Vertical Structures of Late-Type Edge-On Disk Galaxies

Olof A. van den Berg*

Master Thesis

supervisors:
Dr. M. Pohlen†
&
Prof. Dr. R. F. Peletier‡

August 28, 2006

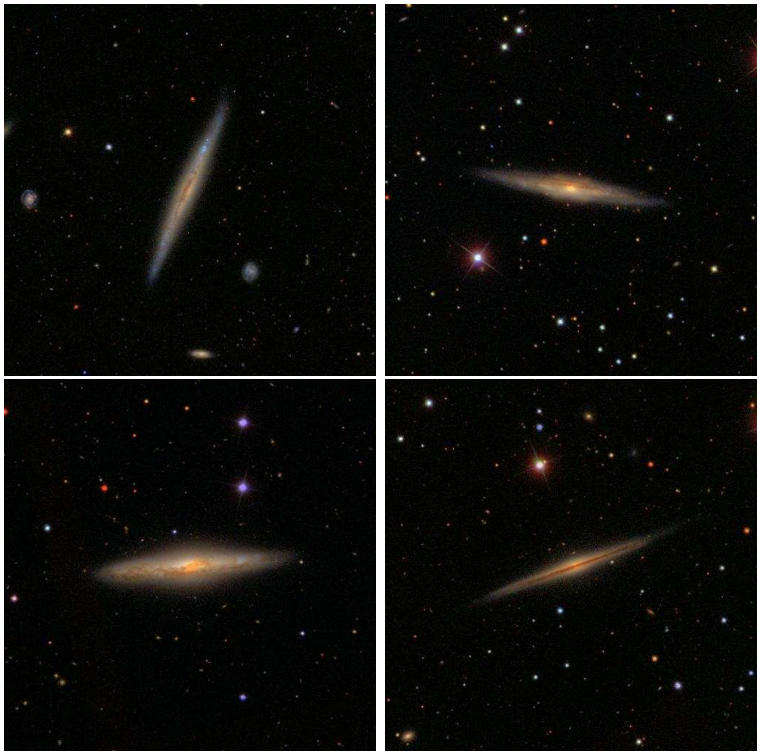

*o.a.van.den.berg@astro.rug.nl
†pohlen@astro.rug.nl
‡peletier@astro.rug.nl

Abstract

The study of the vertical structures of the disks of late-type spiral galaxies is very important as it holds the key to unravelling the formation and evolution of disk galaxies. For example, the uncertainty if all late-type galaxies possess a thick disk, a faint extended disk component containing old stars, plays an important role in this discussion.

To address this question, we collected a pilot sample of 11 late-type disk galaxies, observed in the near-infrared J- and or K'-filter, creating images with high S/N and very flat backgrounds. Various kinds of structure decomposition was done on vertical surface brightness profiles to discover if the galaxies contained thick disks or not and what their parameters would be.

We create vertical colour profile sets for six galaxies available in the J- and K'-band to determine their colour gradients and hence insight in their stellar population.

Our 2D two disk (thin+thick) fits confirm the results of Yoachim & Dalcanton (2006) as we find clear thick disk components in all our sample galaxies except for one case, where the possible existence of a thick disk cannot be excluded. However, our results show clear differences. We only find thick disk components in our high-mass galaxies ($v_{rot} > 120$ km s^{-1}). For two low-mass galaxies added to our sample we confirm a distinct vertical structure but those could not be fitted as a superposition of thin+thick disk. Our thick disk parameter values show also fainter and flatter thick disks than their high-mass galaxies, with an average difference between μ_n and μ_k (the central surface brightness for the thin and thick disk) of 4.5 $\pm$ 0.7 mag arcsec^{-2} and an average scaleheight ratio of 5.6 $\pm$ 1.8. Tests of our fitting methods on artificial galaxies showed that truncated galaxies, a commonly observed phenomenon, will show various deviations from the input parameters, making it difficult to assess the quality of the individual results.

Our $(J-K)$ colour gradients show distinct blueing at larger distance from the plane. This is in contrast to the $(B-I)$ results of De Grijs & Peletier (2000) who find no clear gradient and even a slight reddening at larger scaleheight. Their result is probably affected by star formation near the plane. Our results stay within the Bruzual-Charlot models, showing dust has little influence even close to the galactic plane on our colour profiles. This in contrast to the $(R-K)$ results by Dalcanton & Bernstein (2002) who address their inner reddening to dust influence.

Contents

1 Introduction **5**

1.1 The vertical structure of disk galaxies 5

1.2 The thick disk 5

1.3 Disk colour and colour gradients in edge-on galaxies 6

1.4 Research objectives 7

2 The Data **8**

2.1 Sample & observing runs 8

2.2 NIR imaging background and observations 8

2.3 Data reduction 10

2.3.1 Finalizing the image 12

2.4 Photometric calibration 13

2.4.1 Surface brightness limits 16

3 Disk Models : Structural Parameters **17**

3.1 Models of surface brightness profiles 17

3.2 One dimensional (1D) disk models 18

3.2.1 1D: Single disk model 18

3.2.2 1D: Two disk model 19

3.2.3 1D: Constrained two disk model 19

3.2.4 1D: Alternative fitting functions 20

3.3 Two dimensional (2D) disk models 20

3.3.1 2D: Exponential function fitting 20

3.3.2 2D: Bessel function fitting 21

3.4 Creating surface brightness profiles 22

3.4.1 Averaging 22

3.4.2 Binning 23

3.5 Fitting method 24

3.5.1 Starting values for the Downhill-Simplex method 24

3.6 Weighting 26

3.6.1 Weighting for 1D fitting 26

3.6.2 Weighting for 2D fitting 26

3.7 Tests on artificial galaxies 27

3.7.1 1D: Test fitting 27

3.7.2 2D: Test fitting 27

4 Results **28**

4.1 Sample selection . . . 28
4.2 1D: Constrained two disk fits . . . 29
4.3 1D: Alternative fitting function fits . . . 31
4.4 2D: Two disk (thin + thick) Fits . . . 33
4.4.1 Comments on individual galaxies . . . 34
4.4.2 Intrinsic values of the 2D two disk results . . . 35
4.5 1D: Single disk fits . . . 36
4.6 Fits to artifical galaxies . . . 38
4.6.1 1D: Single disk fits to artificial galaxies . . . 38
4.6.2 1D: Alternative fitting function fits to artifical galaxies . . . 38
4.6.3 2D: Two disk fits on artificial galaxies . . . 42

5 Discussion **43**
5.1 Existence & parameters of thick disks in late-type disk galaxies . . . 43
5.2 1D two disk model versus 2D two disk model . . . 43
5.3 Vertical structures revisited? . . . 44
5.4 Comparison with literature . . . 44

6 Vertical colour profiles & gradients **47**
6.1 Creating colour profiles . . . 47
6.2 Determining colour gradients . . . 48
6.3 Results & discussion . . . 49

7 Conclusions **52**

A Galaxy Atlas **53**

B Single Disk Radial Behaviour of Artificial Galaxies **77**

C Colour Profiles & Gradients **82**

1 Introduction

1.1 The vertical structure of disk galaxies

Late-type disk galaxies could be described as a system with a variety of vertical stellar structure components. They contain a prominent dustlane in the midplane in which stars are currently formed, often around a young disk. Around this young disk lies the thin disk, the main visible structure component of the galaxy, consisting of mainly young metal-rich stars. When one goes to higher vertical heights, the situation becomes more uncertain. A possible other component could emerge: the thick disk, but whether all disk galaxies possess them is still uncertain. The thick disk is considered to consist of older and more metal-poor stars than the stars in the thin disk and has a larger scaleheight and scalelength than the thin disk. Around the disk we expect to find the stellar halo, which is part of the galaxy but not of the disk.

To be able to study vertical structures one has to observe the galaxies edge-on. The surface brightness profile has to be decomposed to find out the structural properties of its components and the distribution and properties of the stars. This is of fundamental importance to gain insight in the formation and evolution of galaxies. A still unanswered, but very important question is if all galaxies have thick disks, since it addresses the viability of different hypotheses for the creation of a thick disk and henceforth also the formation and evolution of disk galaxies. One of these hypotheses considers the thick disk as a separate entity produced in an early phase of enhanced star formation during the initial proto-galactic collapse.

Disk galaxy simulations on cosmological N-body+SPH galaxy formation models by Abadi et al. (2003) find a thick disk that is composed of tidal debris from disrupted satellites, while comparable simulations by Brook et. al. (2004) find that thick disks form during a period of chaotic mergers of gas-rich building blocks.

A family of models propagates the thick disk as an extension (by dynamical heating) of the thin disk, where it is assumed that after the initial collapse all gas settles down into the galactic plane and starts forming stars, experiencing different types of heating mechanisms. Suggestions include heating by spiral density waves, encounters with giant molecular clouds, scattering by massive black holes, energy input by accretion of satellite galaxies, or bar bending instabilities (see for references Pohlen et. al. 2004).

The formation of the thick disk holds the key to unravelling the evolution of disk galaxies. To do so determining the intrinsic components and properties of the vertical structures in disk galaxies is essential and sets strong constraints for galaxy formation and evolution models.

1.2 The thick disk

A disk galaxy is described by a set of distinct stellar entities: a disk population, a bulge component, and a stellar halo. Deep surface photometry of external early-type galaxies (Burstein, 1979; Tsikoudi, 1979) and later elaborate measurements using star counts in our own Galaxy (Gilmore and Reid, 1983) revealed the need for an additional component of stars. This was called a 'thick disk' (Burstein, 1979), since it exhibited a disk-like distribution with larger scaleheight compared to the inner, dominating 'thin disk'. It was originally detected as an excess of light at high galactic latitudes.

The most studied and well known thick disk is that of our own Galaxy. The properties of the Milky Way's thick disk have revealed many differences from the thin disk. Structurally the Milky Way's thick disk has a scaleheight of 0.6–1 kpc, which is about 3 times larger than the thin disk scaleheight. The thick disk also may have a somewhat longer scalelength (3.7 kpc, to 2.8 kpc for the thin disk), a typical thick disk feature stated for external galaxies by De Grijs and Peletier (1997), although Abe et. al. (1999) find a thick disk with a shorter scalelength. For the Milky Way, the observed local (near the Sun) number density of thick disk stars is about 6%–13% of that of the thin disk. Thick disk stars are older ($\approx$10 Gyr) and more metal-poor than stars in the thin

disk, so thick disks are likely to trace the early stages of disk evolution. They have a wide range of metallicity, -2.2 $\leq$ [Fe/H] $\leq$ -0.5, although the metal-weak tail of the distribution contributes only $\sim$1 % of the thick disk and may be a different population than that in the canonical thick disk. Kinematically, Milky Way thick disk stars have both larger velocity dispersions and and slower net rotation than stars in the thick disk.

There is increasing evidence that chemical trends in the thick and thin disk stars are different, showing that the thick is a truly distinct component of the Milky Way. A major diagnostic coming from such different chemical trends between thin and thick disk is the different α-element–to–iron abundance ratios, indicating different formation timescales (see for references Brook et al. 2004).

The measurements required to characterise thick disks are difficult to make outside the Milky Way. The Milky Way thick disk provides less than 10% of the local stellar density, and this faintness makes it hard to do a detailed study of comparable extragalactic thick disks. Studies on thick disk components for external galaxies analyze galaxies in the edge-on orientation, which allows clear delineation between regions where thin and thick disk stars dominate the flux. The edge-on orientation also provides line-of-sight integrations of faint stellar populations to reach detectable levels (see for references Yoachim & Dalcanton 2006).

1.3 Disk colour and colour gradients in edge-on galaxies

A first approach to study the stellar populations which build up galaxies can be done from the colours of galaxies. From that we can gain an understanding of the history of the star formation. For the detailed analysis of the colour profiles of galaxies one needs to adopt a priori assumptions concerning the evolutionary stellar population synthesis, the initial mass function, the metallicity and the star formation history, as well as about the dust geometry and its characteristics. This makes the conversion of broad-band colour gradients to abundance and population gradients in external galaxies controversial and conclusions are not easy to derive.

Because of their sensitivity, colours, which are the difference in magnitudes between two wavelengths, and colour gradients have originally been used to study the metal abundances and ages of stellar populations in the disks of external spiral galaxies. In contrast to the large number of studies of radial colour gradients in moderately inclined and face-on spiral galaxies, the colour behaviour of highly inclined and edge-on galaxies has not received much attention.

In edge-on disk galaxies, the interpretation of intrinsic colours and colour gradients is severely hampered by the presence of dust in the galaxy planes (De Grijs and Peletier, 2000). In general, the dust lanes appear as red peaks in the vertical colour profiles. However, from a comparison with published colours of moderately inclined Sc galaxies, Kuchinski & Terndrup (1996) have shown that for these late-type galaxies there is little or no reddening away from the dust lane. Since statistical studies have shown that the dust content of Sc galaxies is large compared with other disk-dominated galaxy types (e.g. De Grijs et al. 1997), we may assume that the effects of reddening on the intrinsic galaxy colours away from the dust lane are largest for these galaxy types. Thus, colours and colour gradients measured at those distances from the galactic places where the influence of the dust lane is negligible are likely to reflect the intrinsic galaxy properties.

For example, Van der Kruit & Searle (1981b) observed that, at various galactocentric distances, the vertical colours of NGC 891 are getting systematically bluer with greater height above the plane. On the other hand, Jensen & Thuan (1982) did not find any evidence for a similar vertical colour gradient in NGC 4565 in the region where the old thin disc dominates. However, as soon as the light of the thick disk starts to dominate, the disk colours become redder with increasing distance from the galactic plane. A similar result was obtained for NGC 5907, which was interpreted as an extended stellar halo redder than the galactic disc or a very thick-disk component (see for references De Grijs & Peletier 2000).

To summarise, the colour gradients of the colour profiles can be explained by (1) changes in the stellar population, which we are interested in, and (2) variations in reddening due to dust extinction, which we try to avoid (De Jong, 1996).

1.4 Research objectives

Previous detections of thick disk stellar light in external galaxies have been originally made for early-type edge-on galaxies. Without the need for a detailed structure decomposition the thick disk component was clearly visible in several studies. In these, the scaleheight ratio was well determined, but this was not the case for the scalelength ratio. However, only recently Pohlen et. al (2004) conducted the first detailed three dimensional decomposition (taking the line-of-sight into account) of the surface brightness profiles of lenticular galaxies.

Since the work of Tsikoudi and Burstein thick disks are considered to be quite common in lenticular and early-type galaxies, but for late-type galaxies it has not been considered an unambiguous feature because structural decomposition has not been done on a large sample of galaxies to provide sufficient proof.

Thick disks could not be easily seen in late-type galaxies. To do this a detailed structure decomposition was necessary. Van der Kruit & Searle (1981a, 1981b) performed the first three dimensional decomposition of late-type galaxies. Since that time detailed one or two dimensional thick/thin disk decompositions have been reported for only a handful of late-type galaxies.

Recently the inconclusive status of the thick disk in late-type galaxies has been challenged. Dalcanton & Bernstein (2002) and Yoachim & Dalcanton (2006) state that a thick disk is also a common component in late-type disk galaxies. In the first paper thick disk components are inferred from colour maps and colour gradients which show a redding at larger scaleheights, which they attribute to the typical stellar populations in thick disks. For this they focus on low-mass late-type disk galaxies, whereas high-mass disk galaxies do not seem to show such behaviour, which they address to a reddening caused by a larger and more extended dustlane. The reddening in the outer part, or blueing in the inner part, could be addressed to other components or stellar populations.

Continuing on the findings of Dalcanton & Bernstein (2002), Yoachim & Dalcanton (2006) progressed by doing two dimensional one and two disk fits on a subsample of their very late-type disk galaxies. They confirmed the existence of the 'colour' thick disks in all the galaxies of their sample. They also state and show that the thick disk component in low-mass galaxies dominates the profile, contributing nearly half the luminosity of the total galaxy. Although the properties of the components of their high-mass galaxies are comparable to literature, the properties of the components of their low-mass galaxies raise questions and doubts, especially since such they give thin and thick disk central surface brightness differences between –0.8 and 2 mag arcsec^{-2}, and thin/thick disk scaleheight ratios between 1.4 and 2.0 for 11 of their galaxies, which can be seen as unusual considering the commonly addressed properties of the thick disk.

The survey done by Dalcanton & Bernstein (2002) and Yoachim & Dalcanton (2006) is the first extensive search for thick disk components in late-type disk galaxies in many years, so there are few to put their findings to the test. To test if the disk component parameters they find for late-Type disk galaxies can be confirmed we do an extensive research to find and qualify thick disk components in late-type disk galaxies.

To discover a distinct thick disk component in late type disk galaxies we are using the classic way by doing deep surface photometry and structural decomposition of surface brightness profiles. To do this about six edge-on disk galaxies, as a pilot sample, were observed in the J- and/or K'-band, expanded with a second sample of six similar galaxies. We use near-infrared images because those are much less contaminated by the absorbing dust in the mid-plane when doing structure analysis. We test various methods for fitting vertical surface brightness profiles to tackle the problem whether a vertical structure can (or should) be called a thick disk or not.

To compare our $(J-K)$ gradient results we use the results of Dalcanton & Bernstein (2002). This comparison is limited as they use $(R-K)$ profiles and we can only compare to their high-mass galaxy results. We will also compare our results with De Grijs & Peletier (2000), who determined vertical $(B-I)$ colour gradients for a complete sample of edge-on disk galaxies. Besides this, there has not been determined a $(J-K)$ gradient for late-type disk galaxies before with the current observation quality. We use the opportunity to determine the gradients and compare our findings with previous results.

2 The Data

2.1 Sample & observing runs

A first series of observations were carried out by M. Pohlen in February 2004 with the Calar Alto 3.5-m telescope, using OMEGA-Prime, a direct imaging, prime focus, wide-field near infrared camera, giving a field-of-view of 6.8×6.8 arcminutes, with a resolution of 0.396 arcseconds per pixel. A comparison of star position between our and 2MASS images confirmed this resolution within an error of 0.001 arcseconds per pixel. Six late-type edge-on disk galaxies were observed, of which two both in K (2.118 μm) and J-band (1.275 μm), one only in the K'-band and three only in the J-band. We will refer to this set as the CA set.

A second data set of an older observing campain was added to enlarge the sample. This set was observed by R. de Grijs in December 2000 with the 4-m UKIRT telescope, using UFTI, a 1-2.5 μm camera (1024 × 1024 array), with a resolution of 0.091 arcseconds per pixel which was 2×2 binned to a resolution of 0.182 arcseconds per pixel. A comparison of star positions confirmed this resolution as well within an error of 0.001. Six late-type edge-on disk galaxies were taken from this observing run, both in the J and K'-band. We will refer to this set as the UKIRT set.

A third set of reduced optical and R-band images (see Pohlen et. al. (2001,2004) for observation details for observation details), containing two low-mass late-type galaxies and one early-type lenticular galaxy, was kindly provided by M. Pohlen to give a wider range of galaxy types and to allow a better comparison with the literature. For the lenticular galaxy NGC 4179 Pohlen et. al. (2004) already showed it contained a clear thick disk component. We will compare their results for this galaxy with ours, as they used a completely different method.

The galaxy data of the different sets are divided by a horizontal line in Table 1. The data were mostly obtained from the HyperLEDA database[1]. The inclination values were taken from Pohlen (2001). For those galaxies of which no accurate inclination determination could be found, no value is entered. All galaxies have an approximate inclination of 90°.

2.2 NIR imaging background and observations

When one is observing in the near-infrared one is always fighting against the strong and variable sky background, which has significantly more influence than in the optical. It has contributions from OH airglow in the J, H, and K-bands, moonlight (either directly or reflected off clouds) especially in the J-band, and from thermal emission from the telescope and sky in the K-band which varies with temperature and humidity. Although the 10-30% variations in strength with the background caused by these factors do not strongly limit the S/N of observations (except at K for large changes in temperature), they greatly complicate both the creation of mosaics of large regions and accurate surface photometry. Because of the possible rapid shifts in the background time shifts of 60–90 seconds are used. Because saturation of the CCD chip can take place quickly, the exposure times are very short, usually less than 10 seconds.

Like in the optical, data reduction requires accurate correction for the small additive effect of internal lumination, charge generation and charge leakages (dark frames), the large additive effects of sky illumination (sky subtraction frames), and the multiplicative effects of position dependant pixel sensitivity (flatfielding frames). This requires to take various sets of calibration images.

The primary goal of flatfielding images is to correct for pixel-to-pixel sensitivity variations across the area so that relative intensities of objects imaged in different parts of the array are accurately recorded. Flattening the sky background is a secondary effect, although this should also be achieved if the array responds similarly to stellar continuum light and sky emission. Three flatfielding strategies are possible: A set of sky images can be combined to form a sky flat frame, or the same can be done using twilight images. The images of an illuminated screen within the dome can be combined to form a dome flat-fielding frame. The dome flat field could be determined

[1] http://leda.univ-lyon1.fr/

daily taking exposures of the telescope dome with and without illumination from a quartz lamp. The final flatfield frame is the image difference of the two exposures, normalising to its mean.

During the observation one typically shifts the sky frame in a circular pattern around the object frame, with each frame first on the sky, the next on the object and the following frame again on the sky, but now an other part. For the CA set this was done in an OFF-ON pattern (off the source, i.e. on the sky - on the source). For the UKIRT set this was done in an ON-ON-OFF-OFF pattern. The different sets were not fitting to each next set to form a singular sequence. For the data reduction the sequence of images were re-ordered to an OFF-ON pattern so our reduction programs could handle the data similarly as the CA set. To be able to end with a sky frame again the last sky frame was often used again so no object frames were lost unintentionally.

TABLE 1

Observation Sample

Galaxy	RA (2000.0)	DEC (2000.0)	Type	T	d_{25}	i	v_{rot}	$v_{\odot}$	v_{vir}	D
					[′]	[^{o}]	[km s^{-1}]	[km s^{-1}]	[km s^{-1}]	[Mpc]
(1)	(2)	(3)	(4)	(5)	(6)	(7)	(8)	(9)	(10)	(11)
NGC 2424	07h40m39.3s	+39d14m00s	SBb	3.5	3.4	86.5	195.5	3353	3243	45.7
NGC 2591	08h37m25.5s	+78d01m35s	Sc	3.0	3.0	85.5	117.8	1323	1583	22.3
IC 3322A	12h25m42.6s	+07d13m00s	SBc	4.0	2.3	88.5	126.3	995	1055	14.9
NGC 5290	13h45m19.2s	+41d42m45s	Sbc	3.1	3.4	88.5	220.9	2573	2817	39.7
NGC 5348	13h54m11.2s	+05d13m38s	SBbc	3.5	3.5	86.5	67.7	1451	1524	21.4
NGC 5981	15h37m52.7s	+59d23m38s	Sbc	2.8	2.5	86.5	251.1	1764	2813	39.6
NGC 0973	02h34m20.1s	+32d30m20s	Sb	4.0	3.9	89.5	269.2	4855	4948	69.7
UGC 3186	04h51m46.0s	+03d40m05s	Sc	2.0	1.6	–	108.5	4578	4509	63.5
NGC 1886	05h21m48.1s	–23d48m37s	Sbc	3.8	3.2	86.5	154.6	1755	1544	21.7
NGC 2424	07h40m39.3s	+39d14m00s	SBb	3.5	3.4	86.5	195.5	3353	3243	45.7
UGC 4277	08h13m57.2s	+52d38m53s	Sc	4.9	3.3	–	271.4	5459	5650	79.6
IC 2531	09h59m55.5s	–29d37m04s	Sc	7.5	6.6	89.5	222.1	2472	2315	32.6
NGC 4179	12h12m52.1s	+01d17m59s	S0	-1.9	4.3	–	–	1239	1269	17.9
FGC 2339	21h44m39.4s	–06d41m21s	Sc	6.2	1.9	88.5	85.2	3098	3096	43.6
IC 5249	22h47m06.2s	–64d49m56s	SBcd	6.7	4.0	89.0	98.1	2364	2111	29.7

Notes: (1) Galaxy. (2) Right Ascension. (3) Declination. (4) Galaxy Type. (5) Morphological Type Code. (6) Diameter at $\mu_B = 25$ mag arcsec^{-2}. (7) inclination. (8) Rotational velocity. (9) Heliocentric velocity. (10) Systemic velocity with respect to the Virgo Cluster. (11) Distance based on $H_0 = 71$ km s^{-1} Mpc^{-1}.

For the CA set at the beginning or end of each night dome flatfielding and dark images were taken. The observations were typically done in 2-3 sets of 28 image frames. In the CA observations the exposure time in the J-band was 10×6 seconds (which were summed and averaged on the chip) integration time per frame; in the K'-band this was 30×2 seconds per frame, so the sky was monitored every 60 seconds.

For the UKIRT set three sets of 10 frames with a total exposure time of 120 seconds per final image. The observations were typically done in sets of 10–15 image frames. In the first night four standard stars were observed, both in the K and J-band: P9105, P9122, P9138 and P9148 (taken from the catalogue by Persson (1998). In the second night the same stars were used, except for P9148. The stars were observed 1–3 times for 1×15 seconds in J and 1×10 seconds in K' during the night.

TABLE 2

Observation Data

Galaxy	Filter	Date	Run-ID	t_{exp} [min]	Coadds #×[s]	Seeing [″]
IC 3322A	J	04022004	CA	56	56×60	0.9
IC 3322A	K'	04022004	CA	24	24×60	1.3
NGC 2424	J	05022004	CA	29	29×60	0.8
NGC 2591	K'	07022004	CA	53	53×60	0.9
NGC 5290	J	03022004	CA	42	42×60	0.8
NGC 5290	K'	03022004	CA	38	38×60	1.2
NGC 5348	J	07022004	CA	34	34×60	0.9
NGC 5981	J	05022004	CA	61	61×60	0.8
IC 2531	J	19122000	UKIRT	28	14×120	0.9
IC 2531	K'	19122000	UKIRT	30	10×120	0.9
NGC 0973	J	19122000	UKIRT	30	15×120	0.6
NGC 0973	K'	20122000	UKIRT	30	15×120	0.9
NGC 1886	J	19122000	UKIRT	30	15×120	1.0
NGC 1886	K'	19122000	UKIRT	30	15×120	1.0
NGC 2424	J	20122000	UKIRT	20	10×120	1.3
NGC 2424	K'	20122000	UKIRT	30	15×120	1.8
UGC 3186	J	20122000	UKIRT	30	15×120	1.3
UGC 3186	K'	20122000	UKIRT	26	13×120	1.3
UGC 4277	J	19122000	UKIRT	30	15×120	0.7
UGC 4277	K'	20122000	UKIRT	30	15×120	1.3
FGC 2339	R	02082000	ESO	30	3×600	
IC 5249	R	01082000	ESO	30	3×600	
NGC 4179	V	051999	ESO	65	1×600, 1×480, 1×360 1×300, 9×240	1.6

2.3 Data reduction

All image reduction and data analysis was performed in the IRAF[2] environment[3].

From previous runs at Calar Alto there was a necessity to use dark frames, although the dark correction should have been in principle included by doing a sky subtraction with a sky frame. Tests showed that the OMEGA-PRIME camera images did not require dark subtraction as we saw no differences between the resulting images.

Creating flat field frames was the next step. Tests on our data made us decide to use sky flat-fielding frames, because those provide flatter final images compared to dome or twilight images.

To reduce the noise and remove background sources it is preferred to use as many sky frames as possible to form a mastersky for the subtraction of the sky frames from the object image, but this is limited by the rapid changes in the sky structure. However, as tests showed we were limited by this, we had to use the minimal number of sky frames for the object images. So to remove the influence of the stars, SExtractor was used to mask stars on the OFF images, creating an output mask image for each sky frame. Of all objects in the sky image, stars and galaxies, the shape of the flux area is determined by SExtractor and a mask area was created, resulting in an output SExmask image belonging to each object image. Interpolation of the masks with the background value did not give good results as we still saw residuals in the final mosaic-ed image. Because we had many images to be stacked, we decided to keep track of the masks and completely remove

[2]IRAF is the Image Analysis and Reduction Facility made available to the astronomical community by the National Optical Astronomy Observatories, which are operated by AURA, Inc., under contract with the U.S. National Science Foundation.

[3]with custom written packages based on scripts done by Giuseppe Aronica and Michael Pohlen

possible residuals, and thus we did not need to interpolate. The separate SExmask images were used in the final combination to mask the holes produced by stars in the sky image.

Before every object frame was subtracted with the appropriate sky frames (the sky frames that were taken closest to them in time), in this case the minimum number of sky frames (two) near the object frame were used for all reduced galaxies. The sky subtracted target frames were then divided by the sky flat-field (the combination of the two sky images which were normalised). Each of these reduced frames were inspected in case they had large gradient patterns that is not removed by sky subtraction in the combination. Those frames were thus rejected for the final image combining.

The next part consisted of defining relative spatial offsets betweens each object frame in the data (mosaic-ing). This was done by taking three clear and bright stars around the galaxy, ideally forming a triangle, and marking their position in each object frame. After the offsets were determined, all images were combined using a list of the masks for each image that had been made previously with SExtractor so that all the residual influence of the stars in the sky images were removed. Typically a handpicked statistics section (to additively scale the background of each object image to each other) on an already flat part in the to be combined images was selected for the combination – so that the residual background was scaled to an already very flat region.

TABLE 3

Median or Mean Counts in Small Boxes

Galaxy	Filter	Mean of Median [counts]	Mean of Mean [counts]	Median of σ^c [counts]
(1)	(2)	(3)	(4)	(5)
IC 3322A	J	4.32 ± 0.25	4.38 ± 0.25	1.10
IC 3322A	K'	-16.81 ± 0.13	-16.77 ± 0.13	1.89
NGC 2424	J	-0.61 ± 0.23	-0.46 ± 0.23	1.75
NGC 2591	K'	-11.24 ± 0.17	-11.31 ± 0.17	1.27
NGC 5290	J	53.00 ± 0.21	53.27 ± 0.21	1.34
NGC 5290	K'	16.56 ± 0.11	16.68 ± 0.11	1.40
NGC 5348	J	-38.51 ± 0.23	-38.09 ± 0.23	1.76
NGC 5981	J	18.76 ± 0.31	18.73 ± 0.31	1.18
IC 2531	J	-0.84 ± 0.20	-0.83 ± 0.20	1.79
IC 2531	K'	-2.79 ± 0.28	-2.66 ± 0.28	3.17
NGC 0973	J	-0.32 ± 0.16	-0.33 ± 0.16	1.52
NGC 0973	K'	-2.31 ± 0.33	-2.40 ± 0.33	3.28
NGC 1886	J	-0.12 ± 0.32	-0.19 ± 0.32	1.76
NGC 1886	K'	-0.62 ± 0.44	-0.65 ± 0.44	3.74
NGC 2424	J	-0.25 ± 0.46	-0.40 ± 0.46	1.45
NGC 2424	K'	-1.55 ± 0.72	-1.59 ± 0.72	2.45
UGC 3186	J	0.28 ± 0.18	0.26 ± 0.18	1.33
UGC 3186	K'	-0.38 ± 0.29	-0.43 ± 0.29	2.65
UGC 4277	J	-0.68 ± 0.16	-0.68 ± 0.16	1.50
UGC 4277	K'	-0.43 ± 0.46	-0.51 ± 0.46	2.74
FGC 2339	R	3888.66 ± 5.46	3887.30 ± 5.46	24.23
IC 5249	R	4564.68 ± 14.45	4569.42 ± 14.45	26.56
NGC 4179	V	563.6 ± 1.72	564.2 ± 1.72	4.15

Notes: (1) Galaxy. (2) Filter. (3) Mean pixel value of the median values of the small boxes made on the sky background and the standard deviation to this mean. (4) Mean pixel value of the mean values of the small boxes made on the sky background and the standard deviation to this mean. (5) Median of the standard deviation in the small boxes made on the sky background.

Ideally the final background of the image is zero. However, this is rarely the case. Thus the value

of the background has to be subtracted from the image. The background however, is not always perfectly smooth and flat. There are residual large scale gradients and of course forground stars and background galaxies. To find the remaining background value sections around the galaxy were made in the shape of small boxes, 20×20 pixels in size. They were placed manually around the galaxy to map the background as good as possible avoiding the influence of starlight. The mean of the median value of all those boxes provided our background pixel value. The results are listed in Table 3, together with the standard deviations of those means and for comparison the mean value of the boxes when taking the mean value. After the substraction of this value the image was ready.

2.3.1 Finalizing the image

After subtracting the sky background, we applied SExtractor again to automatically find and mask the background stars according to their intensity, size and shape. The masked positions and areas were put into a list. The objects missed by SExtractor, especially around and on top of the galaxy were manually masked and added to the list. Figure 1 shows a rotated and centralized negative image of the galaxy IC 3322A J after masking.

Rotating and centralizing the galaxy is necessary to be able to create a set of vertical surface brightness profiles, which we use for fitting instead of a full two dimensional pixel distribution. We rotated the images according to the smallest rotation angle so that the galaxy is positioned horizontally in the plane. The disk was symmetrically divided, and using one of the multi-colour views in IRAF and blinking the halves of the images, the galaxy was centralized by eye, allowing for subpixel shifts.

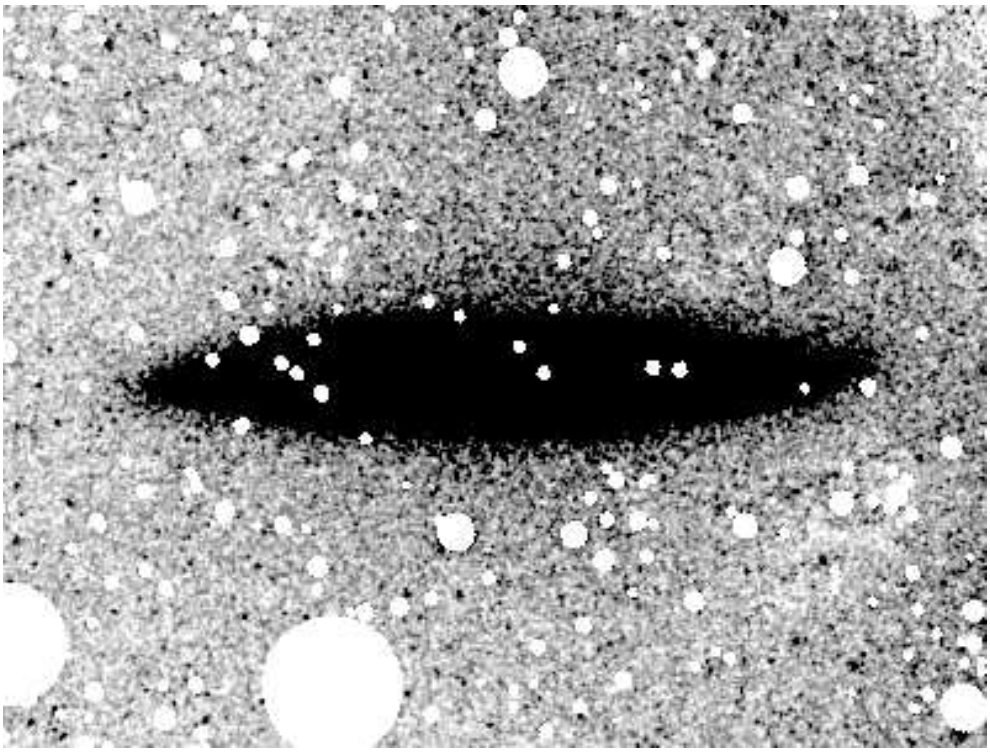

Figure 1: Final masked image of IC 3322A J.

2.4 Photometric calibration

Photometric calibration is necessary to transfer the observed flux to a standard system of the observed galaxies. Usually the zeropoint is determined with the formula

$$m_{fit} \;=\; m_{obs} \;+ a \cdot X \;+\; b \cdot (J-K) \;+\; \text{zeropoint}\;, \tag{1}$$

where a$\cdot X$ is the extinction term with X the airmass and $b \cdot (J-K)$ the colour term. Normally standard stars are observed to obtain the zeropoint, but because no standard stars had been observed in the CA run we had to put everything into one zeropoint.

The photometric calibration was done by doing aperture photometry of all known stars on the frame of the galaxy in the 2MASS catalogue[4] of point sources. For matching the fields we used the Aladin Sky Atlas[5]. We applied three different methods to determine the zeropoints. The 2MASS catalogue provides a list of stars and their magnitudes in the JHK bands which can be selected for the region around our galaxies on the 2MASS images. The 2MASS images are already provided with a zeropoint, which in addition allows us to use their stars to determine the zeropoint of our images independently. The provided stars were matched with stars from our own image and the magnitude read. For the selected stars aperture photometry was done to determine the flux of the stars in our own images. Galaxies (still in the point source catalogue), saturated and crowded regions, or stars too close to the galaxy or the edge of the frame, were not taken into account. By comparing the 2MASS magnitudes and the fluxes the mean zeropoint for each image was calculated. Another test was done by doing also aperture photometry on the stars in the 2MASS image and determining the stellar magnitude manually.

TABLE 4
PHOTOMETRY CA SET

Galaxy	Filter	Zeropoint$^a_{CM}$ [mag]	Zeropoint$^b_{MM}$ [mag]	Zeropoint^c_B [mag]	Night
(1)	(2)	(3)	(4)	(5)	(6)
IC 3322A	J	25.21 ± 0.09	25.18 ± 0.07	25.33	2
IC 3322A	K'	23.56 ± 0.05	23.57 ± 0.08	23.60	2
NGC 2424	J	25.39 ± 0.08	25.39 ± 0.14	25.48	3
NGC 2591	K'	23.43 ± 0.12	23.50 ± 0.19	23.48	5
NGC 5290	J	25.09 ± 0.06	25.09 ± 0.11	25.20	1
NGC 5290	K'	23.49 ± 0.09	23.50 ± 0.11	23.49	1
NGC 5348	J	24.99 ± 0.06	25.29 ± 0.10	25.23	5
NGC 5981	J	25.24 ± 0.13	25.31 ± 0.08	25.43	3

Notes: (1) Galaxy. (2) Filter. (3) Zeropoint by aperture photometry on Standard Stars. (4) Zeropoint by aperture photometry on 2MASS stars with *C*atalogue *M*agnitudes. (4) Zeropoint by aperture photometry on 2MASS stars with *M*agnitudes measured *M*anually the 2MASS images. (5) Zeropoint by aperture photometry on the galaxy bulges in both images. (6) Observation night.

As we were uncertain of the apertures 2MASS used, aperture photometry was done on the bulge for comparison. Four circular apertures were made around the center of the galaxy with the largest circle including the whole bulge. Within each circle the flux was calculated and compared to similar circles on the galaxy in the 2MASS image, resulting in a value for the zeropoint. Making larger circles included too much background that influenced the zeropoint value. The aperture photometry on the bulge was done because this had also been done in the 2MASS catalogue, but comparison with those values were not directly possible because they used ellipse shaped areas for their photometry and the exact shape of the ellipse was not given. Thus we used the bulge

[4] http://www.ipac.caltech.edu/2mass/
[5] http://aladin.u-strasbg.fr/java/nph-aladin.pl?frame=launching&-rm=14.1&-server=Aladin

photometry to have another indication of the zeropoint value when comparing them to the other methods. The results of the different methods are shown in Table 4.

The zeropoint values we found with the 2MASS magnitudes were similar zeropoints we derived by manually determining the magnitudes. However, the stellar magnitudes from 2MASS are determined in a way we could not fully recover (see Skrutskie et al. 2006), while the 2MASS images available on their webserver have been changed in pixel resolution. This makes our manual determination of the magnitudes more uncertain and inaccurate and creating in most cases larger standard deviations, even when we removed all stars that had a magnitude error larger than 0.15.

The UKIRT set did have standard stars observed (taken from Persson et al. 1998). We had too few standard stars to disentangle an extinction and colour term for the zeropoints. The zeropoints showed no dependency airmass of the standard star, so we decided to combine all factors into the zeropoint. We took the average of each set of images. For each night the mean zeropoint for the J- and K'-band were calculated to provide a zeropoint for all respective galaxies (see Table 5).

TABLE 5
Standard Star Photometry UKIRT Set

Star	Filter	Airmass	Zeropoint[a]	Night
P9105	J	1.11	26.08 ± 0.01	1
P9105	J	1.03	26.06 ± 0.01	1
P9122	J	1.20	26.02 ± 0.02	1
P9138	J	1.12	26.06 ± 0.01	1
P9148	J	1.05	26.09 ± 0.02	1
mean	J		26.06 ± 0.03	1
P9105	K'	1.10	25.58 ± 0.02	1
P9105	K'	1.03	25.55 ± 0.01	1
P9122	K'	1.20	25.52 ± 0.01	1
P9138	K'	1.11	25.53 ± 0.02	1
P9148	K'	1.05	25.59 ± 0.02	1
mean	K'		25.55 ± 0.03	1
P9105	J	1.29	26.14 ± 0.02	2
P9105	J	1.27	26.11 ± 0.02	2
P9105	J	1.06	26.08 ± 0.02	2
P9122	J	1.36	26.02 ± 0.03	2
P9122	J	1.18	26.04 ± 0.02	2
P9138	J	1.20	26.07 ± 0.02	2
mean	J		26.08 ± 0.04	2
P9105	K'	1.26	25.64 ± 0.07	2
P9105	K'	1.06	25.61 ± 0.06	2
P9122	K'	1.35	25.57 ± 0.05	2
P9122	K'	1.18	25.58 ± 0.05	2
P9138	K'	1.21	25.60 ± 0.06	2
mean	K'		25.60 ± 0.03	2

Notes: [a] Zeropoints in magnitudes.

To test the reliability of the photometric calibration of the CA set via 2MASS in comparison with the standard stars, we compared the 2MASS calibration also for the UKIRT set (see Table 6). As the image frames of the UKIRT set are small and don't encompass the whole galaxy, a comparison with the 2MASS catalogue was done only where possible. Larger deviations are probably caused by a lack of sufficient stars we could use. Aperture photometry was done on the bulge, resulting in comparable values with the standard star zeropoints, except for UGC 3186, which is probably caused by it being very faint and small.

To obtain more external comparisons for our photometry, we searched in the literature. Unfortunately we did not find any aperture photometry in the bands we used for any of our galaxies and only found one contour map. Comparing contours provides only a crude comparison but is useful to see if the zeropoints deviate by less than 0.2 magnitude. The used contour map was for IC 2531 by Kuchinski et al. (1996). As an other internal comparison we compared the contour maps of NGC 2424, a galaxy that is observed in both sets in the same band. For both maps the comparison shows that the error is smaller than 0.2, showing that our zeropoints are sufficiently accurate.

TABLE 6

PHOTOMETRY UKIRT SET

Galaxy	Filter	Zeropoint$_{SS}$ [mag]	Zeropoint$_{CM}$ [mag]	Zeropoint$_{MM}$ [mag]	Zeropoint$_{B}$ [mag]	Night
(1)	(2)	(3)	(4)	(5)	(6)	(7)
IC 2531	J	26.06 ± 0.03	25.97 ± 0.09	26.15 ± 0.15	26.04	1
IC 2531	K'	25.55 ± 0.03	25.49 ± 0.26	25.54 ± 0.24	25.54	1
NGC 0973	J	26.06 ± 0.03	26.07 ± 0.13	26.24 ± 0.07	26.08	1
NGC 0973	K'	25.60 ± 0.03	25.53 ± 0.06	25.80 ± 0.24	25.59	2
NGC 1886	J	26.06 ± 0.03			26.08	1
NGC 1886	K'	25.55 ± 0.03			25.61	1
NGC 2424	J	26.08 ± 0.04			26.13	2
NGC 2424	K'	25.60 ± 0.03			25.62	2
UGC 3186	J	26.08 ± 0.04			27.84	2
UGC 3186	K'	25.60 ± 0.03			25.36	2
UGC 4277	J	26.06 ± 0.03	26.01 ± 0.15	26.13 ± 0.05	26.06	1
UGC 4277	K'	25.60 ± 0.03	25.38 ± 0.18	25.96 ± 0.40	25.51	2

Notes: (1) Galaxy. (2) Filter. (3) Zeropoint by aperture photometry on Standard Stars. (4) Zeropoint by aperture photometry on 2MASS stars with *C*atalogue *M*agnitudes. (5) Zeropoint by aperture photometry on 2MASS stars with *M*agnitudes measuered *M*anually on the 2MASS images. (6) Zeropoint by aperture photometry on the galaxy bulges in both images. (7) Observation night.

2.4.1 Surface brightness limits

Table 7 shows the magnitude levels corresponding to their 1, 2 and 3 from the standard deviation above the residual background noise. These are the surface brightness values we use as maximum limits of how deep we can reach into the galaxy. The last column contains the $\mu_{\rm crit}$ values, which is the critical surface brigthnbrightnesswhere we really trust the profile, i.e. where beyond the $\pm 1\sigma$ profiles deviate by more than 0.2 mag (see figure 2 in Pohlen & Trujillo 2006) for the profile obtained using our mean residual background values of Table 3. See Appendix A for examples.

TABLE 7

Residual Background Estimations

Galaxy	Filter	Zeropoint [mag]	1 σ [mag/$\Box''$]	2 σ [mag/$\Box''$]	3 σ [mag/$\Box''$]	$\mu_{\rm crit}$ [mag/$\Box''$]
(1)	(2)	(3)	(4)	(5)	(6)	(7)
IC 3322A	J	25.21	**24.70**	23.95	23.51	22.38
IC 3322A	K'	23.56	**23.76**	23.01	22.57	21.47
NGC 2424	J	25.39	24.97	**24.22**	23.78	22.81
NGC 2591	K'	23.42	**23.33**	22.58	22.14	21.04
NGC 5290	J	25.09	24.77	24.02	**23.58**	22.48
NGC 5290	K'	23.49	23.87	**23.12**	22.68	21.71
NGC 5348	J	24.99	24.57	23.82	23.38	22.39
NGC 5981	J	25.24	**24.50**	23.75	23.31	22.34
IC 2531	J	26.06	24.11	23.36	22.91	21.96
IC 2531	K'	25.55	23.23	22.48	22.04	20.99
NGC 0973	J	26.06	24.35	23.60	23.16	21.98
NGC 0973	K'	25.60	23.10	22.35	21.91	20.94
NGC 1886	J	26.06	**23.60**	22.84	22.40	21.34
NGC 1886	K'	25.55	**22.74**	21.50	21.06	20.52
NGC 2424	J	26.08	23.22	22.47	22.03	21.01
NGC 2424	K'	25.60	22.26	21.50	21.06	19.99
UGC 3186	J	26.08	24.24	23.49	23.05	21.83
UGC 3186	K'	25.60	23.24	22.49	22.05	21.08
UGC 4277	J	26.06	**24.35**	23.60	23.16	22.16
UGC 4277	K'	25.60	**22.74**	21.99	21.55	20.56
FGC 2339	R	25.76	28.02	**27.27**	26.83	25.55
IC 5249	R	25.76	28.17	27.42	**26.98**	25.85
NGC 4179	V	24.14	27.71	**26.96**	26.52	25.96

Notes: (1) Galaxy. (2) Filter. (3). Zeropoint. (4–6) Surface brightness level of the variation of the residual background for 1,2, and 3 σ. (7) Critical surface brightness.

3 Disk Models : Structural Parameters

3.1 Models of surface brightness profiles

No physical law exists which describes the surface brightness profile of a galaxy. Initially Patterson (1940) and later De Vaucouleurs (1959) showed that surface brightness profiles could be described by an exponential function. Even later Freeman (1970) surveyed the literature to show empirically this exponential behaviour on face-on disk galaxies and coupled the exponential function with a dynamical background, establishing its form as we know it up to today as

$$I(r) \;=\; I_0 e^{-r/h} \;, \tag{2}$$

where r is the radial position from the center of the disk and h the radial scalelength, and I_0 the central surface brightness.

Van der Kruit (1979) showed that the surface brightness in z is independent of r and that the vertical profile can be described by an analogue exponential function using the vertical scaleheight as a parameter. In an attempt to fit the z distribution of light at each r by that of a locally isothermal sheet, Van der Kruit & Searle (1981) found that a $\mathrm{sech}^2\ (z/z_0)$ function was a more appropriate description for the vertical surface brightness profile. Some years later Van der Kruit (1988) proposed to use a sech function as an intermediate solution to fit vertical profile as he showed that the exponential and the sech^2 function all belonged to the same family of density laws

$$I(z) \;=\; 2^{2/n} I_0\ \mathrm{sech}^{2/n}(nz/2z_0)\ ,\ (n\ >\ 0) \tag{3}$$

where $I(z)$ is the observed vertical density profile and z_0 the scaleheight, while z is the distance from the plane. The isothermal model is the extreme for $n = 1$ and the exponential is the other extreme for $n \;=\; \infty$. With this family of density laws, there are several ways to determine structural parameters.

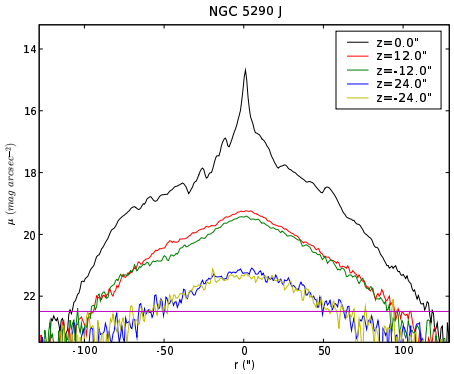

Figure 2: Radial profiles of NGC 5290 J at the midplane and at vertical positions above and below the plane. The magenta line shows μ_{crit}.

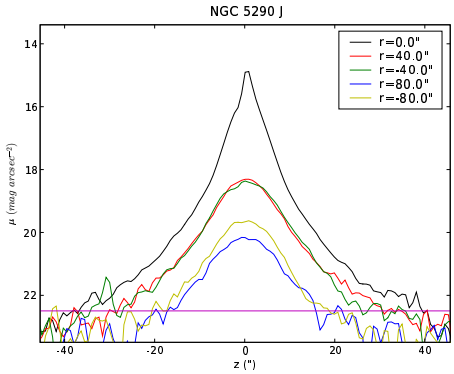

Figure 3: Vertical profiles of NGC 5290 J at the center and at two radial positions on the left and right side from the center. The magenta line shows μ_{crit}.

3.2 One dimensional (1D) disk models

3.2.1 1D: Single disk model

A large family of fitting functions (see equation 3) is available to describe the behaviour of the vertical structure of an edge-on galaxy. As fitting for n adds in an extra and complex parameter to the fit, we have to choose a function to use for our fits. The exponential and the sech^2 function are the two extremes within which those fitting functions behave. In the past both functions have been used to fit vertical surface brightness profiles and no clear preference has been decided on. This is because the main difference between sech^2 and exponential is only the inner part close to the plane. In the outer part both functions have the same shape. The sech^2 is thus mainly used to describe the inner part of the profile in case it shows intrinsic flattening (see figure 3 for an example), while the exponential function expects a peak.

Abe et al. (1999) state that there is no need to use for a sech^2 function to fit the vertical surface brightness profile they observed for IC 5249. The flattening in this case is not intrinsic to the galaxy but caused by external effects: seeing, the dustlane and a not exact inclination of 90°.

Seeing is a common known flattening effect immediately caused by the observations. To determine up to where this flattening still influences the profile a preliminary fit in the z-direction was first made in a cut on a radial position that showed a clear flattened behaviour in the inner part so that a first approximation of where the flattening takes place could be made. The inner points were then removed and a fit was made to obtain the best starting values for the fit. The fitted curve was then convolved with a Gaussian filter to simulate the atmosphere's effect (matched to two times the FWHM), and plotted over the data set including the inner data points and the fitted curve. The point where the Gaussian filtered fitted curve broke away from the fitted curve could be taken as the boundary point where the seeing had too much influence over the dataset.

The flattening of the surface brightness profile is also caused by the remaining dustlane, which, especially in the J-band, absorbs part of the light. We could not distinguish its effect on the flattening from the effect of the seeing. Because we average over four quadrants for our two dimensional fits (see Section 3.4) we lose the advantage of taking the side with the least dustlane influence for the fit, especially when the galaxy is not perfectly edge-on, which is the case for most of our galaxies. The vertical size of the dustlane was determined by comparing the subtracted profiles of the original image with the average image.

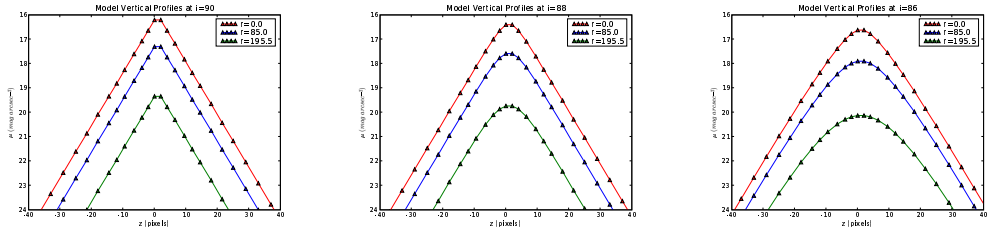

Figure 4: Vertical profiles of observed artificial 3D galaxies at different inclinations. Each panel shows profiles at three different radii of a galaxy at $i = 90°$ (left panel), $i = 88°$ (middle panel), $i = 86°$ (right panel).

A third flattening effect happens when the galaxy is not exactly at an inclination of 90°. Figure 2 shows this effect for three different inclinations in a simple 3D exponential galaxy model with line-of-sight integration over the radius to create the 2D image. The same binning algorithm for our sample galaxies is also applied to show small effects, including a flattening of the inner region

because of the binning. At $i = 90°$ the profiles show a straight peak in the center, but the effects of the inclination grow rapidly at $i = 88°$ and even worse at $i = 86°$, especially at larger radii, making it even harder to determine if a flattening is intrinsic or not.

To confirm that with our data we cannot tell where these effects disappear we would have to determine for each its boundary. As detailed deconvolution of the seeing is beyond the scope of this research and the inner flattened part we observed of no importance to our fitting we decided to use the exponential function and to remove all flattened inner points. We tested several of our sample galaxies on the effects of seeing and the dustlane and found them to be hard to distinguish from each other but always causing sufficient flattening that it was not possible to distinguish the observed from the intrinsic flattening.

After deciding on the exponential function, without an extra vertical structure component, only two parameters are needed to fit the vertical profile of a sample disk: the central intensity I_0 and the scaleheight z_0,

$$I(z) = I_0 e^{-z/z_0} . \tag{4}$$

Since we fit the profile in magnitude arcsec^{-2} even a simple linear fit would sustain when using an exponential function for the fit. The used function for this linear fit is

$$\mu(z) = \mu_0 + 1.086 z/z_0, \tag{5}$$

where the factor 1.086 corrects for the exponential when the intensity is changed into a logarithmic surface brightness. This is the simplest way to fit the vertical distribution and we always apply it for comparison (see Appendix A).

3.2.2 1D: Two disk model

As the thick disk is considered a separate vertical component from the thick disk, the vertical exponential function is expanded and broken into two similar functions to describe the thin and the thick disk separately, doubling the amount of fitting parameters to four, and creating the new fitting function

$$I(z) = I_n e^{-z/z_n} + I_k e^{-z/z_k} , \tag{6}$$

where I_0 and z_0 have now been split into a thin disk central intensity I_n and scaleheight z_n and a thick disk central intensity I_k and scaleheight z_k.

3.2.3 1D: Constrained two disk model

While fitting the two disk model, we realised that intrinsically the two functions describing the thin and the thick disk are the same, so both parts must be constrained heavily. When fitting they have to be given different starting values and fitting boundaries to prevent the fitting function from giving unphysical solutions and to be able to distinguish the results for the thin and the thick disk.

For the two disk model we expect to see two vertical regions, the inner part dominated by the thin disk and an outer part dominated the thick disk. This is surely the case for the thin disk as it is by definition the dominating disk, as the thick disk is expected to be fainter and more extended.

For fitting one will give preference to the smallest possible amount of fitting parameters. Of all the parameters of the two disk fit, the scaleheight of the thin disk is always the most accurate and stable parameter because of its high S/N ratio, while the thick disk component will be faint with few datapoints and a lower S/N.

A 1D Two Disk fit is often ill constrained as it uses four parameters to describe 15 datapoints, so the results can be erratic if there are irregularities in the inner part of the profile. One solution is to constrain the well defined thin disk, by constraining the value of z_n by taking a small selection of datapoints which clearly belong to the thin disk and from these determine the slope for each

cut. A mean or median of all profiles over the radius can then be used to determine a constant value for z_n. Using this value as a constant for each cut of the 1D two disk fit shrinks the amount of fitting parameters from four to three, making it easier and faster to fit the profile.

3.2.4 1D: Alternative fitting functions

As we are looking for an extended vertical structure next to the thin disk we expect not to be able to fit our profiles well with a two parameter fitting function as it will need to choose an intermediate solution that will not describe the shape of the profile sufficiently. The four parameter fitting function of the two disk (thin+thick) fit is not very stable and depends highly on the quality of the profile. A single fitting function that forms an intermediate solution between the one and two disk fit is the Sérsic Law, which is defined as

$$I(z) \;=\; I_0 \exp\left[-\kappa(n)\left[-(r/r_c)^{1/n} - 1\right]\right], \tag{7}$$

where n is the power law index with κ depending on n and r_c is the halflight radius. There is no exact definition of $\kappa(n)$, so we use here the one determined by Balcells et al. (2001), which defines $\kappa(n)$ as

$$\kappa(n) = \; 1.9992n \;-\; 0.3271\;. \tag{8}$$

There also exists a simplified version of the Sérsic Law which is called the Generalized Gaussian, which is defined as

$$I(z) \;=\; I_0 \exp\left[-(|r|/r_0)^{\lambda}\right], \tag{9}$$

where λ is called the the shape parameter and r_0 the width of the distribution. The r_c and r_0 in both functions are not the same and need to be converted for comparison. The keypoint is that both functions have 3 parameters, whereas the two and one disk fits have 4 and 2 respectively.

3.3 Two dimensional (2D) disk models

Fitting a vertical structure with the 1D Two Disk model results in many parameter value results for which it is hard to tell if an individual profile is good enough to determine the average values for the disk components. To avoid this issue one can add additional constraints to the model by adding another dimension to the fitting, in this case the radial distribution, which we know is well described by an exponential, to constrain the fitting better.

3.3.1 2D: Exponential function fitting

The radial structure of a face-on galaxy can be described best by a broken exponential consisting of three distinct parts: the bulge, the inner disk and the outer disk. The bulge part is steep, the inner disk part much flatter, while the outer disk is often steep again. This latter kind of shape is called truncation (see figure 2 for an example). Each part has a different radial behaviour and one thus wants to avoid the bulge, as it is an additional component and may have a different vertical structure, and the outer disk, which has a different radial scalelength than the inner disk. The break points of the inner disk with the bulge and the outer disk were determined by eye, making sure points lying close to the break points were excluded. The inner disk, which we use to the fit, is described in the face-on case by the exponential function proposed by Freeman (1970) (see equation 2).

Adding this exponential radial fitting function to the 1D vertical fitting function creates a two dimensional fitting function which can be used as an extra constraint on possible varying radial behaviour of the inner surface brightness of the thin and the thick disk by combining all the cuts to obtain one set of fit values, i.e. there should be only one scaleheight for the thin and the thick

disk at all radii.

As the thin and thick disk are assumed to have a constant z_n and z_k, their local I_n and I_k values are coupled by the radial distribution as a galaxy becomes fainter in its outer parts. As the scaleheights of the thin and thick disk are separate parameters, it is possible that the scalelengths of the thin and thick disk are different from each other. This requires the vertical functions of the two components to have a separate radial addition. We describe the scaleheight for the thick disk as a ratio factor $f_z = z_k/z_n$, to describe the difference between both scaleheights, leaving the thin disk scaleheight as the main scaleheight parameter. We did the same was for the scalelength, using the ratio $f_h = f_k/f_n$ instead of h_k, leaving the thin disk scalelength as the main scalelength parameter. Using these factors makes it easier to assess our results. The new 2D fitting function becomes

$$I(r,z) = I_n e^{-r/h_n} e^{-z/z_n} + I_k e^{-r/f_h h_n} e^{-z/f_z z_n} , \tag{10}$$

where the thin disk scalelength h_n and f_h are two extra free parameter to the four existing free parameters, while the fit is done over r and z.

3.3.2 2D: Bessel function fitting

As a galaxy is not two dimensional but three dimensional a conversion between the face-on and edge-on galaxies is required to be able to use a similar description of the radial behaviour of the surface brightness. Van der Kruit (1979) showed that to keep the value of the scalelength that is determined for a face-on galaxy, which is derived from fitting an exponential function to the surface brightness, for an edge-on galaxy a modified Bessel function of the first order is required for the conversion, changing the fitting function to

$$I(r) = I_n(r/h_n)K_1(r/h_n) . \tag{11}$$

The results from the line-of-sight integration assume a infinite disk without truncation. Truncation however, is a common feature of galaxies (see Kregel et. al. 2002 and Pohlen & Trujillo 2006) which makes the resulting scalelength from the Bessel function not exactly comparable to the face-on scalelength. The exponential radial function is just a simplified case which in practice works just as well. The new two dimensional two disk function, assuming no truncation, becomes

$$I(r,z) = I_n(r/h_n)K_1(r/h_n)e^{-z/z_n} + I_k(r/f_h h_n)K_1(r/f_h h_n)e^{-z/f_z z_n} . \tag{12}$$

Computation times of either the exponential or the Bessel function proved to be similar, leaving us the freedom to choose either as the preferred fit function on that account.

3.4 Creating surface brightness profiles

The surface brightness profiles of the galaxies were made by binning the image data with a minimum size of 3 pixels, equivalent to the seeing, exponentially growing from the center in the radial and vertical direction. We do this to smooth peaks and irregularities in the profile, but also so that in the outer parts, where the influence of the noise grows larger, more area contributes to the mean intensity. This is to retain an approximately constant overall and higher S/N ratio, thus making it able to follow the profiles further out (De Grijs and Peletier, 1997). If a bin possessed a partial mask, the mask values were ignored and only the real data was used to calculate the average intensity. The vertical position of the bin was determined by weighting all used datapoints to their position. See figures 2 and 3 for examples of radial and vertical profiles.

3.4.1 Averaging

As a galaxy is never exactly symmetrical there are two methods to obtain a result. In the first method one uses the original image and fits profiles to each quadrant of the galaxy, taking the average of all good profiles. In the second method one averages the galaxy over its four quadrants and only fits the vertical profiles of one quadrant, obtaining the average immediately. For our 1D Disk fit we use the original image fitting the profiles of all four quadrants as it allows us to use the full depth and we can weight the datapoints of each cut appropriately, while using a $z_{\max}$ as an outer boundary for the vertical height where we think the noise is starting to dominate.

Instead of using the original image like we did for the 1D model and calculating the average afterwards we decided to use a quadrasized average galaxy to obtain an average result immediately as a quadrasized average has several advantages:

1. Intrinsic asymmetric variations in the light distribution are minimized, creating a natural mean image for each galaxy.

2. The S/N ratio is increased as the noise levels are diminished and the intensity of the galaxy becomes more coherent.

3. The flattening of possible asymmetric large scale structures in the background that still remained after the data reduction and the subtraction of the sky image and residual background. As the subtraction of the residual background was done by determining a single mean number of the pixel values around the galaxy there could still be brighter residual structures near the galaxy. This can cause extended vertical structures in the surface brightness profiles which could be mistaken as a hint of a thick disk. Averaging reduces this possible influence.

4. Minimizing the influences of remaining small and faint unmasked stars closely around the galaxy causing individual points in the outer part of the profile to show unwanted excess light. Applying generous mask sizes would mask most of the outer parts of the profile, thus making it impossible to see any hint of a vertical structure.

Following Van der Kruit & Searle (1981) and Pohlen et. al (2000), we divided the galaxies into their quadrants and averaged the four images. As the masked regions still possess a pixel value that would influence the average, the masked regions were not taken into account. This also removed the chance of having a masked region in our selected profiles. Although using a quadrazised average makes us lose the possibility to study the intrinsic asymmetries of the disk this is not of importance to our research.

To remove the datapoints that clearly belonged to the noise we selected a surface brightness value at which the fainter datapoints would be removed. This cut level was determined by removing all points below the magnitude of the 1, 2 or 3 σ level of the residual background intensity. This

cut level depended on the overall quality of each image. Because we wanted to see the faintest parts of the galaxy we went as deep as possible. The corresponding cut level magnitudes, which I will henceforth refer to as $\mu_{\rm cut}$, have been set to boldface in Table 7 (see columns 4–6).

3.4.2 Binning

Binning, which is the grouping of datapoints and taking the average value of them, is incredibly important when fitting surface brightness profiles.

To attest the highest quality to a fit one would like to use as much of the observed surface brightness profile as possible. For one dimensional fits we used the original galaxy image, which includes many variations and irregularities for each vertical profile. The quadrasized average smoothens the surface to some extent and also increases the S/N ratio, but not sufficiently.

Binning itself smoothens the surface brightness to some extent, depending on its size, but it does not take into account that at lower surface brightness areas, at higher vertical and larger radial positions, the S/N ratio will go down and more area has to be taken into the bin for sufficient smoothing.

To solve this issue one makes the binsizes grow vertically and radially to improve the profile even more, as one desires to follow the vertical structure as far out as possible and to keep the S/N ratio almost constant for all points in the inner and outer part, because that will improve the quality of the fit. The minimum bin is equivalent to the FWHM, 3 pixels. The growing goes according to the function

$$\mathrm{bin}_i \cdot f_b^i \ . \tag{13}$$

The growing factor f_b is very important. This factor can make the bins smaller and larger per radius and z depending on its value. The factor cannot be too small, or it would not smoothen the irregularities sufficiently, and it cannot be too large, as it would smoothen and flatten the profile too much as it takes too much area into the average. A too large f_b also decreases the number of cuts that can be used for the fit as the bins grow larger but the selected radial fit region keeps the same size. The effects of changing the f_b value on the amount of datapoints varies. As datapoints are lost due to less cuts, it is able to obtain more datapoints vertically because the bin takes more datapoints into its average. Tests on the shape of the profiles showed a f_b of 1.07 to be, in our case, a minimum for smoothening sufficiently to obtain a successfull fit. From this number only small increases in the trend of 0.01 already improves the profiles considerably, but also quickly takes effect on the amount of cuts.

As an example, figure 5 shows the central positions of all the bins in the vertical and radial direction, with f_b is 1.09, on the upper north-east quadrant of the image of NGC 5290 J.

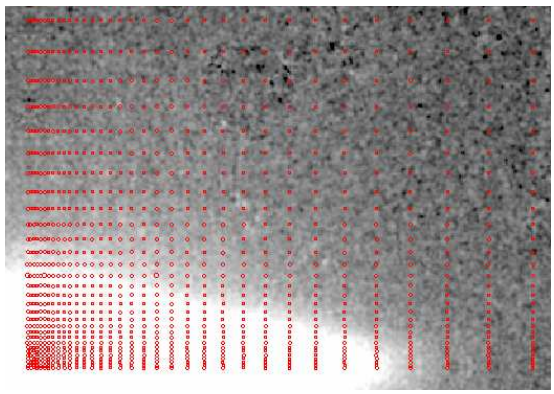

Figure 5: Example of a grid on NGC 5290 J, showing the central positions of the bins which grow in size with a factor of 1.09 in the vertical and the radial direction in one quadrant.

3.5 Fitting method

For the two disk (thin+thick) model fitting with four parameters, in the 1D case, is complicated; fitting with six parameters as in the 2D case, is even more complex. The main problem is that a fitting model with so many free parameters can obtain many possible solutions to give a good fit. Determining which fit result is the best can not be put to guessing, especially when one searches for the lowest χ^2 value, following the formula

$$\chi^2 \;=\; \sum (\text{data} - \text{model})^2 \;. \tag{14}$$

The typical methods use the Levenberg-Marquardt least-squares algorithm for fitting. Just for the one dimensional model, with only four parameters, the fitting results with this algorithm are already highly inconclusive, giving many possibilities. The χ^2 value differences are minimal. Varying along a large range of solutions only provides long computation times and leads to an other solution than the input values. The least-squares algorithm only looks for low χ^2 values in the neineighbourhoodhereas one wants to look around a range of boundaries for the region that shows the steepest slope to a solid χ^2 solution.

A method that meets these requirement better is the Downhill Simplex method (Nelder and Mead, 1965). This method variates the searching area for the best fit according to a set of boundary values, variating the search area in shape and size to find the lowest χ^2 value, after which it shrinks the boundary area to the parameter values of this χ^2 value, setting them as the input parameters. It repeats the process until it returns the input parameters of the lowest χ^2 value it had found. Not only converges this method much faster than the least-squares fit, it is easily extendable when adding more parameters, as needed for the 2D case, and it is able to really converge to a final solution.

3.5.1 Starting values for the Downhill-Simplex method

The least-squares fit showed us that many combinations of the 4 parameters of the two disk fitting function are possible to provide an acceptable fit. Even the Downhill Simplex method has troubles when there are few datapoints for a fitting function with many free parameters or the datapoints show great irregularity.

The Downhill Simplex method requires one to input several sets of starting values in an array which the algorithm will use as boundaries for its fitting area in which it will search for the smallest differences between the datapoints and the model fit function. The parameter space can become huge with many parameters being allowed to vary over a large range. To decrease computation time and make sure the fit gives acceptable results, boundaries have to be set to the parameter space in which the method will search for the lowest χ^2 value. For this the input parameters have to be narrowed down before the actual fitting begins.

Narrowing down the starting values is most important for the vertical profiles. z_n and z_k determine the slope of the two disk components as each describe two different regions of the profile. These values can vary freely between steep and flat if one does not put constraints to this freedom. This can be done by putting a boundary on the values for I_n and I_k who limit how faint or bright the thin and the thick can become in the center of the galaxy, constraining the values z_n and z_k can obtain. For the fit we use the surface brightnesses, μ_n and μ_k, in mag arcsec^{-2}, as input, which are converted into luminosities for the input parameters, because the surface brightness values show the difference better than the larger or smaller luminosity values.

As we are limited by how deep our galaxy images reach, the difference between μ_n and μ_k, which we will address henceforth as μ_{n-k}, is limited for the typical z_k/z_n ratios. μ_{n-k} cannot be too large, as the thick disk will be too faint to be distinguished from the background noise, and not too small, because in that case the thick disk will be too bright and either dominate the profile or be indistinguishable from the thin disk. We have set these two extreme cases, and outer limits, at $\mu_{n-k} = 2$ and $\mu_{n-k} = 6$ mag arcsec^{-2}. So the expected values for μ_{n-k} should be between 3 and 5 mag arcsec^{-2}.

The value of μ_{n-k} is however not something one can easily allow to vary in the Downhill Simplex method. We tried to use the intermediate μ_{n-k} value of 4 for our fits, but this did not result in a free variation of μ_{n-k} and constrained μ_{n-k} and the other starting values too much. Although it was able to always fit the profile and converge to acceptable values, those results were not satisfying as μ_{n-k} only changed in some cases.

The only solution to this was to release the constraints on μ_{n-k} and allow a full parameter range for the fits. However, we still wanted to keep the parameter space small to narrow down on the correct and best solution. To constrain the input parameters we determined them from the actual profile data. We made a sequence of simple linear fits, on the datapoints of the first cut, for the thin and the thick disk, shifting in the z-direction with steps to obtain a range of magnitude and scaleheight values. The most extreme cases were combined to make an additional worst case input set of parameter values to allow the Downhill Simplex method to go search further out for possible solutions. Figure 6 shows an example of this method on the first profile cut of NGC 5290 J. The fits with the same colour in the inner and the outer part represent the thin and thick disk starting values respectively.

h_n and f_h, which are described by a single function, were given a typical range of values for were put into a list, 15–45 and 0.5–3.0 respectively, and separately randomly added to the thin and thick disk starting values.

For some of the sample galaxies we put in an extra constraint if possible. From the radial bulge part three equipositioned cuts were selected and from those the datapoints were taken that were clearly outside the bulge and describing a vertical structure component.

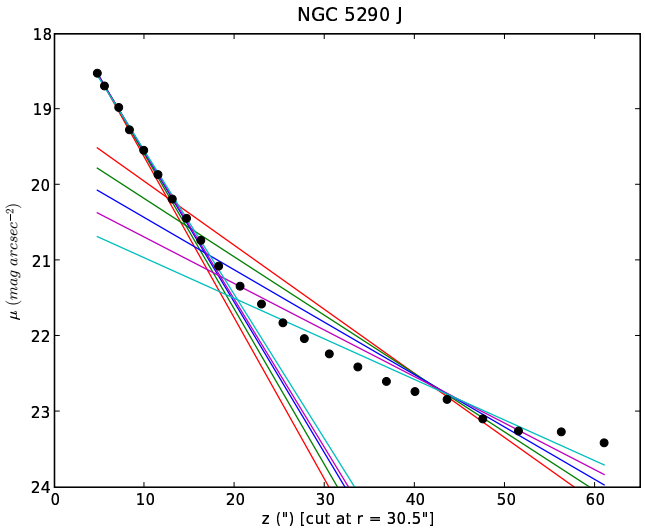

Figure 6: Linear fits to the inner and the outer regions of a profile of NGC 5290 J to create starting values for the Downhill Simplex method. Each combined inner and outer region fit lines have the same colour.

3.6 Weighting

3.6.1 Weighting for 1D fitting

There are many different ways to put a weight to a datapoint for surface brightness measurement. An error can be determined from its dispersion from the average or one adraddressesweighting depending on the position or strength of the datapoint.

In the case of one dimensional fits, weighting is an absolute necessity, because it has not the constraint of the radial behaviour on the other cuts and is more sensitive to variations in its own profile. Each 1D profile can have its own z_n, whereas there is only one z_n for the 2D fit. Because we fit our surface brightness profiles in magnitudes the errors are determined from the variation in the residual background, using the formula

$$\mu_{\pm} \; = -2.5 \log \left(\frac{I_1 \pm 3\sigma}{\text{pixel}^2} \right) \; + \; \text{zeropoint} \; , \tag{15}$$

where I_1 is the intensity of the datapoint, σ the variation in the sky background and pixel the size of the pixel in arcseconds. The logarithmic conversion causes the errorbars to be unequal on the lower and higher side, which makes them difficult to use for correct weighting.

So to retrieve a weighting by error according to the intensity we add the square root of the intensity of each datapoint along the profile, divided by the intensity of the first datapoint to the χ^2 calculation. The square root was used because differences in intensity grow larger rapidly due to its logarithmic behaviour.

3.6.2 Weighting for 2D fitting

Because of the inherent weigthing effect of the two dimensional fit it was decided not to use the typical intensity weighted fit, but allow the Downhill Simplex method to weight all datapoints according to their combined quality to fit to the 2D Two disk model.

Intrinsically the use of a weighting based on the intensity means that the higher the intensity the lower the error. This because a higher brightness will be more accurately detected than a faint brightness. Intensity weighting does not allow for residual structures like unmasked faint stars, which show up as bright peaks in the background noise. These will influence the fit since they get weighted equally as points with the same intensity, giving systematical errors to the fit instead of the normal statistical errors.

Even though using a quadrasized average image minimalizes these peaks there is still a chance that such a false datapoint remains, especially when one side of the residual background has a brighter structure than the other side. For these issues doing a two dimensional fit with the Downhill Simplex method has another advantage over the slightly biased intensity weighting due to bright datapoints in the background noise. The Downhill Simplex method compares the values of each datapoint of each cut with each other. The thin disk component will show up clearly and smooth in each cut and thus will contribute strongly to the determination of its parameter values. The thick disk component however, will be less smooth and on larger radii the thick disk component will start losing signal because we use a surface brightness limit on the profile. The Downhill Simplex method searches for the best fit for all those cuts combined. If a datapoint is erratic and doesn't follow the two dimensional fitting function as well as the datapoints from the other cuts it will automatically contribute less to the fit and get a lower weighting, even if they have a higher intensity in the case of a bright peak in the background noise. This effect showed clearly during our fits.

3.7 Tests on artificial galaxies

An important issue in fitting profiles is the question how well the parametric fitting functions we use are able to reproduce the parameters values of the galaxy. To provide an answer the different fitting functions need to be tested on artificial galaxies for which we can set the parameter values as input. Empirically the fitting functions are quite capable to fit surface brightness profiles, but the question is if they really are able to converge to the input parameters.

We created a three dimensional model of an artificial galaxy with a vertical and radial exponential distribution. Radially we used a broken radial exponential structure (with typical values to the inner and outer scalelength ratio), to account for truncation. We made a model for a thin and a thick disk and added those together. We did line-of-sight integration over the radius to create a 2D artificial image, which will be filtered with the same methods as we use for the sample galaxies. We applied the same binning method as we did for our real data to create vertical profiles. The artifical galaxies we set up resemble our sample galaxies so that we are able to compare the fitting functions ability to reproduce the input parameters. The overall basic input parameters are μ_n = 19.24 mag arsec^{-2}, z_n = 10, h_n = 50 with the truncation, i.e. broken exponential, at $2.5h_n$. The scaleheight of the thin disk was set sufficiently high so it would not be easily dominated by the thick disk component. The remaining parameters were varied to describe galaxies with two vertical disk components.

3.7.1 1D: Test fitting

To test the Sérsic Law and the Generalized Gaussian's ability to recover trends which may change with radius we created an artifical galaxy with a small μ_{n-k}, 3, but distinct thick disk properties: a f_h of 2 and a f_z of 4. As the artifical galaxy has no physical background boundaries a "depth" of the image has to be assumed. To obtain the best comparable profile to our sample we set $\mu_{\rm cut}$ at 7.4 mag arcsec^{-2} from the central thin disk magnitude, which is the largest value from our sample. An artifically deeper dataset at 8.4 mag arcsec^{-2} was also made to see if the behaviour of the resulting fit parameters would change because of the resolution of the image. Another variation was added in the form of a weighted and unweighted test. On a real galaxy one would have to apply weighting to ensure the quality of the fit. On an artificial galaxy weighting should not be necessary to obtain a best fit.

3.7.2 2D: Test fitting

To obtain an indication of the quality of our fitting method and the resulting parameters we selected three artifical galaxies. One with μ_{n-k} is 4, f_h = 2.5 and f_z = 6, one with μ_{n-k} is 3, f_h = 1.0 and f_z = 2 and one with μ_{n-k} is 2, f_h = 1.5 and f_z = 2.5. We set the difference between the central magnitude and $\mu_{\rm cut}$ at 7.4 mag arcsec^{-2}.

To test the influence of disk truncation our radial parameters values two types of model galaxies were created: one with a disk truncation and one without. We use a version without truncation because the Bessel function, which uses line-of-sight integration, assumes the radial behaviour stays the same between r = 0 until ∞, but this is of course not how a typical galaxy behaves radially. The first two galaxies were used for these for different fits. On both galaxy models two 2D Two Disk models were applied: The two dimensional exponential fitting function and the two dimensional Bessel fitting function.

The third galaxy resembles one of the sample galaxies by Yoachim & Dalcanton (2006) to see how our fitting function would respond to such a case.

4 Results

4.1 Sample selection

Thick disks are not easy to determine in late-type disk galaxies compared to early-type galaxies which show much smoother surface brightness profiles compared to the patchy structure of late-type galaxies. In late-type galaxies they are hard to see by eye and one has to apply the disk models to decompose the structure and detect the thick disk component. The galaxy image requires to have a very flat background, a high S/N ratio and a high resolution, to be able to reach to very faint magnitudes, to create high quality profiles.

UGC 3186 proved to be too faint and too disrupted by bright foreground stars in front of the galaxy to obtain workable profiles in either of the bands. The images of NGC 2424 from the UKIRT set had both distorted backgrounds around the galaxy which were caused by a bright star nearby or the moonlight as the Calar Alto image showed a similar effect just outside the range of the galaxy. The contour map of both galaxies (see Appendix A) show this distorted background partially.

The CA set was our initial main sample. Structure decomposition had not been done before in the near-infrared, so we use this as our pilot sample to discover if we could find a thick disk. The UKIRT sample was added to provide a larger sample with more galaxies in the same two bands, but we knew beforehand the image frames of the galaxies were small (as they had originally been intended for study of the bulge) and that it might not be possible to use all galaxies for the profile fits. IC 2531 and NGC 973 had to be rejected from the fit.

The late-type edge-on galaxies of the CA set were selected according to the allocated observing time and for being undisturbed. Although it turned out that some contained bulges that were tilted with respect to the disk, this was not problematic. This was not the case for NGC 5348. As one can see on the left and right side on the contour map (see Appendix A), the galaxy has an U-shaped warp. This makes it very complex to create an average quadrasized galaxy, but even 1D profiles on either of the four sides will have an up- or downbending of intensity in the outer part. Fitting vertical profiles which do not follow a straight line in radius, but a 'line of nodes', is very complex to do, so it was decided not to use NGC 5348.

In the end, out of 20 data-reduced galaxy images, only 11 remained for the profile fit. An S0 galaxy, observed in the V-band, of which we already knew it had a thick disk (see Pohlen et. al. 2004) and two low-mass Sd galaxies, observed in the R-band, for comparison with Yoachim & Dalcanton (2006), as noted in Section 2.1, were added to expand the range of galaxy types and be able to test our methods and results with literature data. Obviously those did not create issues for creating profiles.

4.2 1D: Constrained two disk fits

Two galaxies were selected for a test of the 1D constrained two disk fit. We selected on the basis of a clearly present thick disk component in the profiles, but with a low thick disk scaleheight. IC 3322A and NGC 5981, both in the J-band, were chosen. An outer limit was determined by comparing the shape and extent of the different vertical profiles to see where the noise clearly started to dominate. For both galaxies $z_{\max}$ was set at 30 arcseconds. No lower surface brightness limit was set as the fit is weighted with the intensities. $z_{\min}$ is the same for the 2D Two Disk fit (see Table 11), determined at where the flattening of the inner part of the profile started, which is approximately equal to two times the FWHM. For each quadrant we determined the average or mean, depending if they deviated by more than 0.3 arcseconds, of z_n for each cut by selecting 4–5 datapoints of the inner part of the profile and fitting a linear slope to it. The thin disk scaleheight is given in the title of each subtable of Tables 8 and 9.

TABLE 8

IC 3322A J

1D: Constrained Two Disk Fit Results

A: Upper North-West [$z_n = 4.1$]

χ^2	r [″]	μ_n [mag/□″]	μ_k [mag/□″]	f_z
(1)	(2)	(3)	(4)	(5)
–	30.5	–		
–	34.1	–		
0.0053	38.0	18.33	22.95	8.65*
0.0151	42.4	18.49	22.33	4.19
0.0257	47.1	18.66	22.22	3.57
0.0593	51.9	19.05	21.73	3.02
0.0387	57.4	19.58	21.43	2.64
0.0815	63.4	20.97	20.51	1.80*
0.0065	70.1	20.19	21.83	2.83*
0.0663	77.2	21.05	21.16	2.00*
0.0484	84.7	20.32	23.41	8.78*

B: Lower North-West [$z_n = 3.6$]

χ^2	r [″]	μ_n [mag/□″]	μ_k [mag/□″]	f_z
(1)	(2)	(3)	(4)	(5)
0.0225	30.9	18.38	21.59	4.36
0.0340	34.1	18.42	21.95	4.77
0.0143	38.0	18.60	21.36	3.19
0.0338	42.4	18.80	21.12	2.54
0.0169	47.1	18.79	22.48	6.40
0.0181	51.9	18.85	23.06	9.60*
0.0277	57.4	19.14	22.37	4.01
0.0982	63.4	19.63	21.79	2.88
0.0349	70.1	19.78	21.82	2.72
0.0242	77.2	20.27	21.33	2.00*
0.0225	84.7	19.97	23.67	9.56*

C: Upper South-East [$z_n = 4.1$]

χ^2	r [″]	μ_n [mag/□″]	μ_k [mag/□″]	f_z
0.0244	30.9	18.36	22.35	3.90
0.3393	34.5	18.99	19.71	1.38*
0.0576	38.0	18.50	22.58	3.70
0.0206	42.4	18.65	22.90	6.12
0.0231	47.1	18.93	22.27	3.69
0.0206	52.3	19.34	21.55	2.45
0.1572	57.8	20.71	20.32	1.57*
0.1354	63.8	21.06	20.61	1.56*
0.0510	70.1	20.38	22.15	2.71
0.0572	77.2	20.50	22.73	3.07

D: Lower South-East [$z_n = 4.0$]

χ^2	r [″]	μ_n [mag/□″]	μ_k [mag/□″]	f_z
0.0144	30.9	18.73	21.96	3.92
0.0485	34.5	18.75	22.19	3.33
0.0089	38.0	18.89	21.78	3.09
0.0762	42.4	20.76	19.40	1.33*
0.0280	47.1	19.09	21.49	2.37
0.0344	52.3	19.06	21.99	2.88
0.0154	57.8	19.15	23.01	6.34
0.0445	63.8	19.66	21.33	1.95*
0.0596	70.1	19.48	22.82	2.99
0.1554	77.2	19.83	22.05	1.98*

Notes: (1) See Section 3.6 for the defitinion. (2) central radial position of the bin. (3) Thin disk central surface brightness. (4) Thick disk central surface brightness. (5) Thick disk/thin disk scaleheight ratio. * cuts not taken into account for determining the average parameters.

The results are shown in Table 8 and 9 for IC 3322A and NGC 5981 respectively. The tables are set in sets of four, for each quadrant of the galaxy. For IC 3322A J we found an average z_n of 3.9 ± 0.4 arcseconds and an average f_z of 3.7 ± 1.2 with an average μ_{n-k} of 3.0 ± 0.7 mag arcsec^{-2}. We chose to represent μ_{n-k} as this value gives a good indication of the brightness difference between the thin and the thick disk. For NGC 5981 J we found a z_n of 3.1 ± 0.4 arcseconds and a f_z of 3.9 ± 1.7 with a μ_{n-k} of 3.7 ± 1.0 mag arcsec^{-2}.

The cuts in the tables marked with a * were not used to determine the average parameter values as they either contained background structure making f_z too large to be trustworthy, were partially masked or contained other irregularities that made the fit doubtful. We were not able to fit all profiles due to residual background structures or too heavy irregularities in the profile.

One can clearly see a lot of variation in the results and that the results are very sensitive to the local intrinsic vertical structure of the galaxy. It is hard to see any trends, especially in the case of NGC 5981 which has many cuts which could not be fitted.

TABLE 9

NGC 5981 J

1D: Constrained Two Disk Fit Results

A: Upper North-West [z_n = 3.1]

χ^2	r [″]	μ_n [mag/□″]	μ_k [mag/□″]	f_z
0.0109	21.4	17.22	22.09	5.94
0.0382	24.2	17.23	22.38	6.52
0.1234	27.3	17.39	21.27	2.83
0.0248	30.5	17.39	22.95	9.17*
0.1103	34.1	17.51	21.89	3.45
0.0251	38.0	17.53	23.54	8.65*
–	42.4	–		
–	47.1	–		
0.0260	51.9	18.60	19.82	1.49*
0.3152	57.4	18.94	20.19	1.58*

B: Lower North-West [z_n = 3.3]

χ^2	r [″]	μ_n [mag/□″]	μ_k [mag/□″]	f_z
0.1121	21.4	18.00	20.90	2.61
0.0434	24.2	17.97	22.02	4.94
0.0384	27.3	18.05	21.95	3.79
0.0315	30.5	18.14	21.85	2.88
0.0575	34.1	18.59	20.11	1.64
0.0188	38.0	18.41	21.73	2.68
0.1352	42.4	18.45	22.38	2.79
–	47.1	–		
–	51.9	–		
–	57.4	–		

C: Upper South-East [z_n = 3.3]

χ^2	r [″]	μ_n [mag/□″]	μ_k [mag/□″]	f_z
–	21.8	–		
–	24.6	–		
–	27.3	–		
0.3317	30.9	17.79	23.00	8.12*
–	34.5	–		
0.0640	38.0	18.17	22.06	3.27
0.0319	42.4	18.40	21.82	2.88
–	47.1	–		
0.1280	52.3	18.89	21.45	2.42
0.4340	57.8	19.16	22.32	3.59
0.0744	63.8	20.84	20.72	1.98*

D: Lower South-East [z_n = 3.0]

χ^2	r [″]	μ_n [mag/□″]	μ_k [mag/□″]	f_z
0.0652	21.8	17.49	22.17	5.95
0.0344	24.6	17.54	22.98	11.94*
0.0407	27.3	17.66	22.71	7.99*
–	30.9	–		
0.0321	34.5	17.94	22.84	7.70*
0.0140	38.0	18.18	22.47	5.22
0.0401	42.4	18.74	20.63	2.13
0.1170	47.1	18.84	22.03	3.54
0.0397	52.3	19.28	21.96	3.88
–	57.8	–		
–	63.7	–		

Notes: See Table 9 for a description.

4.3 1D: Alternative fitting function fits

For the test with alternative fitting functions we selected the galaxy IC 3322A J, which showed in the 1D constrained two disk fit a good set of profiles. The best quadrant of the galaxy was the lower north-west quadrant, which was the one we used to compare to the alternative fitting functions. The results are shown in Table 10.

An attempt to do a Sérsic Law fit on IC 3322A resulted in parameters values we could not discuss or derive conclusions from. Since the Generalized Gaussian proved to provide acceptable parameter values and artifical galaxy tests showed no difference between the Generalized Gaussian and the Sérsic Law in the matter of fit quality, we decided to only use the Generalized Gaussian (see Section 4.8).

The results are shown in Table 10B. A plot of the two fits on the first profile is shown in figure 7 where the red line represents the 1D Constrained Two Disk fit and the blue line the Generalized Gaussian fit. For easy comparison the 1D Constrained Two Disk fit table of the same area has been added. The value for λ stays for a range of f_z values rather constant, showing where the general good fit lies. This is also directly related to r_0 which behaves similarly. The values for μ_0 show no coherency, but unlike the constrained two disk fit the inner part is not constrained, which is probably the cause for this. The main problem with the results from the Generalized Gaussian is the interpretation of the parameter values, as there is no trend visible and the parameters are more erratic. So our idea of using less parameters and create a more stable fit because less parameters are less sensitive to irregularities, did not work out

TABLE 10

IC 3322A Alternative Fitting Function Fit Results

A: 1D Constrained Two Disk Fit [$z_n = 3.6$]					B: Generalized Gaussian Fit			
χ^2	r [″]	μ_n [mag/□″]	μ_k [mag/□″]	f_z	χ^2	μ_0 [mag/□″]	r_0 [″]	λ
(1)	(2)	(3)	(4)	(5)	(6)	(7)	(8)	(9)
0.0225	30.5	18.38	21.59	4.36	0.1505	15.3	0.11	0.37
0.0340	34.1	18.42	21.95	4.77	0.2891	15.3	0.12	0.38
0.0143	38.0	18.60	21.36	3.19	0.0318	15.3	0.12	0.38
0.0338	42.4	18.80	21.12	2.54	0.1790	16.8	0.58	0.50
0.0169	47.1	18.79	22.48	6.40	0.2302	15.8	0.11	0.37
0.0181	51.9	18.85	23.06	9.60	0.3104	15.3	0.06	0.34
0.0277	57.4	19.14	22.37	4.01	0.4245	16.0	0.12	0.38
0.0982	63.4	19.63	21.79	2.88	0.7514	16.2	0.09	0.36
0.0349	70.1	19.78	21.82	2.72	0.3270	17.6	0.42	0.45
0.0242	77.2	20.27	21.33	2.00	0.3283	19.3	2.31	0.70
0.0225	84.7	19.97	23.67	9.56	0.4149	16.0	0.02	0.29

Notes: (1)(6) See Section 3.6 for the defitinion. (2) central radial position of the bin. (3) Thin disk central surface brightness. (4) Thick disk central surface brightness. (5) Thick/thin disk scaleheight ratio. (7) Central surface brightness. (8) Width of the distribution. (9) Shape parameter.

TABLE 11

2D Two Disk Fit Results

Galaxy	Filter	μ_n [mag/□″]	μ_k [mag/□″]	μ_{n-k} [mag/□″]	z_n [″]	z_k [″]	f_z	h_n [″]	f_h	#pts	#cuts	$\chi^2_{\nu,1}/\chi^2_{\nu,2}$	f_b	$R_{\rm min}$ [″]	$R_{\rm max}$ [″]	$z_{\rm min}$ [″]
(1)	(2)	(3)	(4)	(5)	(6)	(7)	(8)	(9)	(10)	(11)	(12)	(13)	(14)	(15)	(16)	(17)
IC 3322A	J	17.85	21.26	3.4	4.1	14.2	3.4	28.2	1.2	142	11	4.4 (3.7)	1.09	30	85	5.0
IC 3322A	K'	16.41	22.02	5.6	3.5	24.6	7.0	24.0	2.4	130	11	2.8 (3.7)	1.08	30	85	2.5
NGC 2424	J	17.23	21.68	4.5	3.8	26.2	6.9	23.4	1.2	125	10	7.4 (3.3)	1.09	30	85	6.0
NGC 2591	K'	16.27	21.50	5.2	4.3	21.1	5.0	26.0	3.4	142	12	5.1 (4.0)	1.09	13	56	4.0
NGC 5290	J	16.65	21.23	4.6	4.7	33.8	7.2	24.8	2.1	255	12	39.6 (4.0)	1.07	30	80	4.0
NGC 5290	K'	15.70	20.80	5.1	4.4	33.7	7.7	25.6	1.8	230	12	13.9 (4.0)	1.07	30	80	4.5
NGC 5981	J	16.42	20.27	3.9	2.7	9.0	3.3	21.5	1.3	131	12	5.0 (4.0)	1.09	20	75	2.0
NGC 1886	J	16.40	21.33	4.9	2.8	12.2	4.3	18.9	1.2	207	13	2.2 (4.3)	1.07	15	44	3.0
NGC 1886	K'	15.31	19.53	4.2	2.6	7.6	3.0	18.2	1.6	171	12	1.8 (4.0)	1.09	15	44	3.0
UGC 4277	J	17.60	21.52	3.9	3.1	20.0	6.5	21.8	0.6	132	10	4.6 (3.3)	1.10	15	46	3.0
UGC 4277	K'	16.19	20.61	4.4	2.5	18.7	7.5	19.9	1.0	95	9	5.9 (3.0)	1.12	15	46	3.0
NGC 4179	V	19.17	22.98	3.8	7.0	24.8	3.6	22.1	3.2	241	9	19.5 (3.0)	1.07	35	75	4.0

Notes: (1) Galaxy. (2) Filter. (3) and (4) thin and thick disk central surface brightness respectively. (5) Difference between μ_n and μ_k. (6) and (7) thin and thick disk scaleheight. (8) Thin/thick disk scaleheight ratio. (9) Thin disk scalelength. (10) Thin/thick disk scalelength ratio. (11) and (12) number of datapoints and cuts respectively. (13) Ratio of the reduced χ^2 of the single disk fit and the two disk fit. (14) Bin growing factor. (15) and (16) Inner and outer radial boundaries for the selected profiles. (17) minimum z-position where the inner flattened part of the profile was removed.

4.4 2D: Two disk (thin + thick) Fits

For our 2D Two Disk fits we made use of equation 12 as the Bessel function will return scalelength values which we can compare better with results from the literature. The results and boundary parameters and binning factor of the fits are listed in Table 11. A selection of the vertical profiles is shown in Appendix A in a set of four panels, containing the charactistic bending in the outer part of the vertical profile, resembling a thick disk, together with the two and one disk fit and the individual thin and thick disk component to the fit.

For each galaxy the number of datapoints and cuts are given. $\chi^2_{\nu,1}/\chi^2_{\nu,2}$ is the ratio of the reduced χ^2 for the 1D Single Disk exponential fit for each cut of the dataset and the reduced χ^2 for the 2D Two Disk fit over the whole dataset, and gives a measure of the quality of the thick disk component. Following Wadadekar et. al. (1999), we use this ratio and not the reduced $\chi^2_{\nu,x}$, because we want to compare the quality of the fitted thick disk components, as a six parameter fit will naturally provide a better fit. With each ratio a break ratio is given, which is the ratio between the total number of free parameters for each of the two fits. As the 1D Single Disk fit is not radially related the degrees of freedom accumulate depending on the amount of profiles and are thus different for each galaxy. For example, if there are 12 cuts the number of free parameters for the single disk fit will be 12 times 2 parameters; 24 in total. For the 2D Two Disk fit the parameters include one dataset containing all profiles and will thus be only 6. The break ratio is then $24/6 = 4$. The higher the ratio is above the break point the better the two disk fit is compared to the one disk fit. At the break point both fits are equally good.

An import remark has to be made however. When using a $\mu_{\rm cut}$ as a lower boundary for the fits, the elliptic shape of the galaxy causes the outer cuts to lose signal in the z-direction. This causes a systematic effect that the thick disk component becomes smaller at larger radius. This causes a systematic decrease of the quality of the contribution to $\chi^2_{\nu,1}/\chi^2_{\nu,2}$ towards the outer cuts, causing $\chi^2_{\nu,1}/\chi^2_{\nu,2}$ to be lowered as well. Since this effect is not truly systematic, and different for each galaxy, we cannot correct for this effect. Another issue is that a single disk fit would not fit itself to the dominating thin disk component but chose an intermediate slope to minimize the difference between the datapoints.

$R_{\rm min}$ and $R_{\rm max}$ are the boundaries of the inner disk, excluding the bulge region on the one side and the outer disk on the other side (see Section 3.4.1). The radial fit was taken within these boundaries. $z_{\rm min}$ is where the vertical profile in the inner part showed flattening and we decided to remove those inner datapoints.

What one notices is that the values of μ_{n-k}, f_z and f_h stay within certain limits. The μ_{n-k} values lie close together: 4.5 ± 0.7 mag arcsec^{-2}. f_z varies considerably, giving an average value of 5.6 ± 1.9. Both values are higher than found in previous research. f_h is set at 1.6 ± 0.8 which is nicely within literature boundaries. The result of NGC 4179 is not included in the averages, as it is a different galaxy type while we want to compare the typical results for late-type galaxies. Within these boundaries we can speak of an average thick disk with these three fundamental parameters, with which one will find most likely the correct thick disk component for late-type disk galaxies according to our sample and fitting method.

During the fits we noticed the Downhill Simplex method to show a certain coupling between μ_{n-k} and f_h while trying to converge to the lowest χ^2. In some cases it made μ_{n-k} smaller by decreasing f_h and similarly it increased μ_{n-k} as it increased f_h, while the other parameters hardly changed. As it is not possible to determine in which cases this effect appears, it does allow us to explain certain low or high values for μ_{n-k} and f_h in some cases in combination with their other parameter results.

4.4.1 Comments on individual galaxies

Over our sample the J-band surface brightness profiles showed more distinct and smoother thick disk components than the K'-band profiles, which shows that the J-band data are deeper compared to the K'-band data. The very late-type low-mass galaxies FGC 2339 and IC 5249 could not be fitted with the 2D Two Disk model and are discussed in Section 4.5.

IC 3322A: The J-band profile of the galaxy shows a weak but distinct thick disk component, which shows in the low values for μ_{n-k}, 3.4 mag arcsec^{-2}, and f_z, 3.4. The K'-band results show an extremely high μ_{n-k}, 5.6 mag arcsec^{-2}, and a much flatter thick disk with a f_z of 7.0. However, its profile shows the thick disk much less distinct and the $\chi^2_{\nu,1}/\chi^2_{\nu,2}$ is below the break point, which makes the quality of the fit not good. An attempt to use larger f_b values did not improve the quality of the profile. The high f_z value, compared to the low value of the J-band, does hint that μ_{n-k} is too large.
NGC 1886: This is the only case in which no clear hint of a thick disk or an extended vertical structure is seen in either of the bands, although the J-band results seem to hint at some slight flatter structure at the high z. In the K'-band profile nothing can be seen. The $\chi^2_{\nu,1}/\chi^2_{\nu,2}$ ratios clearly support this. However, considering the other results, which show μ_{n-k} larger than 5 mag arcsec^{-2} and f_z values of only 3.4, the thick disk component can be too faint or too steep to be seen in this profile and thus cannot be excluded to be still possibly existing. Deeper surface photometry would solve the unanswered result for this galaxy as it is the only one from our sample not showing a thick disk component.
NGC 2424: A strong thick disk component can be seen in the profiles. μ_{n-k} is with 4.5 mag arcsec^{-2} moderate, while the f_z with 6.9 is high, but not too extreme.
NGC 2591: μ_{n-k} shows to be quite high with 5.2 mag arcsec^{-2}, while f_z remains moderate compared to the other results with 5.0. f_h however is quite high with 3.4 and seems out of place, but if one couples this to the high μ_{n-k}, this can be seen as overrated by the fitting effect we described earlier. The thick disk component is somewhat weak but still distinct enough to be recognized.
NGC 4179: The only early-type galaxy, which was used to compare it to previous fit results by Pohlen et. al. (2004). A clear thick disk component is seen and the fit, after conversion, matches their results decently, with μ_n = 20.2 mag arcsec^{-2}, μ_n = 22.9 mag arcsec^{-2}, μ_{n-k} = 2.7 mag arcsec^{-2}, f_z = 3.1 and f_h = 2.0. Our results show a fainter and flatter thick disk (μ_{n-k} = 3.8 mag arcsec^{-2}) with also a quite higher scalelength ratio (f_h = 3.23). If this is a case where a high f_h is coupled to a high μ_{n-k} this could explain the difference with these numbers to the results of Pohlen et al. (2004).
NGC 5290: In this galaxy the thick disk is shown to be more extended, and more shallow, with a very large scaleheight ratio of 7.2 in the J-band and 7.7 in the K'-band, higher than any previous research results. μ_{n-k} are 4.6 and 5.1 mag arcsec^{-2} respectively. It could be that this is an extreme case, but it can also mean that thick disks can be so shallow that they are very hard to detect. The thick disk structure already shows up strongly above $\mu_{\rm crit}$, supporting that thick disks can be so faint and flat compared to thin disk that they are hard to distinguish from the background if the resolution doesn't go deep enough. For both bands we could make a fit with the lowest starting value of f_b, showing a distinct and smooth thick disk component in both bands. The $\chi^2_{\nu,1}/\chi^2_{\nu,2}$ values are extremely high, dissolving any remaining doubt.
NGC 5981: This galaxy showed to be similar to IC 3322A in its parameter results with a relatively low μ_{n-k} of 3.9 mag arcsec^{-2} and a f_z of 3.3. The thick disk component is also weak and less distinct but still quite visible, while the $\chi^2_{\nu,1}/\chi^2_{\nu,2}$ value is above the break point.
UGC 4277: The profiles of this galaxy showed quite a lot of bumps in the profiles that could not be removed easily by making f_b larger. For the K'-band profile we had to resort to a f_b of 1.12 to be able to fit the distinct thick disk component we saw in both profiles. Too large bins caused the profile the flatten more, especially in the outer part where the thick disk component was already not that steep. The bins also lose some of the thick disk datapoints because the

larger bins take more background noise into the average. This can make the average intensity drop if they are all very low. The J-band results show a quite flat thick disk, with a f_z of 6.5, but f_h is unusually low with 0.6. As a flat thick disk can be coupled with being much fainter than the thin disk, this low number can also explain the relatively low value for μ_{n-k} at 3.9 mag arcsec^{-2}. During the fitting the coupling between μ_{n-k} and f_h was clearly noted, so these low values could be a systematic effect. As the K'-band f_z is quite high with 7.5, and we had to resort to large bins we consider the J-band results to represent the thick disk parameters better.

4.4.2 Intrinsic values of the 2D two disk results

Table 12 shows the results and input parameters of our fits converted to intrinsic sizes together with the thin and thick disk values of the Milky Way in the near-infrared (see Ojha 2001) for comparison. Additionally the ratio between the total luminosity of the thick and the thin disk is given. The luminosity ratios were determined with the formula

$$L_{\rm tot} \; = \; 4\pi h^2 z_0 L_0 \; , \tag{16}$$

taken from Van der Kruit & Searle (1981a), where h is the scalelength, z_0 the scaleheight and L_0 the central luminosity, calculating the total luminosity for the thick and the thin disk and dividing them. The average luminosity ratio is 0.21 ± 0.13. It has to be noted for equation 16 it is assumed that there is no truncation over the radius, causing the total luminosity to be overestimated. As we use a ratio of two total luminosities, this value is not much effected by this overestimation.

Most of our thick disk component have a higher scaleheight than the Milky Way. It only resembles our galaxies with the lowest thick scaleheight. NGC 5290, which in mass and size can be compared best to our Milk Way is far more extended than the Milky Way for its thin and thick disk components.

TABLE 12
2D Two Disk Fit Results in Parsecs

Galaxy	Filter	z_n [pc]	z_k [pc]	h_n [kpc]	$R_{\rm min}$ [kpc]	$R_{\rm max}$ [kpc]	$z_{\rm min}$ [pc]	L_k/L_n
IC 3322A	J	300	1030	2.0	2.4	47.3	360	0.20
IC 3322A	K'	250	1780	1.7	2.4	47.3	180	0.23
NGC 2424	J	840	5810	5.2	7.3	145.1	1330	0.16
NGC 2591	K'	460	2280	2.8	1.4	9.1	430	0.45
NGC 5290	J	900	6510	4.8	6.4	62.5	770	0.46
NGC 5290	K'	850	6490	4.9	6.4	62.5	870	0.22
NGC 5981	J	520	1730	4.1	4.0	41.0	380	0.17
NGC 1886	J	300	1280	2.0	1.6	5.8	320	0.07
NGC 1886	K'	270	800	1.9	1.6	5.8	320	0.16
UGC 4277	J	1190	7720	8.4	5.9	22.9	1160	0.06
UGC 4277	K'	960	7220	7.7	5.9	22.9	1160	0.13
NGC 4179	V	610	2150	1.9	3.0	6.5	350	1.11
Milky Way	NIR	260	860	2.8				

Notes: See Table 12 for a description. L_k/L_n is the ratio of central luminosities of the thick and the thin disk.

The luminosity ratios are in three of four cases higher in the K'-band except for NGC 5290. This is also the only galaxy where the scalelength of the thin disk is smaller in the J-band than the K'-band, which is quite unexpected, as it is commonly found to be larger in the J-band. The luminosity ratio given by Pohlen et. al (2004) for lenticular galaxies is somewhat lower than

ours: 0.81 to 1.11. Yoachim & Dalcanton (2006) find thin disk scaleheights around that of the Milky Way (200–1000 pc). Only those of the high-mass galaxies are higher (800–1100 pc). This result is somewhat strange, as the Milky Way is a high-mass galaxy. Their thick disk scaleheights (600–1100 pc) are similar to the Milky Way's thick disk scale-height, their high-mass galaxies still giving higher values (1100-1400 pc). Only our galaxies with less prominent bulges, IC 3322A and NGC 5981, represent their results but NGC 5981 is more massive, and thus does not seems to represent mass and scaleheight coupling of Yoachim & Dalcanton (2006) that well. Overall most of our galaxies give much larger scaleheights for the thin and the thick disk.

4.5 1D: Single disk fits

Our additionally added very late-type and low-mass galaxies FGC 2339 and IC 5249 could not be fitted with the 2D Two Disk fit or the 1D Constrained Two Disk fit. This is not due to a lack of a second vertical component. As we could see in NGC 1886 J it would still give fit results. In both galaxies a vertical structure is visible. Although it is faint for FGC 2339, both seem to have a too flat second component. This makes it hard for the fitting function, as it has to sum two exponential functions and gives higher scaleheight values tot the second component to describe it, after which it will start to increase rapidly to unphysical values. A similar thing happened to the scalelength of both the thin and the thick disk, showing that the intensity stays rather flat over radius. This behaviour was in strong contrast to the Two Disk model's ability to fit the other sample galaxies without problems, confirming the vertical structures seen to be thick disks. Thus the only remaining option to be able to present quantitative numbers is the 1D Single Disk fit.

Only two parameters are needed to fit with the 1D Single Disk fit, μ_0 and z_0. For FGC 2339 f_b was set to 1.10 and we used an $z_{\rm min}$ of 1.5 arcseconds to avoid the inner flattening; for IC 5249 f_b was set to 1.08 and a $z_{\rm min}$ of 2.5 arcseconds was used. Tables 13A and 13B show the fit results of each cut of the quadrazised average galaxy, for FGC 2339 and IC 5249 respectively. See Appendix A for plots of the vertical profiles and the single disk fit. The quadrasized average was chosen because it would constrain z_0 better in its variation and due to the flat radial behaviour of the thin and thick disk intensity the vertical structure will not disappear at higher radius because of the $\mu_{\rm cut}$ value. For the fit equation 5 was used. The fitting was done with the Levenberg-Marquardt least-squares algorithm, weigthed with the average magnitude error for each datapoint.

The values for z_0 remain reasonably constant, giving a median of 2.1 ± 0.1 arcseconds for FGC 2339 and 3.7 ± 0.1 arcseconds for IC 5249. What shows most notably is the very slow increase of μ_0 over the radius for both galaxies, showing the intensity remains almost flat over the radius of the galaxy. This confirms the 'flat' behaviour of the radial parameters in the 2D Two Disk fit, making it clear that one cannot use this fitting model for these galaxies. The χ^2 values are all quite high, showing that the 1D One Disk fit is not capable of doing a good fit and confirming the existence of a distinct vertical structure, which could not be described by a thick disk.

TABLE 13

1D One Disk Fit Results

A: FGC 2339 R

r [″]	z_0 [″]	μ_0 [mag/□″]	χ^2
2.43	1.94	20.27	29.35
3.24	1.96	20.31	21.68
4.32	2.02	20.37	18.91
5.40	2.07	20.44	19.55
6.48	2.12	20.53	14.89
7.56	2.14	20.60	24.43
8.91	2.17	20.67	16.02
10.53	2.20	20.75	16.68
12.15	2.21	20.79	9.40
13.77	2.18	20.82	10.15
15.93	2.13	20.84	20.66
18.09	1.97	20.80	28.98
20.25	1.97	20.87	34.54
22.95	1.88	20.78	28.04
25.65	1.71	20.61	27.05

B: IC 5249 R

r [″]	z_0 [″]	μ_0 [mag/□″]	χ^2
34.29	3.75	21.25	18.35
37.53	3.83	21.33	41.74
41.04	3.70	21.31	29.72
44.82	3.77	21.39	36.82
49.14	3.68	21.04	25.14
53.46	3.68	21.44	31.03
58.32	3.70	21.05	27.72
63.72	3.77	21.58	40.35
69.12	3.60	21.52	16.46
75.33	4.02	21.67	191.71

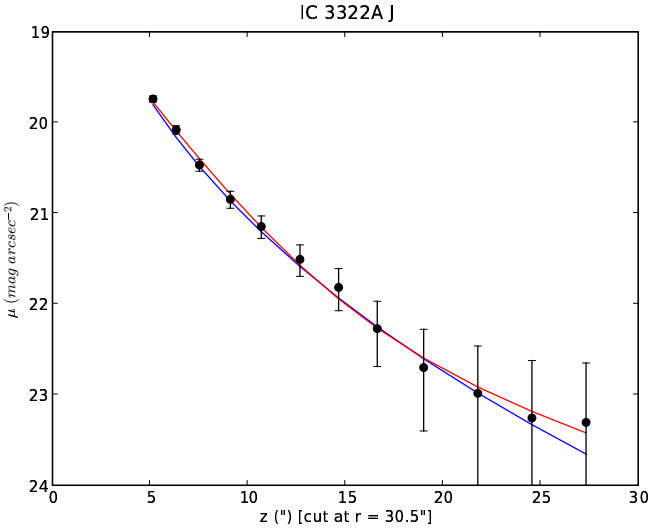

Figure 7: 1D Fit on the first profile of the lower north-west quadrant of IC 3322A J. The black dots are the actual data. The red line is the 1D Constrained Two Disk fit, the blue line is the Generalized Gaussian fit.

4.6 Fits to artifical galaxies

4.6.1 1D: Single disk fits to artificial galaxies

The radial behaviour of $z_0/z_{\rm input}$, determined with single disk weighted least-squares fits, over radius with input parameters ranging from μ_{n-k} is 3–5, f_h is 0.5–3.0 and f_z is 2 to 6, has been plotted in Appendix B for 36 3D artifical galaxies, as described in Section 3.8. The artifical galaxies consist of two vertical components (a thin and a thick disk) to see the radial behaviour of a single disk fit for the various input parameters. The 36 plots have been sorted in three columns according to either growing μ_{n-k}, f_h or f_z. The fits were done to see if there were any notable trends visible from which conclusions coulds be drawn, but we did not see any trends.

4.6.2 1D: Alternative fitting function fits to artifical galaxies

Tables 14 and 15 A1–A2 and B1–B2 show the results of the 1D profile fits with the weighted and an unweighted Generalized Gaussian and Sérsic Law respectively. The artificial galaxy for the fit has the input parameters $\mu_{n-k} = 3$, $f_h = 2.0$ and $f_z = 4.0$, with a truncation at $2.5h_n$, depicting an ideal thick disk galaxy. Two $\mu_0 - \mu_{\rm cut}$ values are used: 7.4 and 8.4 mag arcsec^{-2}. We do this to compare the behaviour of the fit for different depths. μ_0 is the central surface brightness.

What you see immediately is that there is rarely any difference between the χ^2's of both methods, showing they fit evenly well and that using either model suffices with the main differences the parameter results. There are significant differences between the z_0 values of the weighted and the unweighted Generalized Gaussian. A similar thing can be said for the Sérsic Law. At $\mu_0 - \mu_{\rm cut} = 7.4$ the Sérsic Law shows a typical growing trend of a larger scaleheight with radius, as expected from the thick disk's larger scalelength. At $\mu_0 - \mu_{\rm cut} = 8.4$ however, the scaleheight is decreasing with radius. There are also notable differences between the results of the weighted and the unweighted fit, which would not have been expected, as the artificial galaxies provide smooth profiles that are easy to fit. A profile and fit with the weighted Generalized Gaussian is shown in figure 8, A profile and fit with the weighted Sérsic Law is shown in figure 9. Both have $\mu_0 - \mu_{\rm cut}$ set at 7.4 mag arcsec^{-2}. In the inner part a stronger up-bending can been seen, while both fitting functions cannot reproduce the bending to the thick disk component very well.

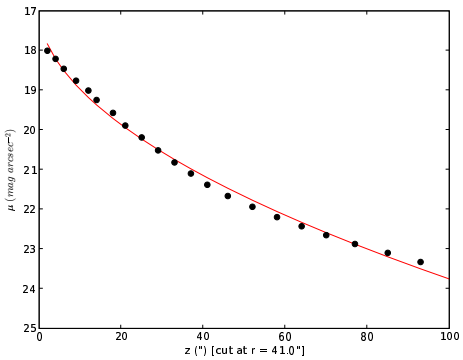

Figure 8: Fit with the Generalized Gaussian to an artifical galaxy.

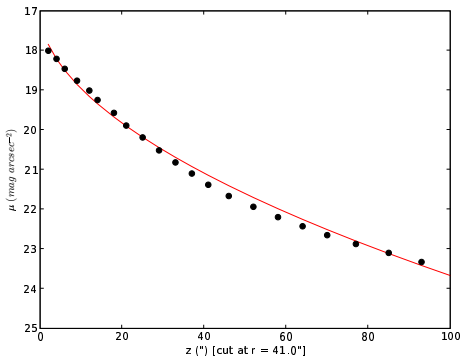

Figure 9: Fit with the Sérsic Law to an artifical galaxy.

TABLE 14

1D Weighted Alternative Fitting Function Results

A1: Weighthed Generalized Gaussian [$\mu_0 - \mu_{\rm CUT} = 7.4$]

χ^2	r ["]	μ_0 [mag/□"]	r_0 ["]	λ
(1)	(2)	(3)	(4)	(5)
0.1392	41.0	16.98	3.16	0.53
0.1342	46.0	17.11	3.42	0.53
0.1301	52.0	17.19	3.40	0.53
0.1244	58.0	17.30	3.42	0.53
0.1134	64.0	17.44	3.62	0.54
0.1081	70.0	17.55	3.63	0.53
0.1023	77.0	17.68	3.65	0.53
0.0959	85.0	17.82	3.67	0.53
0.0850	93.0	18.02	3.90	0.53

B1: Weighthed Sérsic Law [$\mu_0 - \mu_{\rm CUT} = 7.4$]

χ^2	r ["]	μ_0 [mag/□"]	r_c ["]	n
(6)	(7)	(8)	(9)	(10)
0.1383	41.0	15.95	33.47	1.86
0.1342	46.0	16.03	33.99	1.87
0.1296	52.0	16.11	34.60	1.88
0.1244	58.0	16.21	35.29	1.89
0.1134	64.0	16.35	35.46	1.86
0.1081	70.0	16.46	36.30	1.87
0.1023	77.0	16.59	37.26	1.88
0.0959	85.0	16.74	38.36	1.89
0.0850	93.0	16.93	38.99	1.87

A2: Weighthed Generalized Gaussian [$\mu_0 - \mu_{\rm CUT} = 8.4$]

χ^2	r ["]	μ_0 [mag/□"]	r_0 ["]	λ
0.1669	41.0	16.97	3.01	0.52
0.1635	46.0	17.06	3.11	0.53
0.1635	52.0	17.15	3.11	0.53
0.1636	58.0	17.27	3.18	0.53
0.1581	64.0	17.39	3.26	0.53
0.1581	70.0	17.51	3.26	0.53
0.1581	77.0	17.64	3.26	0.53
0.1507	85.0	17.82	3.44	0.54
0.1507	93.0	17.99	3.44	0.54

B2: Weighthed Sérsic Law [$\mu_0 - \mu_{\rm CUT} = 8.4$]

χ^2	r ["]	μ_0 [mag/□"]	r_c ["]	n
0.1669	41.0	15.88	33.03	1.91
0.1635	46.0	15.98	32.77	1.90
0.1635	52.0	16.07	32.77	1.90
0.1635	58.0	16.17	32.77	1.90
0.1581	64.0	16.30	32.41	1.87
0.1581	70.0	16.42	32.41	1.87
0.1581	77.0	16.55	32.41	1.87
0.1507	85.0	16.74	31.96	1.84
0.1507	93.0	16.90	31.96	1.84

Notes: (1)(6) See Section 3.6 for the defitinion. (2)(7) Radial position of the profile. (3)(8) Central surface brightness. (4) Width of the distribution. (5) Shape parameter. (9) Halflight radius. (10) Power law index.

TABLE 15

1D Unweighted Alternative Fitting Function Results

A1: Unweighted Generalized Gaussian [$\mu_0 - \mu_{\rm CUT} = 7.4$]

χ^2	r [″]	μ_0 [mag/□″]	r_0 [″]	λ
0.4426	41.0	16.45	1.44	0.44
0.4204	46.0	16.54	1.47	0.44
0.3964	52.0	16.65	1.51	0.44
0.3704	58.0	16.77	1.56	0.45
0.3390	64.0	16.93	1.71	0.45
0.3139	70.0	17.07	1.77	0.45
0.2875	77.0	17.22	1.84	0.45
0.2602	85.0	17.40	1.92	0.45
0.2289	93.0	17.62	2.12	0.46

B1: Unweighted Sérsic Law [$\mu_0 - \mu_{\rm CUT} = 7.4$]

χ^2	r [″]	μ_0 [mag/□″]	r_c [″]	n
0.4426	41.0	15.36	36.18	2.25
0.4204	46.0	15.45	36.79	2.25
0.3964	52.0	15.56	37.48	2.25
0.3704	58.0	15.68	38.27	2.25
0.3390	64.0	15.85	38.71	2.21
0.3139	70.0	15.98	39.66	2.21
0.2875	77.0	16.14	40.73	2.20
0.2602	85.0	16.31	41.93	2.20
0.2289	93.0	16.54	42.88	2.17

A2: Unweighted Generalized Gaussian [$\mu_0 - \mu_{\rm CUT} = 8.4$]

χ^2	r [″]	μ_0 [mag/□″]	r_0 [″]	λ
0.5255	41.0	16.35	1.25	0.44
0.5252	46.0	16.42	1.23	0.43
0.5252	52.0	16.51	1.23	0.43
0.5252	58.0	16.61	1.23	0.43
0.5235	64.0	16.73	1.27	0.44
0.5235	70.0	16.85	1.27	0.44
0.5235	77.0	16.98	1.27	0.44
0.5150	85.0	17.18	1.36	0.44
0.5150	93.0	17.34	1.36	0.44

B2: Unweighted Sérsic Law [$\mu_0 - \mu_{\rm CUT} = 8.4$]

χ^2	r [″]	μ_0 [mag/□″]	r_c [″]	n
0.5255	41.0	15.26	34.72	2.29
0.5252	46.0	15.33	34.75	2.30
0.5252	52.0	15.42	34.75	2.30
0.5252	58.0	15.52	34.75	2.30
0.5235	64.0	15.65	34.65	2.29
0.5235	70.0	15.77	34.65	2.29
0.5235	77.0	15.90	34.65	2.29
0.5150	85.0	16.09	34.38	2.26
0.5150	93.0	16.26	34.38	2.26

Notes: See Table 15 for a description .

TABLE 16

2D Two Disk Artificial Galaxy Fit Tests Results

Model	μ_n [mag/□″]	μ_k [mag/□″]	z_n [″]	h_n [″]	f_z	f_h	μ_{n-k} [mag/□″]	$\chi^2_{\nu,1}/\chi^2_{\nu,2}$
Input	17.47	21.47	10	50	6	2.5	4.0	
BesTr2.5h_n[a]	17.35 (–0.7%)	21.66 (+0.9%)	10.05 (+0.5%)	43.39 (–15.2%)	5.99 (-0.2%)	2.13 (–17.4%)	4.31 (+7.8%)	701.7
BesNoTr[b]	17.40 (–0.4%)	21.49 (+0.1%)	10.05 (+0.5%)	50.06 (+0.1%)	5.99 (-0.2%)	2.51 (+0.4%)	4.09 (+2.3%)	1624
ExpTr2.5h_n[c]	17.02 (–2.6%)	21.50 (+0.1%)	10.05 (+0.5%)	54.67 (+9.3%)	5.99 (-0.2%)	2.56 (+2.4%)	4.48 (+12%)	387.8
ExpNoTr[d]	17.06 (–2.4%)	21.33 (–0.7%)	10.04 (+0.4%)	62.05 (+24.0%)	5.98 (-0.3%)	3.05 (+22%)	4.27 (+6.8%)	604.8
Input	17.45	20.45	10	50	2	1.0	3.0	
BesTr2.5h_n[a]	17.49 (+0.2%)	19.09 (–7.1%)	9.26 (–8.0%)	43.20 (–15.7%)	1.68 (-19.0%)	1.00 (0.0%)	1.60 (–47.7%)	6.8
BesNoTr[b]	17.53 (+0.5%)	19.26 (–6.2%)	9.39 (–6.5%)	50.48 (+1.0%)	1.69 (-18.3%)	0.98 (–2.0%)	1.73 (–42.3%)	12.0
ExpTr2.5h_n[c]	17.07 (–2.2%)	19.24 (–6.3%)	9.58 (–4.4%)	53.87 (+7.7%)	1.76 (-13.6%)	1.04 (+4.0%)	2.17 (–27.8%)	4.3
ExpNoTr[d]	17.20 (–1.5%)	18.79 (–8.8%)	9.29 (–7.6%)	61.68 (+23.2%)	1.67 (-19.8%)	1.00 (0.0)	1.59 (–47.0%)	5.6
Input	17.45	19.45	10	50	2.5	1.5	2.0	
BesTr2.5h_n[a]	17.40 (–0.2%)	20.03 (+3.0%)	10.03 (+0.3%)	48.96 (–2.1%)	2.49 (-0.4%)	1.45 (–3.4%)	2.63 (+31.5%)	176.8

Notes: [a] Model with Bessel radial function and truncation at 2.5 h_n. [b] Model with Bessel radial function and no truncation. [c] Model with exponential radial function and truncation at 2.5 h_n. [d] Model with exponential radial function and no truncation.

4.6.3 2D: Two disk fits on artificial galaxies

The fitting function and the fitting method were tested on their ability to reproduce the input parameters on three artifical galaxies. For two galaxies the two 2D Two Disk models, with the exponential function and the Bessel function to describe the radial behaviour, were tested on a truncated and an untruncated version. The two selected galaxies describe a strong and a weak thick disk component similar to the parameters we found for our sample galaxies. In total four different fits were done on each galaxy. A third galaxy with thick disk parameters comparable to the more distinct thick disk cases from Yoachim & Dalcanton (2006) was only tested with the Bessel function 2D Two Disk model, as this was the model we used for our sample galaxies. In all cases $\mu_0 - \mu_{\rm cut}$ was set at 7.4 mag arcsec^{-2} so that they represent the quality of our own sample galaxies.

The results of the tests of the 2D Two Disk model on artificial galaxies are shown in Table 16. μ_{n-k} is given to describe the effects of the fits on this value. The $\chi^2_{\nu,1}/\chi^2_{\nu,2}$ value is added to show how much the fitting method fits the thick disk component more clearly in an artificial galaxy than in our sample galaxies.

Considering the scalelengths the Bessel function returns the original values quite accurately for the untruncated case while the exponential fits badly, but this was expected as the 3D galaxies were created with a Bessel function to describe the line-of-sight integration of the disk over the radius. The differences on the truncated case between the Bessel function and exponential fit however, are small, especially considering the scalelength parameters, where one would again expect the Bessel function to perform better.

For the artificial galaxy with a high f_z, the fits return the input accurately. This is not the case for the case with a low f_z, which gives overrations in the range of +13–20%. The same can be said for μ_{n-k}. Although it is higher for the $f_z = 6$ galaxy, the deviations are considerable, but acceptable, while the $f_z = 2$ galaxy underrates it heavily, ranging from –28–48%. That one overrates and the other underrates is also notable, showing varying possible behaviour.

Neither of the two fitting function are well adjusted to a truncation and over all parameters they perform similar. The exponential overrates the scalelength while the Bessel function underrates it. In the case of the Bessel function we see the line-of-site integration fails, even when cutting at a $R_{\rm min}$ and a $R_{\rm max}$ in the case of radial truncation.

The third galaxy, representing one of the more typical thick disk parameters from Yoachim & Dalcanton (2006), gives very different results. We do not see the similar underrating of the other two galaxies to the scale lenght of the thin disk, which is odd compared to the clear different and expected behaviour of the first two sets of fits. All the parameters are fitted quite well, but strangely enough not μ_{n-k}, which it overrates strongly. The cause for this lies at the thick disk component. The overrating is quite surprising, as the μ_{n-k} values of Yoachim & Dalcanton (2006) are typically much smaller than our fitted result.

What we can see is that the less truncated a galaxy the better the Bessel model fits will return the input parameters. Truncation however, is a common radial feature (Kregel et. al. 2000, Pohlen & Trujillo 2006). The tests on our artifical galaxies show that the conversion to a Bessel function to keep the correct scalelength will not be able to do so in most cases. The difference between exponential and Bessel function is neglectable for truncated galaxies.

The importance of the tests on artificial galaxies is that they give an indication of the error of our fit results for the 2D Two Disk fit as it is not possible to obtain clear error margins for the six parameter values except for the speed and accuracy of the convergence of the Downhill Simplex method as it only produces one final result.

5 Discussion

5.1 Existence & parameters of thick disks in late-type disk galaxies

In seven of the ten galaxies we fitted we find a thick disk. Two galaxies show an extended vertical structure that cannot be described by a two component fitting function. One galaxy does not show a clear sign of a thick disk component, although the two component fitting function is able to fit the profiles. The results give thick disks in the range of $\mu_{n-k} \approx 3.4$–5.6 mag arcsec^{-2}, $f_z \approx 3.3$–7.7 and $f_h \approx 0.6$–3.4.

Determining the quality of the fits to the thick disk components in late-type disk galaxies is complicated as the profiles are usually not smooth and the quality is different for each cut. Tests on artificial galaxies (see Section 4.6.3), which have perfect profiles for the outer component showed that the fitting method is often not capable of producing all the correct parameters as were set as input parameters. As we have to find the parameters empirically, it is hard to determine which kind of deviation our results are subject to, especially as the profiles of the sample galaxies have a much lower quality than the artificial galaxies. Because of this we mention here average limits within one can expect to find the thick disk parameters and to not hold unto all the individual results as they can have unknown deviations.

We also noted the possible behaviour of the fit function to couple μ_{n-k} and f_h to improve the fit, but it is not clear when this happens as the profiles of each galaxy are different. With six parameters to fit the profiles there exists a large range of possible solutions for the best fit. However, we showed in our tests on artificial galaxies that our fitting method is able to reproduce the input parameters sufficiently where it concerns the thick disk component in case the real galaxy would follow the model.

In Table 11 three galaxies give a $\chi^2_{\nu,1}/\chi^2_{\nu,2}$ ratio higher than 10, presenting very certain thick disk cases. Three galaxies are below the break point and their fits can thus be considered to be a bad representation of a possible thick disk component. The other galaxies have ratios just above the break point, showing that there is a strong hint for a thick disk, but no absolute certainty as there still exists a risk of being biased by residual background structure causing the thick disk scaleheigth to be overestimated.

Although we are able to fit thick disks in our sample galaxy, most of regions dominated by the thick disk lie under $\mu_{\rm crit}$. This is to be expected as it is faint and hard to detect. Several galaxies show the characteristic bending of a second component just above or around $\mu_{\rm crit}$, which supports the claim for a thick disk component in those galaxies.

The relative scaleheight of the thick disk shows a possible relationship to a vertically extended size of the bulge, which can seen from the contour maps of the galaxies. The high values for f_z for NGC 2424, NGC 5290 and UGC 4277 can be related to those, while the low values of IC 3322A and NGC 5981 can be matched to their small bulges. This might suggest the not seen thick disk component of NGC 1886 is rather shallow as is has a strong bulge component.

Overall, the thick disk parameters all point at faint thick disks and higher scaleheights for late-type disk galaxies, as previous results gave μ_{n-k} of 4 mag arcsec^{-2} and f_z values no higher than 6.5 (see Section 5.4).

5.2 1D two disk model versus 2D two disk model

We performed a 1D Constrained Two Disk fit and a 2D Two Disk fit on two galaxies so we could compare the respective results. For IC 3322A J the μ_{n-k} of the 1D fit is somewhat smaller than the 2D fit, but within its errors. The values of z_n are quite close and can be considered to be a robust match. f_z is for the 1D fit higher than the 2D fit, but this value has a high error range. For NGC 5981 J the μ_{n-k} value matches better, but z_n is much higher, while f_z is also quite higher in the 1D fit. These higher values are somewhat surprising as one might expect the quadrasized average galaxy to flatten and smoothen the profile as it takes averages of all four sides, but the

opposite is the case in our results.

Although the results of the 1D and the 2D fit do not deviate much, the results of the 2D fit are an average wherein the contribution of the individual cuts are weighted to their quality to fit the model in comparison with the other cuts. This is not the case for the 1D Two Disk model. Profiles had to be removed to acquire representative thick disk parameters for the average. This selection, although appropriate enough, gives equal weight to each profile for calculating the average while it is impossible to make a weighting depending on the quality of the profile. This shows in the large range of parameter results. The most important conclusion from the comparison is that the 2D Two Disk fit gives similar results as the 1D Two Disk Fit, thus confirming the quality of the 2D Two Disk fit results.

5.3 Vertical structures revisited?

FGC 2339 and IC 5249, both low-mass galaxies, could not be fit with the Two Disk models, while the Single Disk fit gave very high χ^2 values, showing the existence of a vertical structure at higher scaleheight that is clearly distinct from a single thin disk. This vertical structure however, cannot be described as a superposition of a thin plus a thick disk. A study of the shape on contour maps and the radial surface brightness profiles (see Appendix A) shows both galaxies to possess a extended box shaped structure. This is especially strong in IC 5249 which shows a long radial range in which the surface brightness hardly decreases. Also in the contour map the isophotes remain very parallel to the major axis. What these flat vertical structures are we cannot say. It could be a long bar or (multiple) inner rings within the galaxy, which affects the vertical structure along the whole z-region. We show here that they are not thick disks in the traditional sense; as a superposition of a thin and a thick disk is not a valid description of the vertical structures we see. This in contrast to the easy fits on our other sample galaxies.

A reassessment of the vertical structures in (low-mass) late-type galaxies might be necessary. The question is that we don't know if what we see is something like a thick disk or a completely different structure. Our findings resemble the findings of Matthews (2000), who suggests that the superthin edge-on Sd galaxy UGC 7321 has multiple disk subcomponents with different scaleheights, comprised of stellar populations with different ages and velocity dispersions. FGC 2339 and IC 5249 could be similar galaxies to UGC 7321.

The issue could also be that low-mass galaxies have not developed a thin with thick disk structure and can not be used to determine a distinct thick disk component. A thick disk might require more mass and potential energy to develop a thick disk component. All in all this will have its implications on the hypotheses on the formation and evolution of galaxies.

5.4 Comparison with literature

The main problem when comparing our results with literature is the wide variety in methods used to do the fits and hence obtain the thick disk parameters. Comparison of our results with literature is complicated, as few structure decompositions have been performed with some of them on the same galaxy and even fewer on late-type galaxies. We present the previous results in Table 17, which is adapted from Pohlen et al. (2004). μ_{n-k} is also shown where possible to compare the faintness of the thick disk compared to the thin disk.

Our lower values for f_z match previous found values, but our higher values exceed any previous values, although Morrison et. al. (1997) find a possible f_z of 6.3 for NGC 891. The fact that the galaxy with our highest f_z is also the galaxy in our sample with the most distinct thick disk component makes this extreme value hard to challenge. It also shows thick disks can be very flat and thus harder to distinguish from the background noise.

Our f_h values give little rise to discussion as they are similar to previous results. Although we find some low and high values, these could be explained by the fit due to a possible coupling with μ_{n-k}. Our μ_{n-k} values encompass earlier results. The values from Pohlen et. al. (2004) are

lower, but this could be caused by the different modelling method or the coupling effect of the fit. We also find several much larger μ_{n-k} values. The only other result of such a large value is from Van Dokkum et. al. (1994). During our fits we noted that a μ_{n-k} of 5.6 mag arcsec^{-2} is an extreme maximum for the fit function with our surface brightness limit, and this kind of difference between surface brightness makes the fit degenerate as the fitting function can fit almost any thick disk scaleheight to such a larger difference in surface brightness if the thick disk is not as distinct as for NGC 5290. The low f_z of Van Dokkum et. al. (1994) however, does not correspond to the typical degeneracy. They also used a 1D fit which showed in our tests to result in a larger μ_{n-k} than the 2D fit and they used radially larger binned profiles to determine the fit, which could be of influence.

The use of radially larger binned profiles (this to increase the S/N ratio) than we did to determine vertical disk components is also used in Neeser et. al. (2002) and Abe et. al. (1999). Neeser et. al. (2002) first create many vertical bins with small equal widths and then average those in larger bins, with the bins growing larger over radius. Their summed bins are very large compared to our binsizes which we need to keep small to have sufficient cuts for a trustworthy 2D fit, where they use a 1D fit. Their low f_z, in contrast to their high μ_{n-k}, makes the possible thick disk component seem hard to distinguish from the thin disk.

TABLE 17
Literature Thick Disk Results

Galaxy	Type	Model	f_z	f_h	μ_{n-k}	Reference[a]
11 galaxies	Sb–Sc	exp+exp	3.3–7.7	0.6–3.4	3.4–5.6	This Study
34 galaxies	Sd	sech$^{n/2}$+sech$^{n/2}$	1.4–4.0	0.6–1.7	-0.8–3.5	YO06
5 galaxies	S0	sech+sech	2.6–5.3	1.7–1.9	2.2–3.0	PO04
NGC 4710	S0	sech+exp	3.2			DG96
NGC 4762	S0	sech+exp	4.6			DG96
5 galaxies	S0	–	1.8–4.6			DG97
NGC 6504	Sab	exp+exp	4.0		5.6	VD94
NGC 891	Sb	exp+exp	2.3–6.3			MO97
NGC 891	Sb	$R^{1/4}$+sech^2+exp	3.0			VA84
NGC 4565	Sb	sech^2+sech^2+halo	2.2	1.4		WU02
NGC 4565	Sb	sech^2+sech^2	4.6	1.4	4.1	SH89
NGC 4565	Sb	exp+exp	5.4	1.4	4.2	SH89
MW[b] (optical)	Sbc	exp+exp	3.0	1.3		LA03
MW[b] (NIR)	Sbc	exp+exp	3.3	1.3		OJ01
ESO 342-017	Scd	exp+exp	2.5	$\gtrsim$1.0	4.0-4.1	NE02
IC 5249	Sd	exp+exp	3.0	0.6		AB99

Notes: [a] reference YO06: (Yoachim and Dalcanton, 2006), DG96: (De Grijs and Van der Kruit, 1996), DG97: (De Grijs and Peletier, 1997), VD: (Van Dokkum et al., 1994), MO97: (Morrison et al., 1997), VA84: (Van der Kruit, 1984), WU02: (Wu et al., 2002), SH89: (Shaw and Gilmore, 1989), LA03: (Larsen and Humphreys, 2003), OJ01: (Ojha, 2001), NE02: (Neeser et al., 2002), AB99: (Abe et al., 1999). [b] Milky Way.

Abe et. al. (1999) used the same low-mass late-type galaxy (IC 5249) as we did, in the same band, using a 1D fit, so this provides a good comparison. However, we were unable to fit it in either a 2D or a 1D Two Disk fit. Abe et. al. (1999) however, use only 4 large radial bins for their fit and perform much larger conservative masking of stars than we did, which loss they correct by using large radial bins. Evenso, their f_z does not hint at the flat extended vertical structure we noticed. This difference could be caused by their conservative masking and by using large radial bins, something which we could do for a more extensive comparison. They find a f_h of 0.55, a value rather low and they are not hinting at the profound flatness we found (see Section 4.5). No thin and thick disk surface brightness is given so we cannot compare those. That they are able to fit this galaxy while we could not leaves the question of a possible thick disk component open for

debate. We did not study the effect of these large radial bins, so we cannot say much about their effect on the vertical profile. It is possible they lost the vertical structure we noticed even in the vertical profiles of the original image. It might also be that the asymmetric shape of the galaxy caused our Two Disk fit to fail, which Abe et. al. (1999) solved by using large bins. However, the asymmetry is not an issue for FGC 2339.

Yoachim & Dalcanton (2006) performed a 2D Two Disk fit, but used the $\mathrm{sech}^{n/2}$ functions for their fits and their results originated from R-band observations. While we fitted a large range of selected surface brightness profiles they fit the 2D Two Disk model on a cropped selection of the galaxy image without the use of any binning, fitting the model on each pixel of the image. This does mean that they keep a lower S/N ratio at higher scaleheights, while we try to increase the S/N in the outer parts by using growing bins to improve the quality of the fit, as this was necessary for us to be able to fit the vertical profiles. Another issue is their use of the Levenberg-Marquardt least-squares fitting which for us showed too many local minima and made it very difficult to determine what the global minimum is. However, they fitted in a completely different way, which makes it hard to compare, as we did not have galaxies from their sample. Yoachim & Dalcanton also show no vertical profiles to support the quality of their fit results, an important issue as we ourselves could find a succesful fit on NGC 1886, while there was no distinct thick disk component visible in the vertical profiles.

In our attempts to fit two late-type low-mass galaxies we clearly could distinct a vertical structure, but they did not resemble in any way the very small μ_{n-k} and f_z values that Yoachim & Dalcanton (2006) found. On the contrary. Our fits hint at a very flat vertical structure that hints of a long boxy structure like a ring or a large bar instead of a thick disk. They find 11 galaxies with a f_z equal or lower to 2, and 18 galaxies between 2 and 3. Only four of their sample galaxies give an f_z higher than 3. These values make it seem the thick disk is hard to distinguish from the thin disk. In their cases where the thick disk actually dominates the profile this structure should not be called a thick disk anymore if one considers the thick disk to be a faint extended component of the surface brightness profile. The small peak of the inner profile can be labelled to an inner disk or a young disk that is produced by enhanced star formation, with the outer part a more flatter or 'thicker' thin disk component.

The best way to understand the effect of the different fitting methods is to perform all those methods on a large sample and compare the results. However, we limited ourselves to the different models and used the method we considered to provide the most accurate results. We showed the 1D Two Disk fit results to be similar to the 2D Two Disk fit results where the 2D fit provided a higher accuracy although it is more sensitive to strong irregularities. The 1D fit requires sufficient good profiles fitted to acquire good average parameter values, but in contrast to the 2D fit shows insight to the intrinsic properties and the true radial variation of each profile.

6 Vertical colour profiles & gradients

Another way to gain insight in the structure of galaxies is by studying the stellar populations which build up galaxies and their variation within the galaxy. This can be done by analyzing the colours and colour gradients of galaxies. With our sample containing some galaxies observed in the J- and the K'-band, we are able to create $(J-K)$ colour profiles and study their properties and behaviour through the determination of the colour gradients.

We can study the properties and behaviour with stellar population synthesis models, which are tools for interpreting the integrated light (colors, line indices, and mass-to-light ratios) that we observe from galaxies. Ideally, we want to determine what mix of stars give rise to the observations, but as this is very complex, it is needed to make some assumptions about how the number of different types of stars are related. We will make use of the Single Stellar Population (SSP) models with a single age and a single metallicity. In these, all the stars are formed at the same time, with distribution in mass given by the chosen initial mass function (IMF), and with identical chemical composition. More advanced models take evolutionary processes into account, like enrichment of the interstellar medium, differential loss of various elements by galactic winds, and a time-dependent IMF. However, these processes are not well understood, and no consensus has yet been reached on these matters.

James et al. (2006), who performed a study on $(B-K)$ and $(J-K)$ colours on early-type galaxies, state that the integrated colour $(J-K)$ appears to be a good tracer of the initial metallicity of a SSP and is only weakly affected by age, whereas the integrated $(B-K)$, which we can compare to the $(B-I)$ results of De Grijs & Peletier (2000), who also determined vertical gradients on edge-on galaxies, is a good age indicator, mildly affected by the SSP metallicity. The J and K integrated fluxes are dominated by AGB stars when the SSP age is below $\sim$1 Gyr, and by upper red giant branch (RGB) objects for higher ages. This means that the integrated $(J-K)$ colour is mainly determined by the colour of AGB and/or RGB stars, whose evolution is strongly affected by their initial metallicity, whereas $(B-K)$ is sensitive to the magnitude and colour of the TO (turn off) stars, hence to the SSP age. However, for ages above $\sim$10 Gyr the $(B-K)$ colour tends to lose sensitivity to age. The age sensitive $(B-K)$ colours are very sensitive to the presence of young populations, whose main sequence stars are very bright in the B band.

The interpretation of broadband colour gradients relies on a careful mapping of the dust extinction within a galaxy (Knapen et. al. 1995, Huizinga 1998). No attempt was made to correct the surface brightness measurements for internal extinction, since no unique recipe is available to do this. We determine our gradients on the dustfree side of the galaxy and take the galactic extinction into account when determining our $(J-K)$ values.

In section 6.1 we will describe how colour profiles are created. Section 6.2 describes how we determined the vertical colour gradient of each galaxy. The results are shown in Section 6.3 and these will also be discussed there.

6.1 Creating colour profiles

To obtain colour profiles and determine the colour gradients we initially had 8 galaxies observed in two filters to create a $(J-K)$ profile. The image quality of NGC 2424 was too bad to match sufficient stars to match the two images for subtraction, while the J- and the K'-bands images of UGC 3186 were both simply too faint to obtain a coherent colour profile from which could be determined a gradient. Because of this these two galaxies were rejected.

Colour profiles can only be created when both galaxy images are exactly aligned and have the same pixel size. The K'-band images were matched to the J-band images using common forground stars. The seeing of both images was determined to decide which image would have to be convolved to the image with the higher seeing. This was usually the J-band image, although convolving was not always necessary. Because the J-band images show more and brighter stars as they have a higher resolution, these images was used to mask all the stars and from that create a mask image that could be used for the J- and the K'-band images. This to not be hindered by contamination

of the galaxy luminosity by forground star light. To both images and the mask image the rotation and centering of the J-band image was now applied.

Vertical colour profiles were created by subtracting vertical K'-band surface brightness profiles from binned vertical J-band surface brightness profiles. At the subtraction the masked areas were ignored and only those vertical data positions both images had a value for were used. For the combined error calculation a 1σ level of the variation in the sky background was used.

We extracted vertical surface brightness profiles at nine positions along the major axis of the sample galaxies, as we wanted to apply equal intervals that approximately corresponded to a factor of the typical scalelengths found with the two disk fits (20–25 arcseconds). The two profiles were binned as done before, the bins growing at an exponential factor b_f from the midplane, to retain an approximately constant overall S/N ratio in the resulting vertical profiles and decrease large irregularities. b_f was chosen to be 1.07, the minimal value that was also used for fitting the surface brightness profiles. No larger number was chosen as it would reduce the amount of datapoints.

To determine the radial positions we used scalelength factors of 0, 0.5, 1, 1.5 and 2, on both sides of the galaxy. We did not use the scalelengths from our 2D Two Disk fits as initial tests showed no radial behaviour of the profiles. Due to the small field of view of the UKIRT telescope it was not possible to go out much further radially so we had to limit ourselves to 2 scalelengths for the radial profiles. The radial width of the bin of each cut was larger than the previous to adjust for the lower S/N at larger radius. The radial binsize was set manually, the size a step of 2 pixels larger for each outer cut.

6.2 Determining colour gradients

To determine colour gradients certain selections had to be made to decide which part of the colour profile we would fit. De Grijs & Peletier (2000) state that the total acceptable range for a gradient fit produces – in general – the most representative vertical colour gradients as a function of projected galactocentric distance: Any small-scale variations arising from excess out-of-plane extinction, foreground starlight or artefacts from low S/N ratios in the outer regions are smoothed out by using a relatively large vertical range.

The profiles were plotted to determine on which side the dust lane is lying (see Appendix C). This could easily be determined by the red peak of the central profile on the bulge. This was done to use the side of the profile that is least contaminated by dust extinction for the gradient fit, as it would create a systematic higher gradient, while we want to recover a gradient for which external effects by dust are minimized. By eye it was determined at which height a clear steep rise of the profile started and this point was used as a minimum height for all colour profiles of the galaxy. As the minimum scaleheight for most galaxies was around 1 z_n, it was unnecessary to set a minimum depending on the scaleheight. We also wanted to be able to use as many datapoints possible.

The maximum height was determined by the ratio of z/z_n. This was set at 4.5 z_n. A initial limit was set at a $(J-K)$ error larger than 0.1 mag to prevent erratic datapoints (very high or low values) to be taken into account. This limit already made most datapoints fall within the 4.5 z_n limit, but this was not always sufficient as some remaining profiles still contained erratic datapoints. 4.5 z_n is a typical limit also used in literature to mark the range of a qualitative good profile.

The gradients of the profiles have to be matched to each other in case of radial variations so they contribute evenly to the determination of the central $(J-K)$ value. In the selected colour profiles we see no radial behaviour that would require a radial fit to correct the central $(J-K)$ value for each gradient. Without a radial behaviour the gradients are matched to each other by determining the average $(J-K)$ value of each cut at $z/z_n = 2$. The deviation of $(J-K)$ to the average $(J-K)$ at $z/z_n = 2$ was then determined for each profile. With the already determined gradient value for each cut the correct $(J-K)$ value at $z = 0$ could be calculated for each cut and from this value the average. Too sustain the final colour we then correct for the galactic extinction to $(J-K)$. This is a constant value, but different for each galaxy, that has to be subtracted from

the $(J-K)$ value.

To determine the gradient the Levenberg-Marquardt linear least-squares algorithm was made to the selected profile, weighting the datapoints to their errors. The results of the $(J-K)$ colour gradients are determined in mag arcmin^{-1} and in mag z_n^{-1}.

6.3 Results & discussion

Plots of the colour profiles for each of the six galaxies and their selected profiles for the gradient fit are shown in Appendix C, together with the single gradient fit results at their respective radii for each of the six galaxies in the tables A to F.

Two single stellar population models with different metallicity and initial mass functions are used to determine the properties of our colour profiles. The details are shown in table 18, which is adapted from the GALAXEV manual (2003), which can be downloaded from the GALAXEV website[6], and shows the metallicities of the SSP of the Bruzual & Charlot population synthesis models (Bruzual and Charlot, 2003). The models were computed using the Chabrier (2003) IMF with lower and upper mass cutoffs at $m_L = 0.1\ M_\odot$ and $m_U = 100\ M_\odot$ respectively. The SSP models are normalized to a total mass of 1 $M_\odot$ in stars at age $t = 0$.

For a better comparison of the results the Vazdekis population synthesis models[7] were used as well. The models were computed using the Unimodal Salpeter IMF with lower and upper mass cutoffs at $m_L = 0.01\ M_\odot$ and $m_U = 200\ M_\odot$ respectively, whereas the faintest star is 0.09 $M_\odot$. The Vazdekis models use a smaller range of metallicities but also smaller intermediate steps. For more details see Vazdekis et. al (1996).

TABLE 18

Metallicities of the Bruzual-Charlot SSP models

Key[a]	Z	X	Y	[Fe/H]
m22	0.0001	0.7696	0.2303	–2.2490
m32	0.0004	0.7686	0.2310	–1.6464
m42	0.004	0.7560	0.2400	–0.6392
m52	0.008	0.7420	0.2500	–0.3300
m62	0.02 ($Z_\odot$)	0.7000	0.2800	+0.0932
m72	0.05	0.5980	0.3520	+0.5595

Notes: [a] Padova 1994 evolutionary track; see Bruzual & Charlot (2003) for references. The key names the list for each set of metallicities. X, Y, Z are the fractional abundances of hydrogen, helium and everything else, respectively.

Table 19 shows in columns 2 and 3 the average gradients for the respective galaxies. The gradients are presented in mag arcmin^{-1} and mag z_n^{-1}. The average gradient $(z_n \Delta_{J-K})$ is –0.063 ± 0.027 mag z_n^{-1}. The $(J-K)$ in column 4 is not corrected for the galactic extinction. The average $(J-K)$ value, corrected for the galactic extinction, is 0.962 ± 0.066 magnitude.

To determine qualitative insight into the results of our gradient fits we applied them to the Bruzual-Charlot and Vazdekis models to derive what kind of stellar populations we find at different vertical heights and if our results are viable. To determine the tracks for the inner and outer vertical height a single stellar population with an age of minimal 15 Gyr was selected to cover the oldest stars in the galaxy. For those ages the resulting $(J-K)$ for the gradient position was compared to the metallicity tracks of the Bruzual & Charlot and the Vazdekis models.

Both models have their advantages and disadvantages. The Bruzual & Charlot models have a

[6] http://www.cida.ve/∼bruzual/bc2003

[7] http://www.iac.es/galeria/vazdekis/

larger range in metallicities and hence in $(J-K)$ values, while the smaller steps between metallicities in the Vazdekis models allow a more accurate determination of the metallicity, although this does not go up at extreme values.

TABLE 19

Colour Gradients

Galaxy	Δ_{J-K} [Mag arcmin^{-1}]	$z_n\Delta_{J-K}$ [Mag z_n^{-1}]	$J-K$ [Mag]	$E(J-K)$ [Mag]	$z_n\Delta^{BC}_{B-I}$ [Mag z_n^{-1}]	$z_n\Delta^{V}_{B-I}$ [Mag z_n^{-1}]
(1)	(2)	(3)	(4)	(5)	(6)	(7)
IC 2531	-0.937 ± 0.533	-0.070 ± 0.040	1.057 ± 0.080	0.044	-0.163	-0.120
IC 3322A	-1.384 ± 1.392	-0.082 ± 0.082	0.871 ± 0.164	0.010	-0.130	-0.106
NGC 0973	-0.039 ± 0.547	-0.003 ± 0.041	0.973 ± 0.082	0.053	-0.040	-0.014
NGC 1886	-0.621 ± 0.719	-0.028 ± 0.032	0.986 ± 0.064	0.013	-0.142	-0.070
NGC 5290	-1.326 ± 0.491	-0.093 ± 0.034	0.960 ± 0.069	0.003	-0.264	-0.222
UGC 4277	-1.808 ± 0.995	-0.076 ± 0.042	1.081 ± 0.084	0.033	-0.163	-0.120

Notes: (1) Galaxy. (2) $(J-K)$ gradient. (3) $(J-K)$ gradient over units of scaleheight. (4) Observed average $(J-K)$ values at $z=0$ after matching the gradients to their $z/z_n=2$ position. (5) Galactic extinction[8]. (6) $(J-K)$ to $(B-I)$ gradient conversion according to the Bruzual-Charlot models. (7) $(J-K)$ to $(B-I)$ gradient conversion according to the Vazdekis models.

Table 20 shows the different metallicities according to the average gradients for each galaxy taking $z/z_n=0$ and $z/z_n=4$ for the inner and outer vertical heights, as most selected profiles are not able to reach much further out, to determine their population properties. For this the $(J-K)$ gradient difference from the two positions was subtracted from the average $(J-K)$ of the fit, which value is equal to the central value at $z/z_n=0$. The median abundance gradient is –0.049 ± 0.18 $Z\ z_n^{-1}$. The median is taken as IC 3322A gives a value of –0.006 and NGC 0973 –0.028, while the other values are equal at 0.049. Their low values originate from a low overall $(J-K)$ and a rather flat gradient, respectively.

All galaxies show high metallicities in the mid plane while IC 2531 and UGC 4277 show values above the model possibility. This unusual high value can be contributed to reddening by dust extinction as both galaxies possess prominent dustlanes and are about perfectly edge-on. Thus the correct gradients for IC 2531 and UGC 4277 are probably smaller. As the high metallicity for the inner part is expected and the $(J-K)$ values remain within model values, the influence of dust is probably small in our fit. The outer parts show in all cases lower metallicities.

TABLE 20

Metallicities for 15 Gyr Stars on $J-K$ Gradients

A: Bruzual-Charlot Models

Galaxy	Z (0 z_n)		Z (4 z_n)
IC 2531	0.05<	⇒	0.004
IC 3322A	0.008–0.004	⇒	0.0001>
NGC 0973	0.05–0.02	⇒	0.05–0.008
NGC 1886	0.05	⇒	0.008–0.004
NGC 5290	0.05	⇒	0.0004–0.0001
UGC 4277	0.05<	⇒	0.004

B: Vazdekis Models

Galaxy	Z (0 z_n)		Z (4 z_n)
IC 2531	0.03<	⇒	0.004
IC 3322A	0.03<	⇒	0.0004>
NGC 0973	0.019–0.030	⇒	0.019
NGC 1886	0.03<	⇒	0.008
NGC 5290	0.03<	⇒	0.0004
UGC 4277	0.03<	⇒	0.004

Notes: Fractional abundances of non-hydrogen and -helium metals at $z=0$ and at 4 scaleheights. $<$ or $>$ mean the found values are larger or smaller than provided by the models.

As we found that $(J-K)$ gives insight in the metallicity of the stellar population, the models also allow us to see if we can gain insight in the age of the stellar population over vertical height. We did this by determining the stellar population ages of stars with a solar metallicity (m62) and

with a minimal age of 1 Gyr. We expected not to be able to get results and this was also the case. Thus we can confirm that $(J-K)$ colour profiles are a good indicator for change in the metallicity of stellar populations, but weak on changes in the stellar population ages, as James et. al (2006) state.

To be able to compare our results with those from De Grijs & Peletier (2000), we converted each average $(J-K)$ gradient to a $(B-I)$ gradient. This was done by selecting the same age for the model (15 Gyr) and matching it with the metallicity models that we had found for the $(J-K)$ values, to determine the $(B-I)$ values for these metallicities. From this a $z_n\Delta_{B-I}$ gradient could be determined. The median $(B-I)$ colour at $z=0$ is 2.56 ± 0.23 magnitude for the Bruzual-Chabrier models and 2.41 ± 0.19 magnitude for the Vazdekis models. The resulting gradients are shown in Table 19. The average $(B-I)$ gradient is -0.150 ± 0.072 mag z_n^{-1} for the Bruzual-Charlot models and -0.109 ± 0.069 mag z_n^{-1} for the Vazdekis models. The slightly lower Vazdekis values are caused by its lower extremes for possible high or low $(J-K)$ and $(B-I)$ values, which automatically leads to smaller gradients. Thus we consider the Bruzual-Charlot models to be better in our case as our values remain better within their extremes than the Vazdekis models.

We find that our gradient is not only blueing but also much larger than the De Grijs & Peletier (2000) result of 0.03 or their alternative gradient of 0.06 from a model with a different star formation rate. On average, the earlier-type galaxies of De Grijs & Peletier (2000), exhibit smaller vertical $(B-I)$ gradients than the later types, but their $(B-I)$ gradients are not as large as our $(B-I)$ gradients, showing their gradients are influenced by star formation close to the plane. Evenso, the observation of a blueing of the galactic disk with height above the plane cannot always rule out the possibility that this is due to extinction effects while the center part is reddened by dust. However, since almost all of our profiles show a blueing trend in the gradient of which some are quite strong, they cannot all be simply explained by these effects, as our inner part values remain within model values and can be assigned to a higher metallicity.

A comparison with Dalcanton & Bernstein (2002) is more difficult, as they do not provide colour gradients for their $(R-K)$ profiles. Our sample galaxies are also all high-mass galaxies, so we cannot say anything about their low-mass results. They assign their reddening in the inner part of the colour profiles of their high-mass galaxies to dust. In our case, as we have taken the side where there is no dustlane and went further out for the gradient fit to avoid its effects, we cannot say the same thing. As the central $(J-K)$ values remain within model values for stars with high metallicity in the inner part and low metallicity in the outer part this means that dust is probably not dominating the reddening in our inner part.

7 Conclusions

We performed data reduction and photometric calibration on a pilot sample of 11 late-type disk galaxies, observed in the near-infrared J- and or K'-filter, creating images with high S/N and very flat backgrounds. Various kinds of structure decomposition was done on vertical surface brightness profiles to discover if the galaxies contained thick disks or not and what their parameters would be.

We create vertical colour profile sets for six galaxies available in the J- and K'-band to determine their colour gradients and hence insight in their stellar population.

Our 2D two disk (thin+thick) fits confirm the results of Yoachim & Dalcanton (2006) as we find clear thick disk components in all our sample galaxies except for one case, where the possible existence of a thick disk cannot be excluded. However, our results show clear differences. We only find thick disk components in our high-mass galaxies ($v_{rot} > 120$ km s^{-1}). For two low-mass galaxies added to our sample, which were observed in the R-band, we confirm a distinct vertical structure but those could not be fitted as a superposition of thin+thick disk. Our thick disk parameter values show also fainter and flatter thick disks than their high-mass galaxies, with an average difference between μ_n and μ_k (the central surface brightness for the thin and thick disk) of 4.5 ± 0.7 mag arcsec^{-2} and an average scaleheight ratio of 5.6 ± 1.8. Tests of our fitting methods on artificial galaxies showed that truncated galaxies, a commonly observed phenomenon, will show various deviations from the input parameters, making it difficult to assess the quality of the individual results.

Our $(J-K)$ colour gradients show distinct blueing at larger distance from the plane. This is in contrast to the $(B-I)$ results of De Grijs & Peletier (2000) who find no clear gradient and even a slight reddening at larger scaleheight. Their result is probably affected by star formation near the plane. Our results stay within the Bruzual-Charlot models, showing dust has little influence even close to the galactic plane on our colour profiles. This in contrast to the $(R-K)$ results by Dalcanton & Bernstein (2002) who address their inner reddening to dust influence.

Acknowledgements

First of all I would like to thank Michael Pohlen for his help, suggestions, advise and insightful discussions. I would like to thank Reynier Peletier for providing me with this fascinating research project and giving useful advise and help. I would also like to thank Richard de Grijs for his useful comments on colours and colour gradients and providing us with his observation logs. And last but not least, I would like to thank my fellow students from the old Coma Cluster: Hugo Buddelmeijer, Johan Hidding, Arjen Siegers and Matthijs van der Wiel, for their help, advise, support and making sure I took time to relax during my project.

APPENDIX

A Galaxy Atlas

For each galaxy image five images/plots are shown. In the upper left corner, if available, a colour image of the galaxy is shown, taken from the Sloan Digital Sky Survey[9].

In the upper right corner (or center) a contour map of the respective galaxy is shown. The contour lines are set in equidistant intervals of 0.5 magnitude with the value of the outermost isophote, $\mu_{\rm lim}$, given in the upper right corner. The contour maps of FGC 2339, IC 5249 and NGC 4179 originate from Pohlen (2000) and Pohlen et al. (2004).

In the second row a set of vertical profiles next to a set of radial profiles of the complete galaxy are shown. For each profile three cuts are selected. Errorbars are not shown to keep the quality of the plot. The horizontal cyan line represents $\mu_{\rm crit}$ (see Section 2.4.2 and Table 8), i.e. the surface brightness up to where we trust the profile.

On the last row a four window set of plots of vertical profiles are shown of the selected fit datapoints with their errors (black dots), the model fit (red line), the thin disk component to the fit (magenta line), the thick disk component to the fit (green line) and the single disk fit (blue line). The profiles have been chosen on their quality to clearly show thick disk component if present. For FGC 2339 and IC 5249, for which no two disk fit could be made, only the single disk fit is shown. For the galaxies not used for the fit no plots are shown.

[9] http://www.sdss.org/

FGC 2339 R

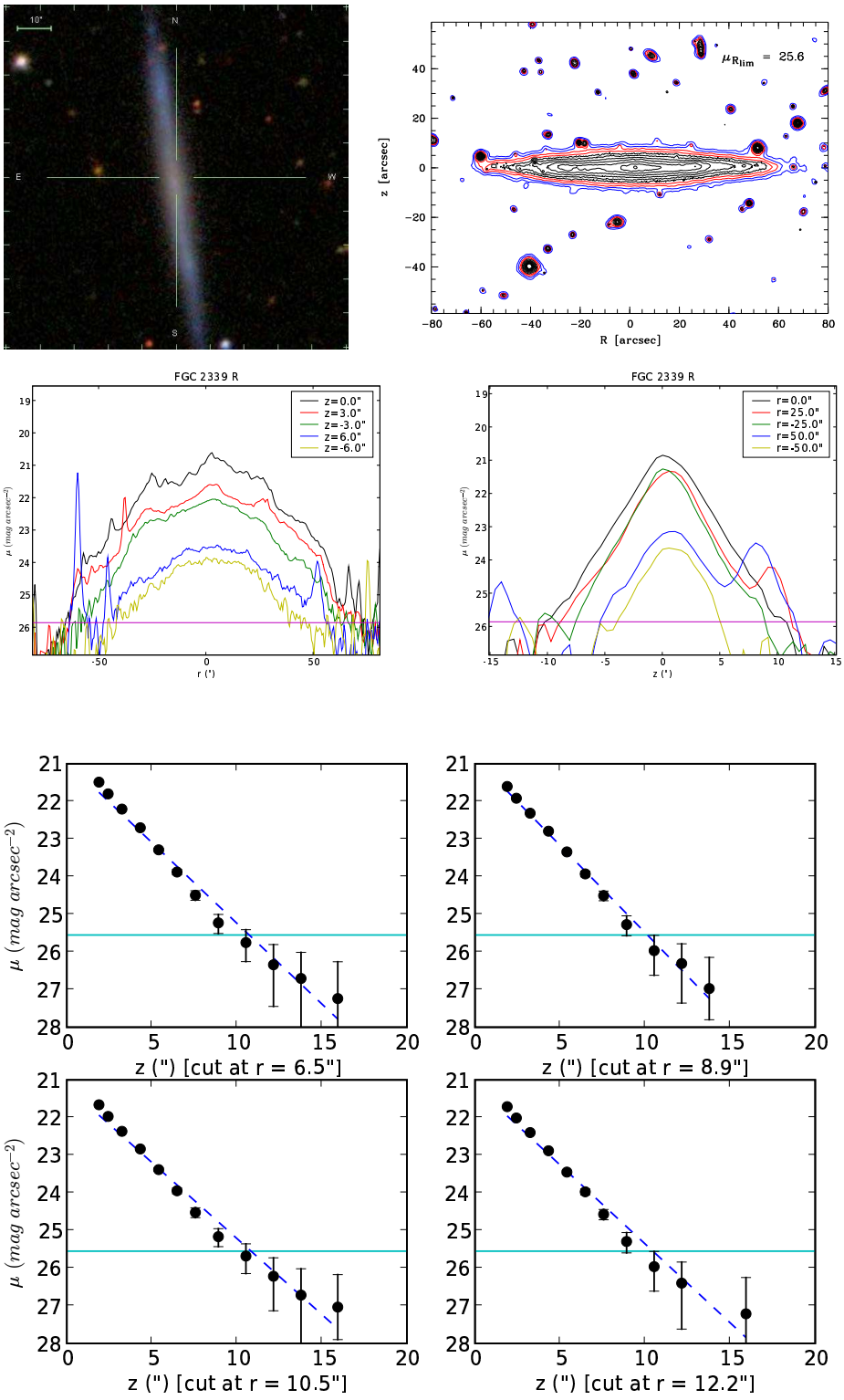

Figure 10: FGC 2339 R

IC 2531 J

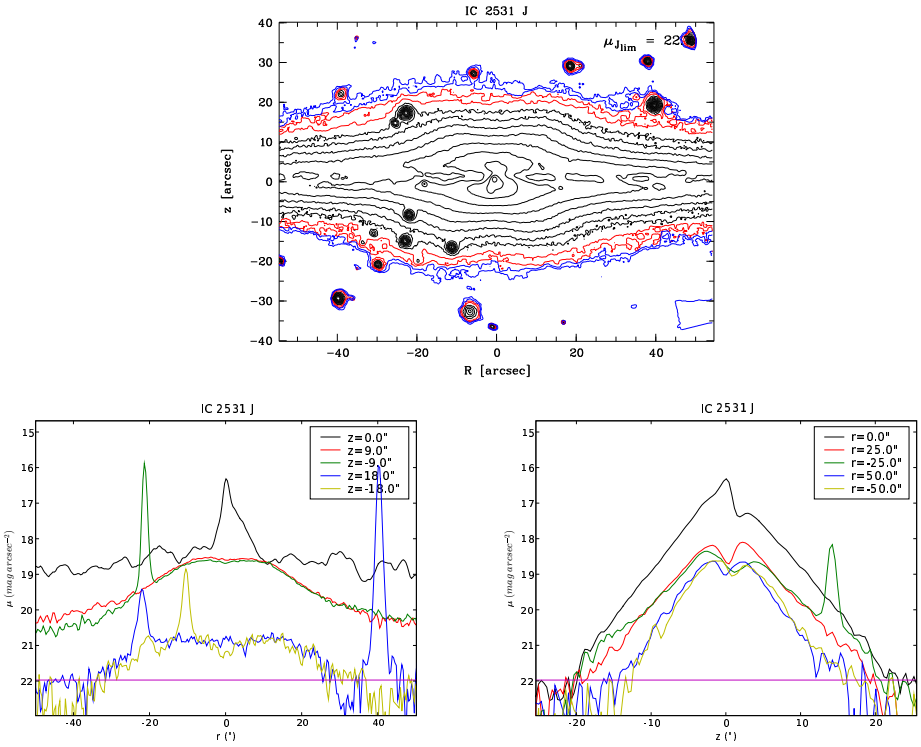

Figure 11: IC 2531 J

IC 2531 K

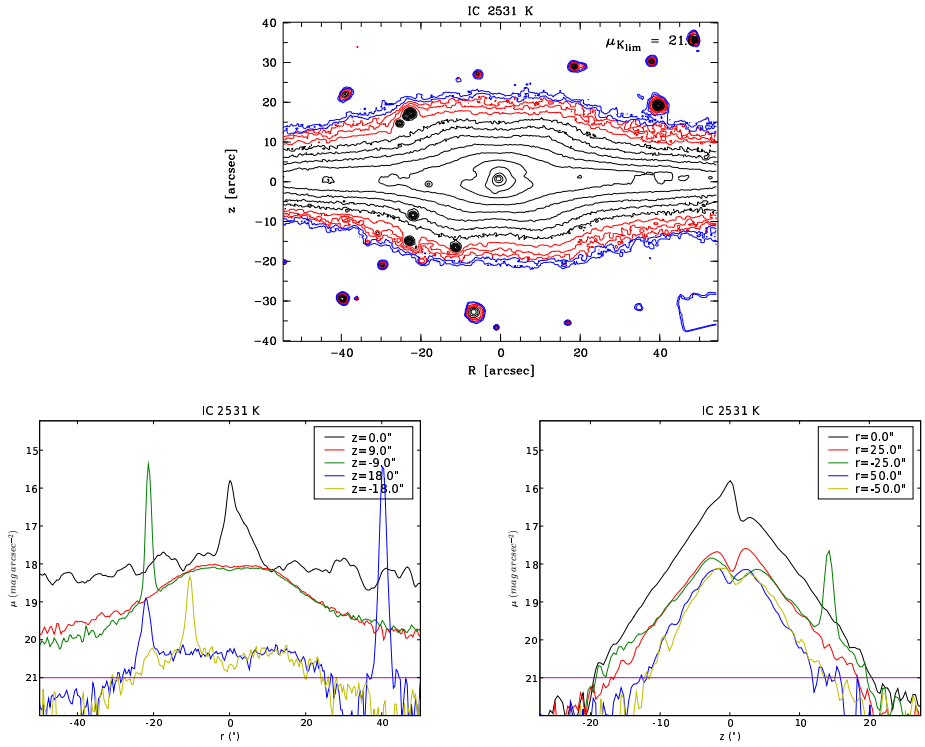

Figure 12: IC 2531 K

IC 3322A J

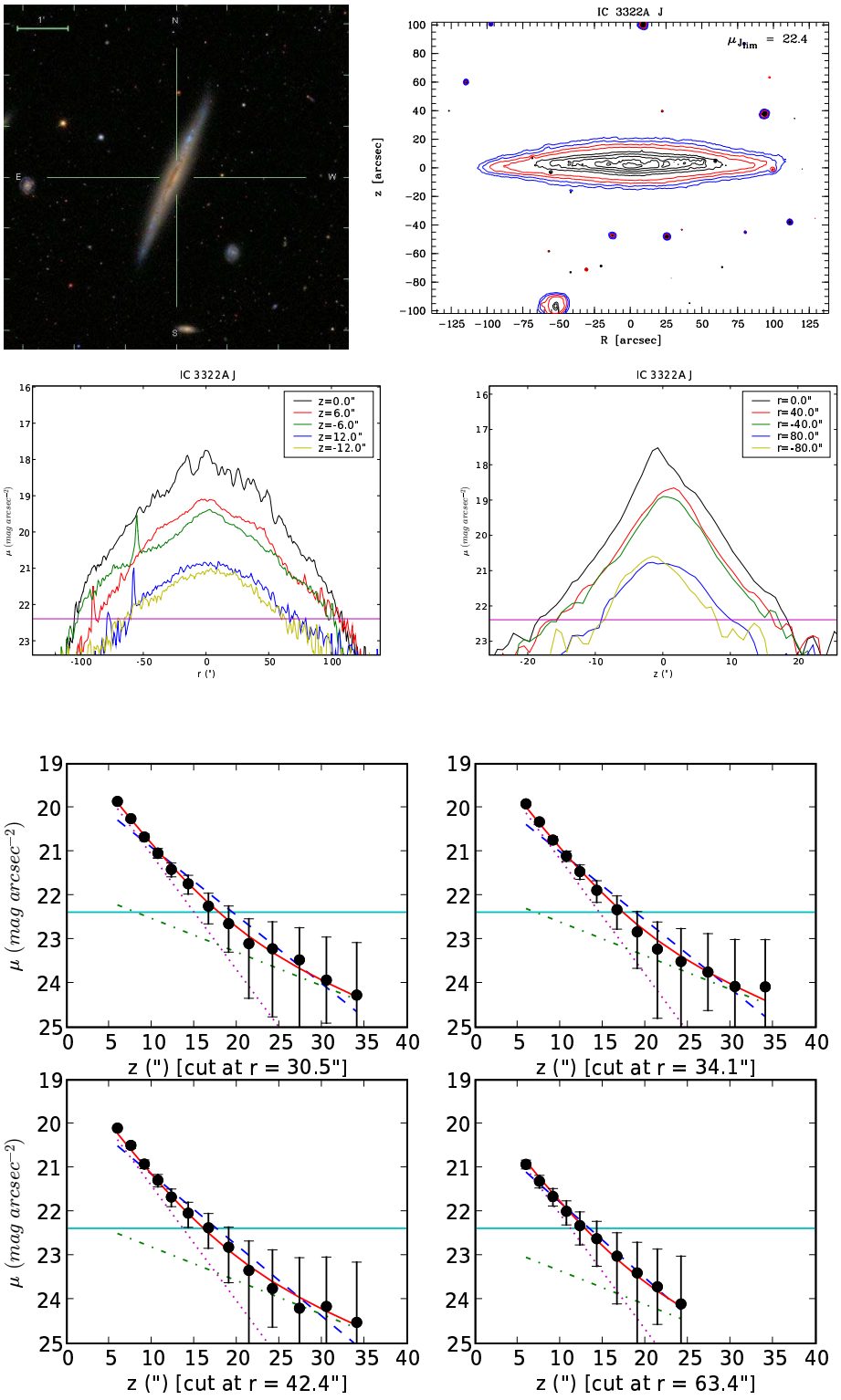

Figure 13: IC 3322A J

IC 3322A K

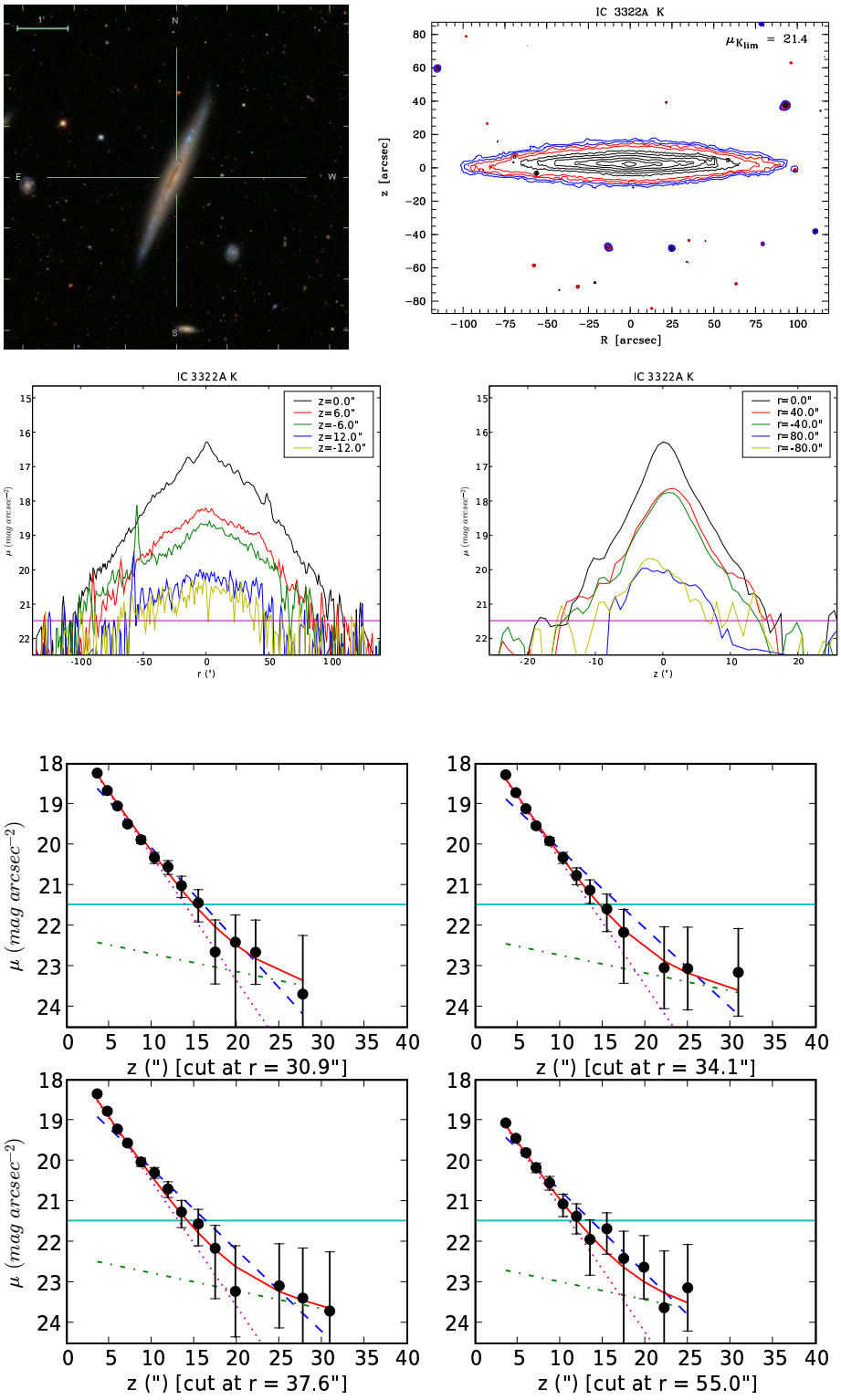

Figure 14: IC 3322A K

IC 5249 R

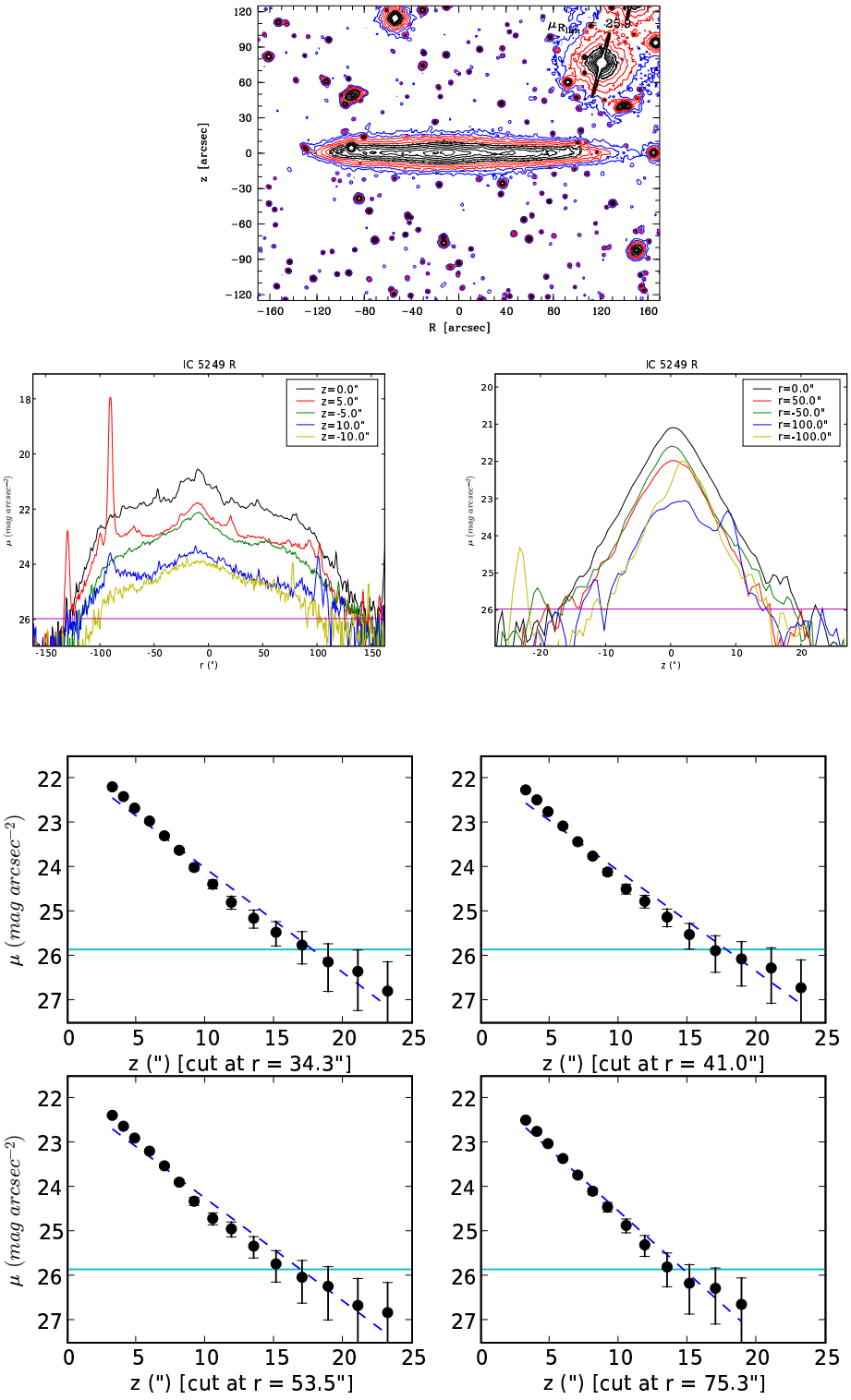

Figure 15: IC 5249 R

NGC 0973 J

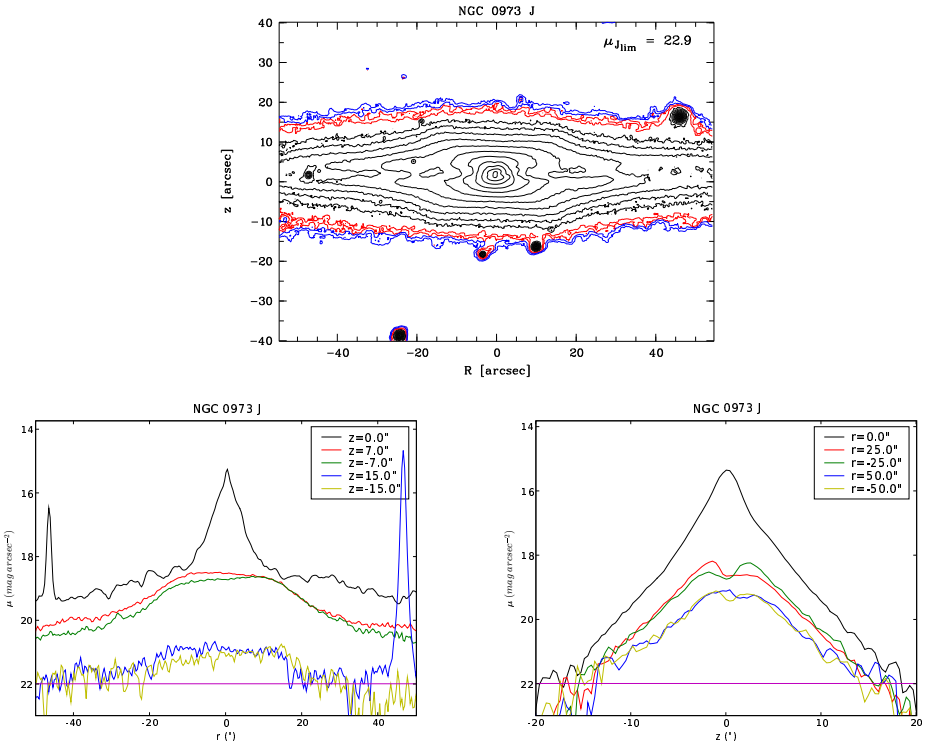

Figure 16: NGC 0973 J

NGC 0973 K

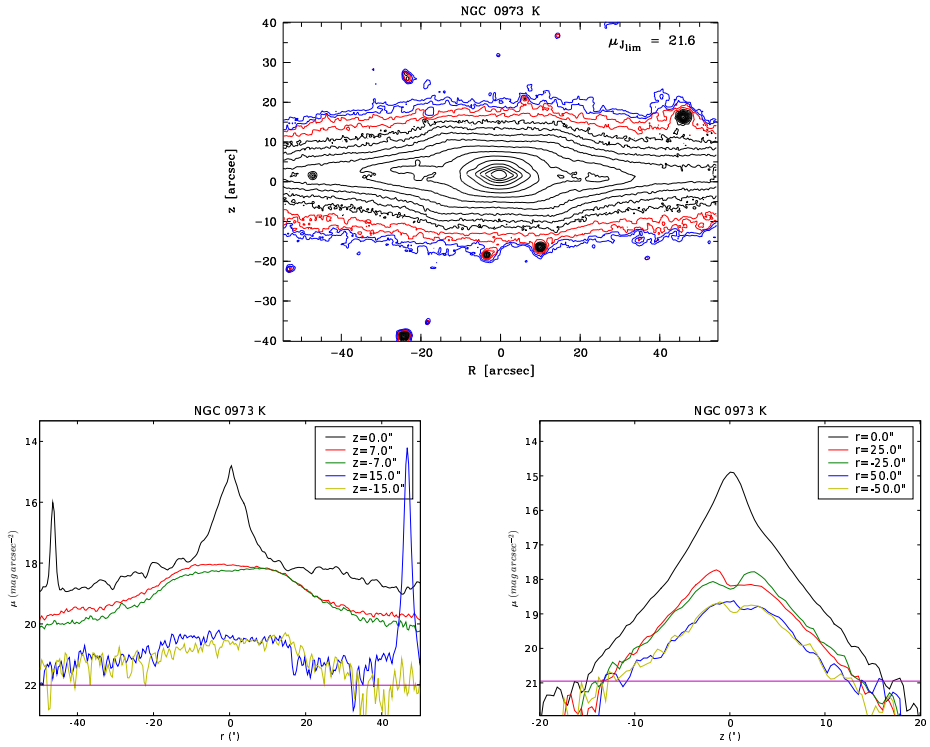

Figure 17: NGC 0973 K

NGC 1886 J

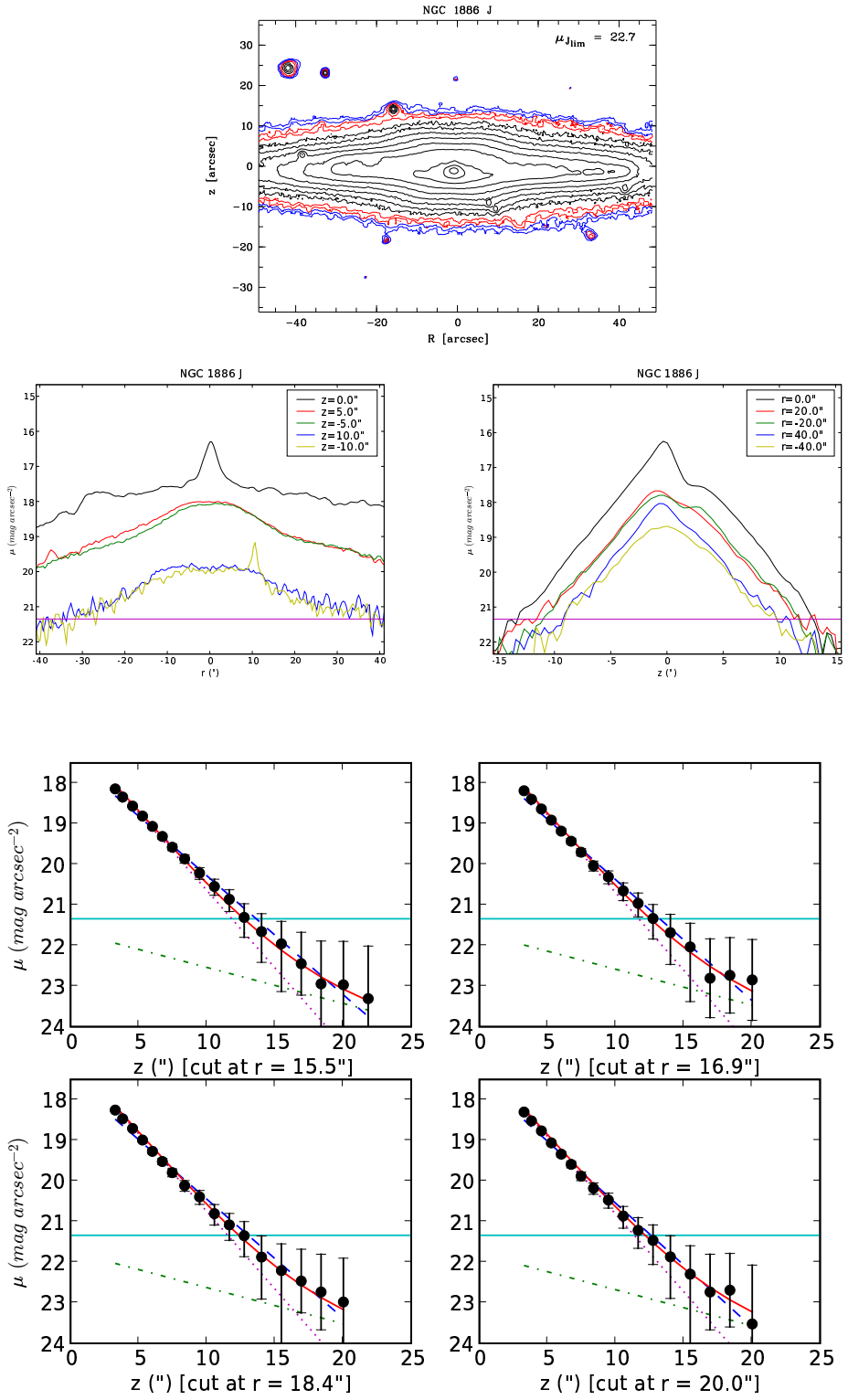

Figure 18: NGC 1886 J

NGC 1886 K

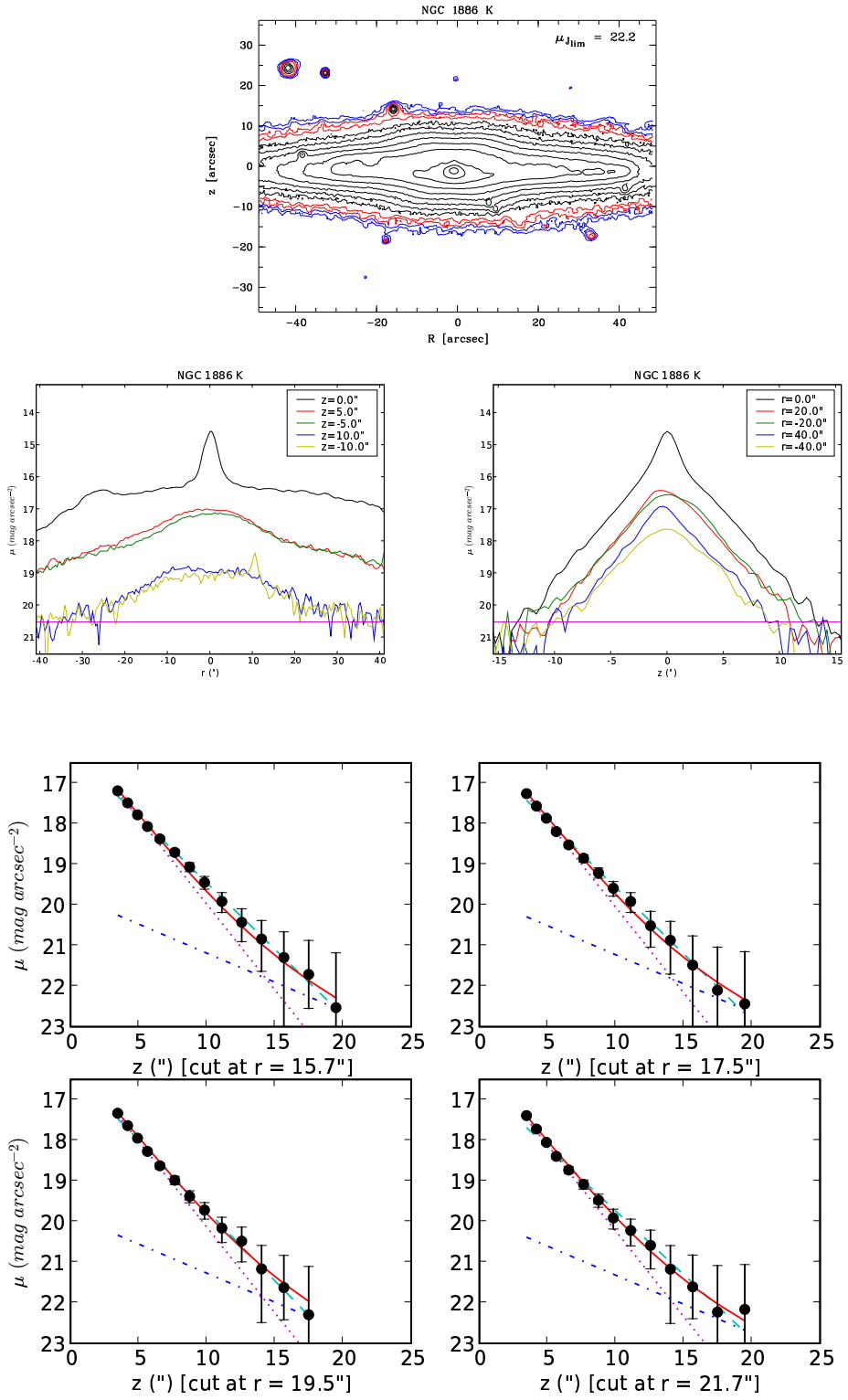

Figure 19: NGC 1886 K

NGC 2424 J (CA)

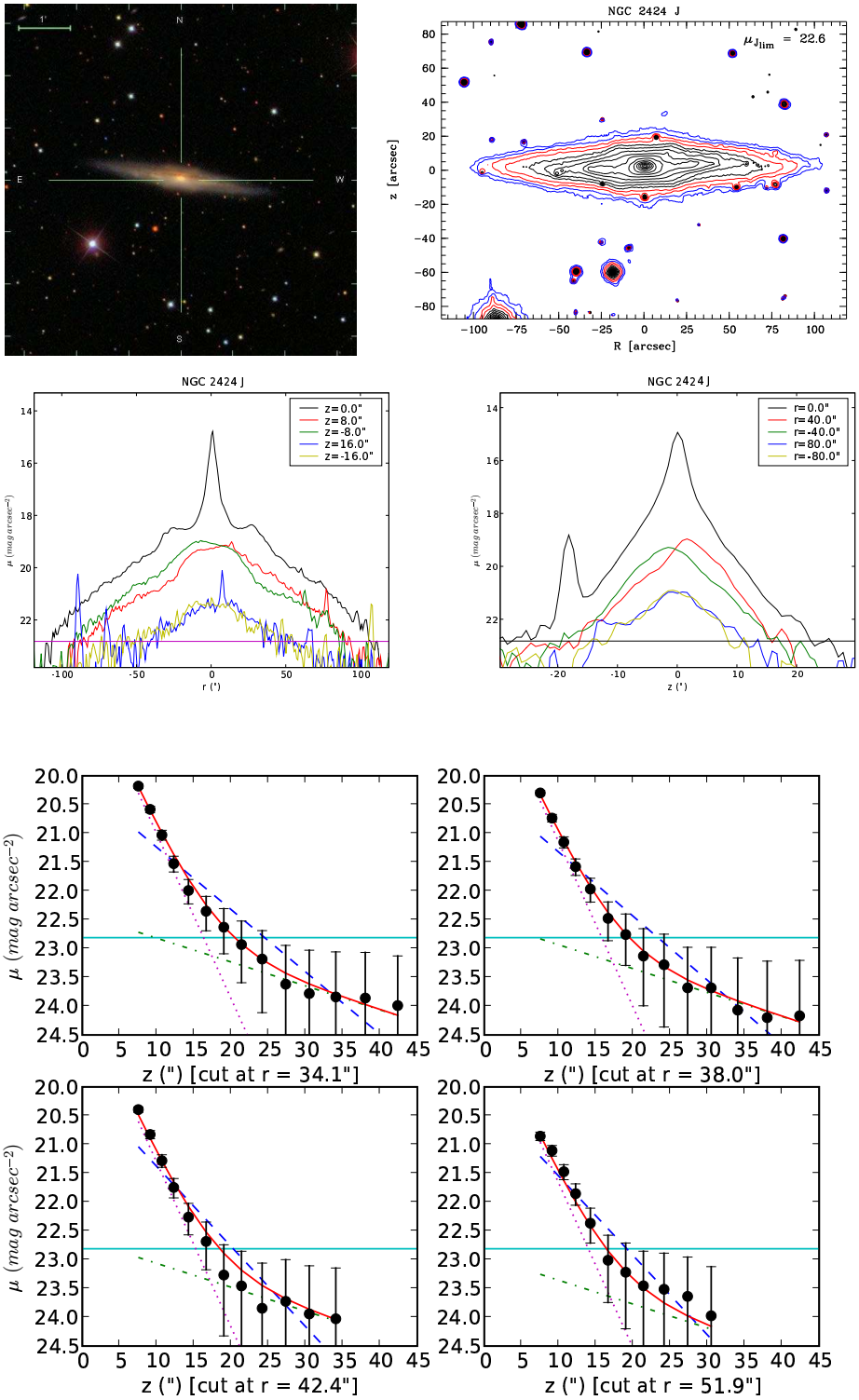

Figure 20: NGC 2424 J (CA)

NGC 2424 J (UKIRT)

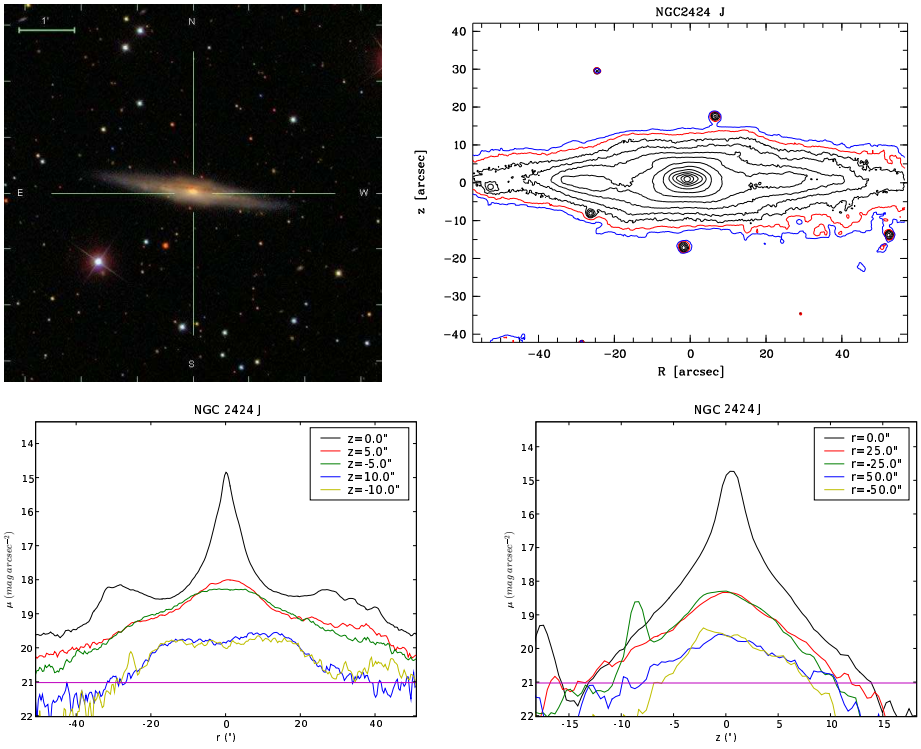

Figure 21: NGC 2424 J (UKIRT)

NGC 2424 K (UKIRT)

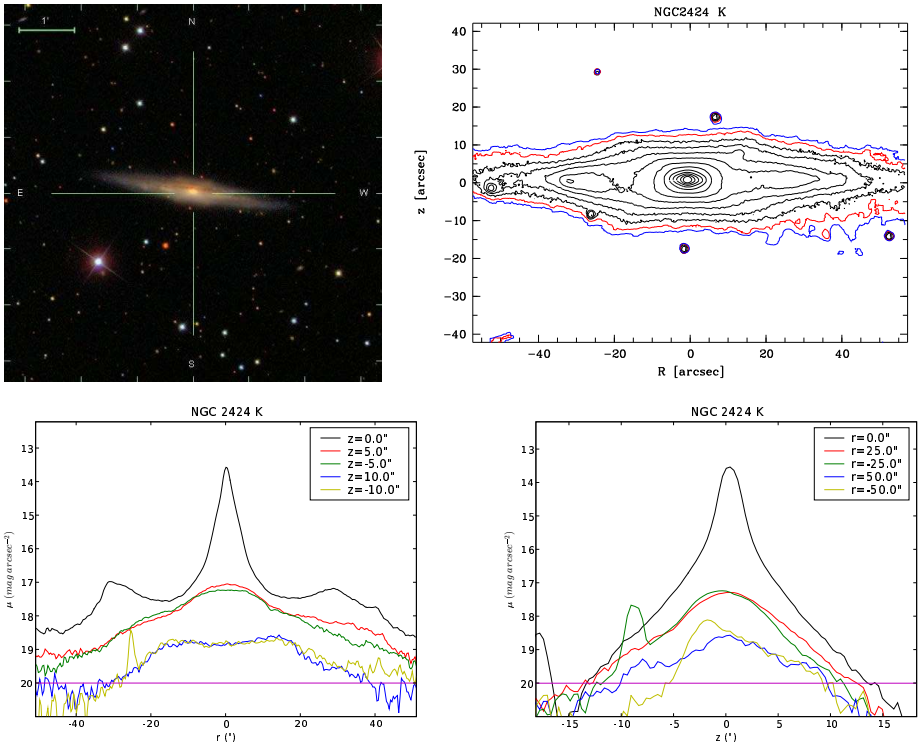

Figure 22: NGC 2424 K (UKIRT)

NGC 2591 K

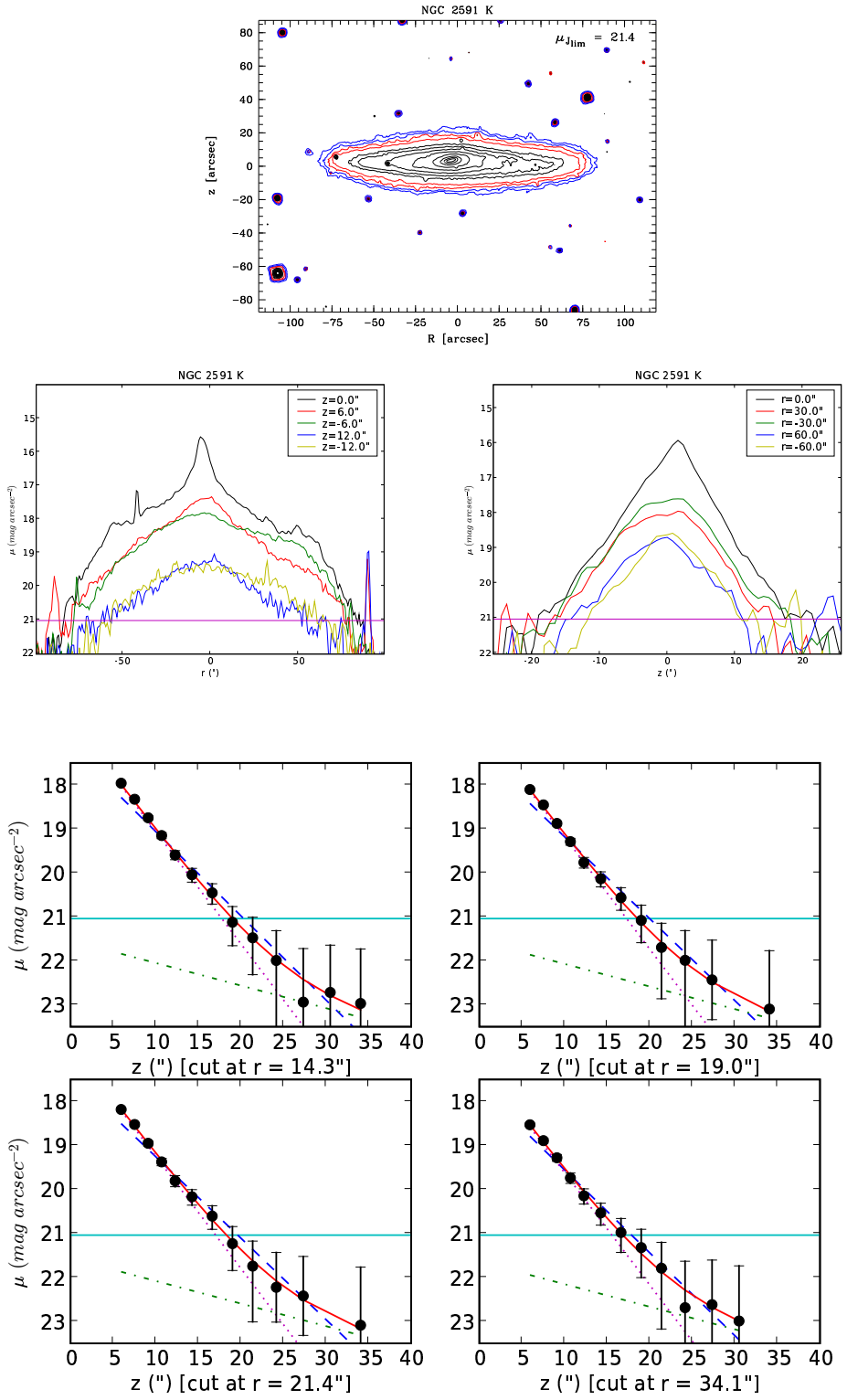

Figure 23: NGC 2591 K

NGC 4179 V

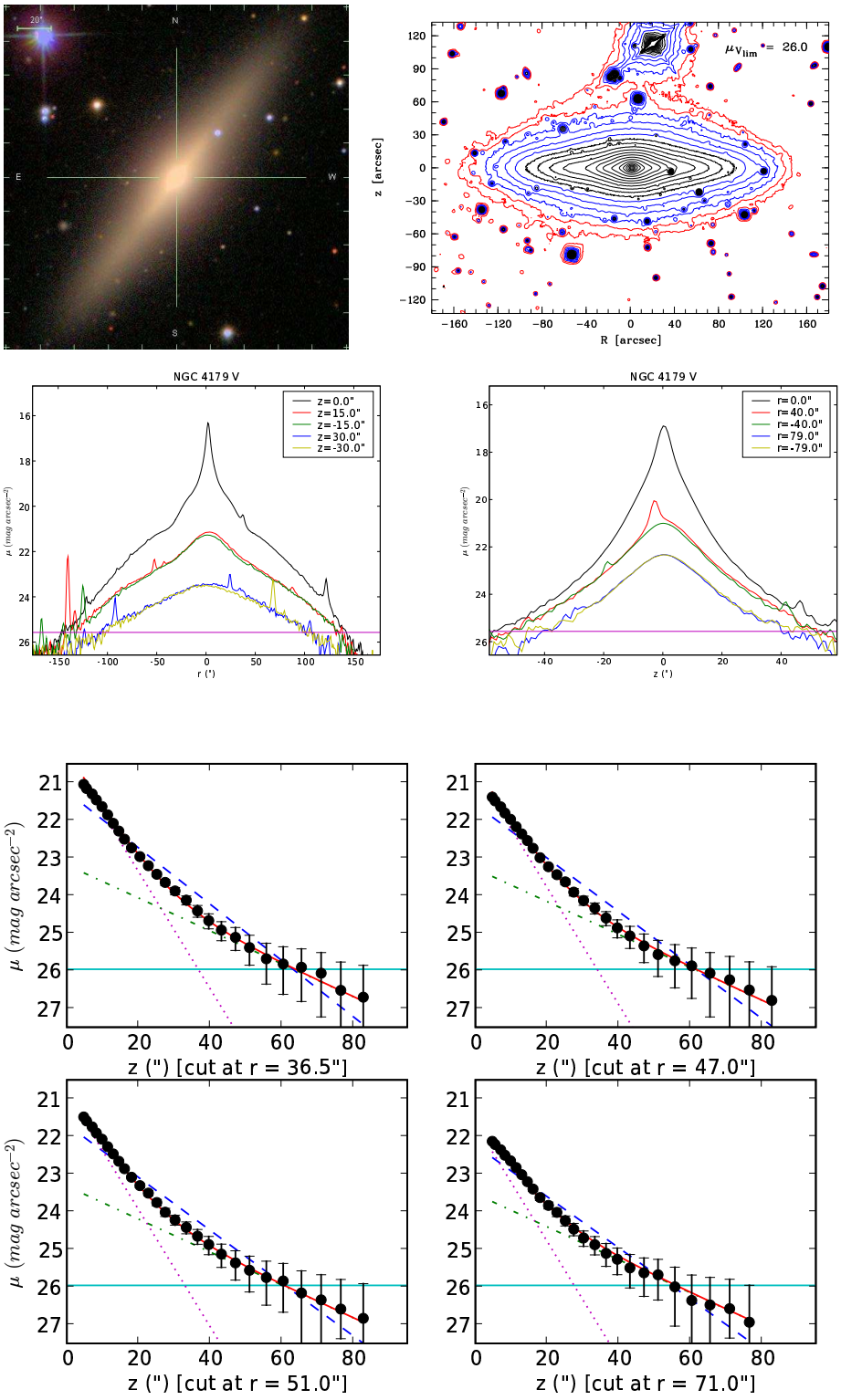

Figure 24: NGC 4179 V

NGC 5290 J

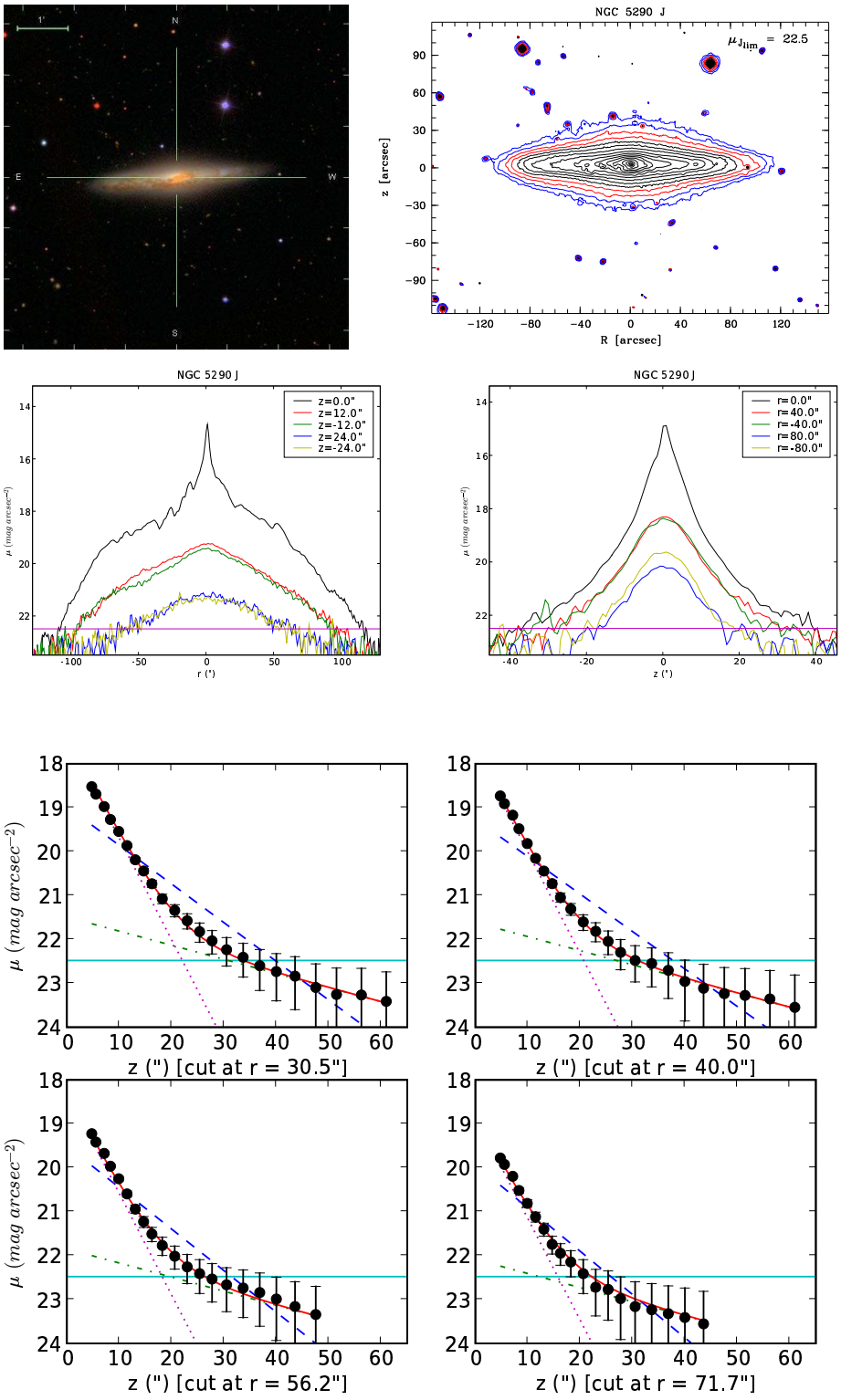

Figure 25: NGC 5290 J

NGC 5290 K

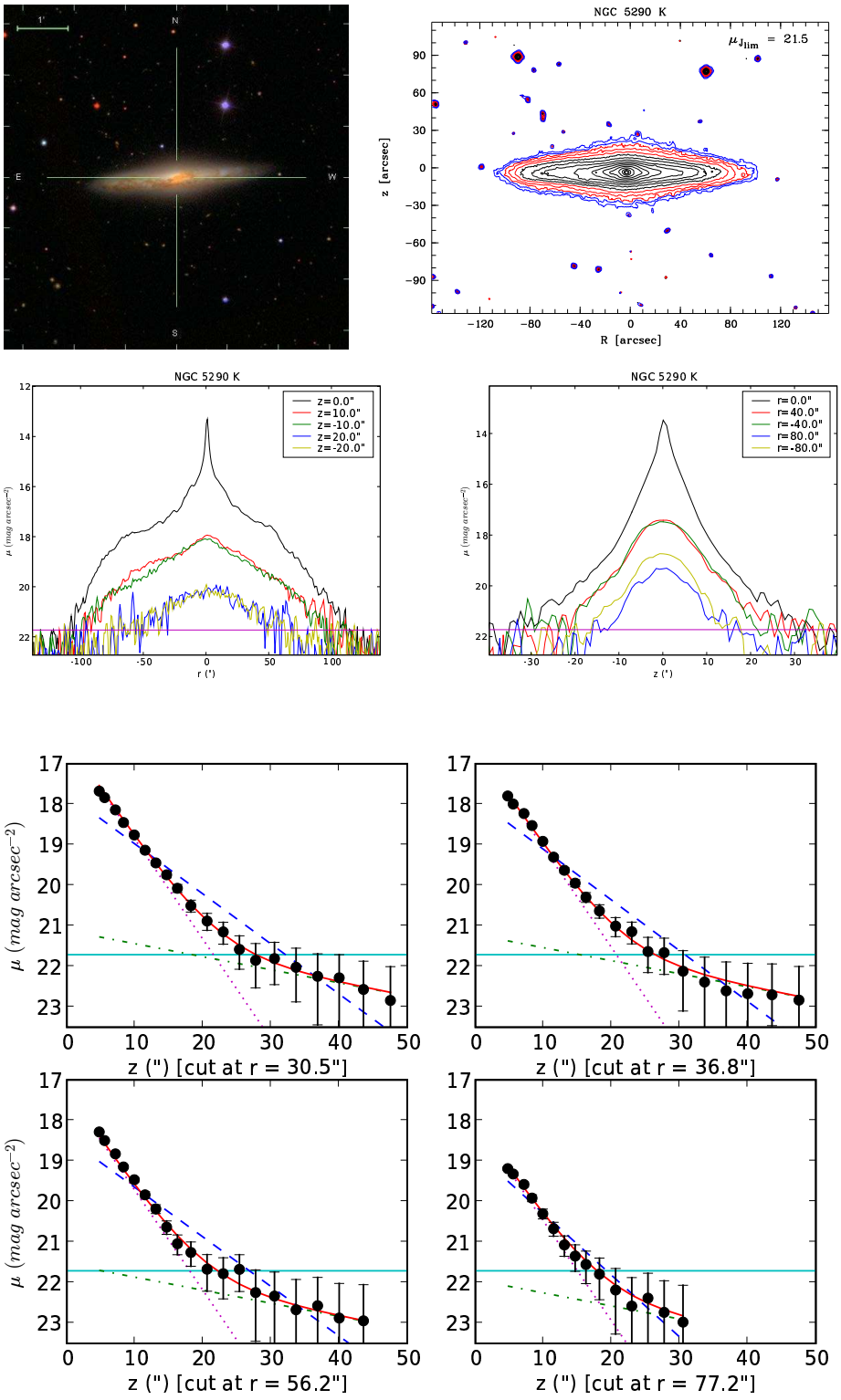

Figure 26: NGC 5290 K

NGC 5348 J

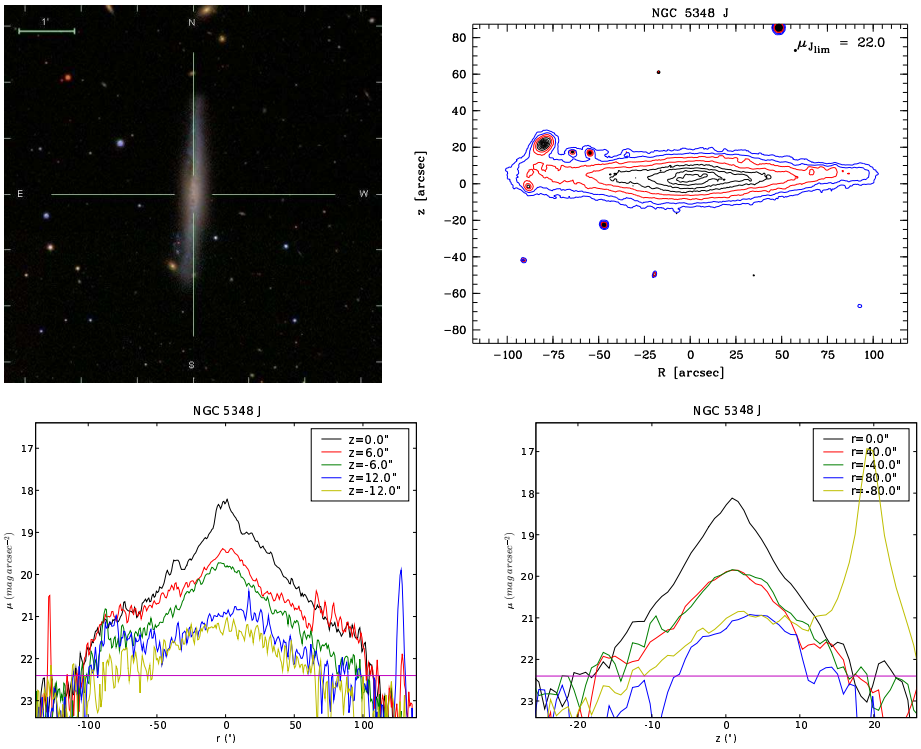

Figure 27: NGC 5348 J

NGC 5981 J

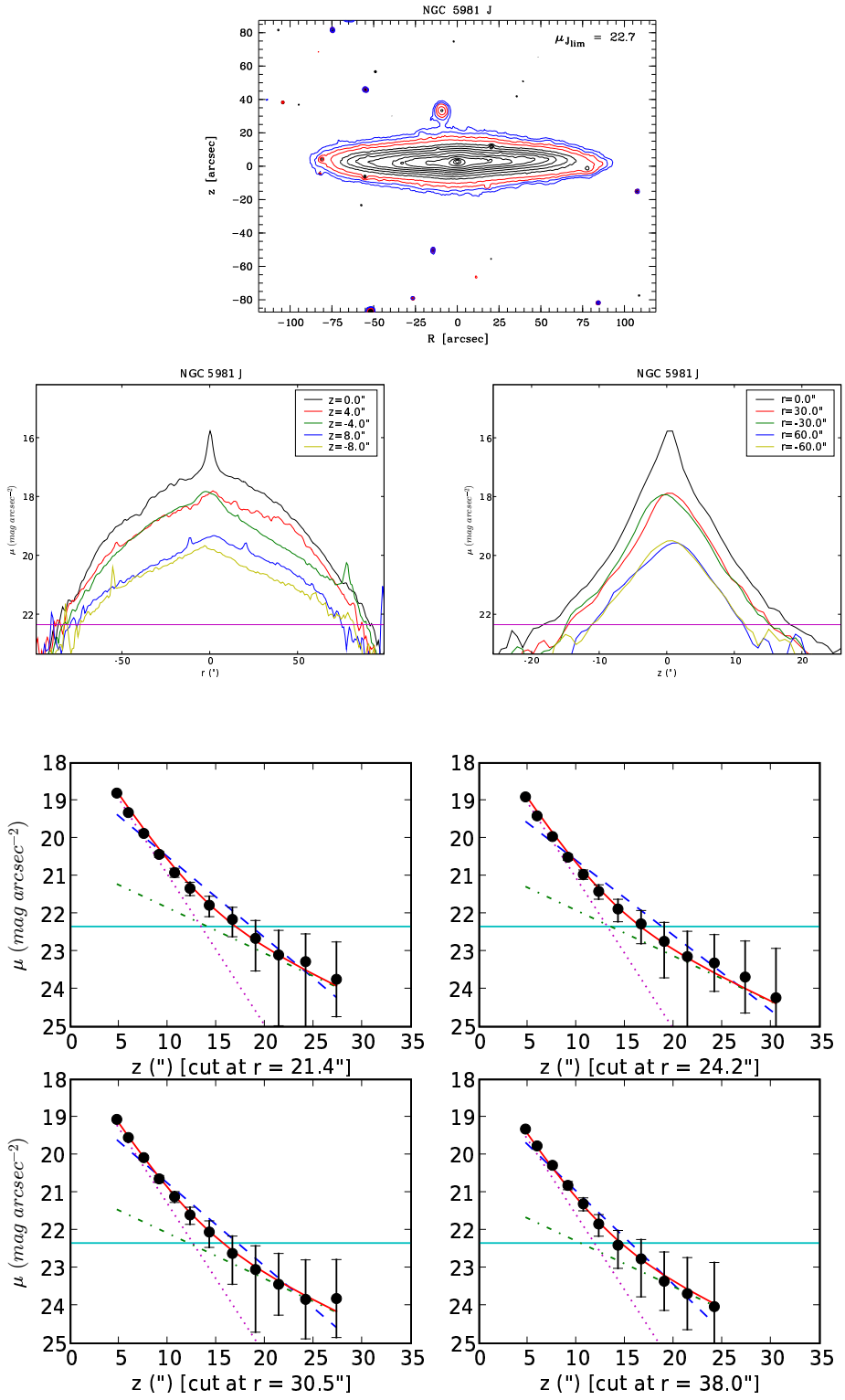

Figure 28: NGC 5981 J

UGC 3186 J

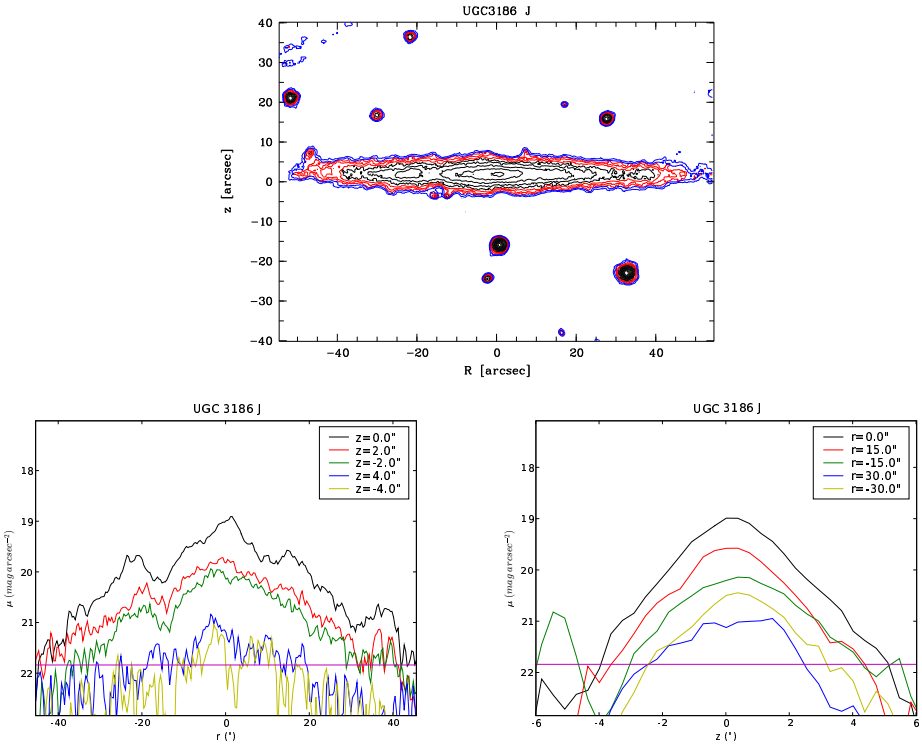

Figure 29: UGC 3186 J

UGC 3186 K

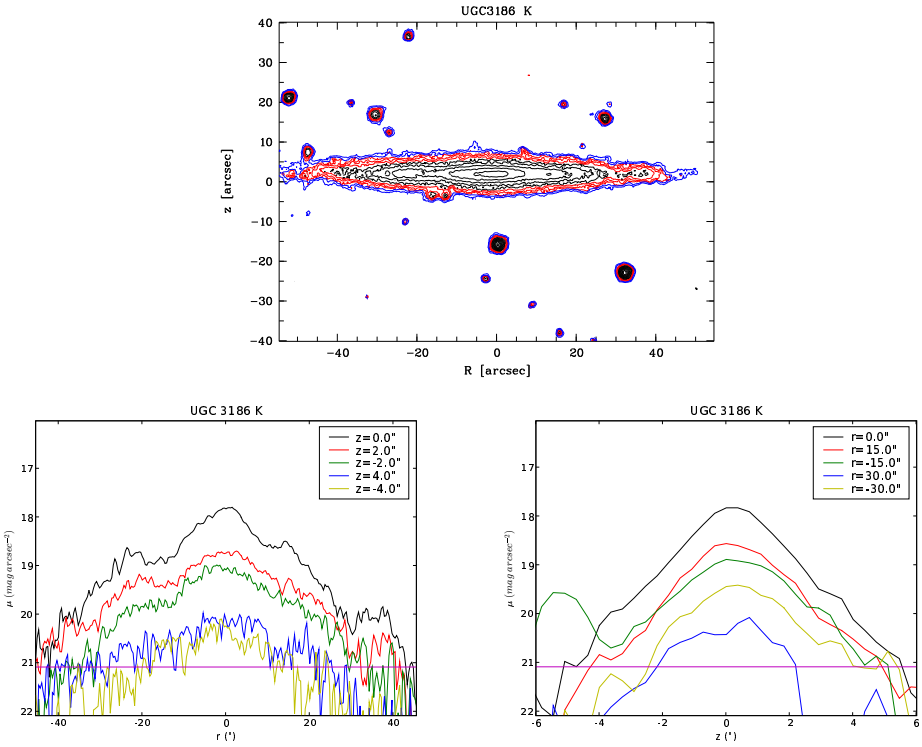

Figure 30: UGC 3186 K

UGC 4277 J

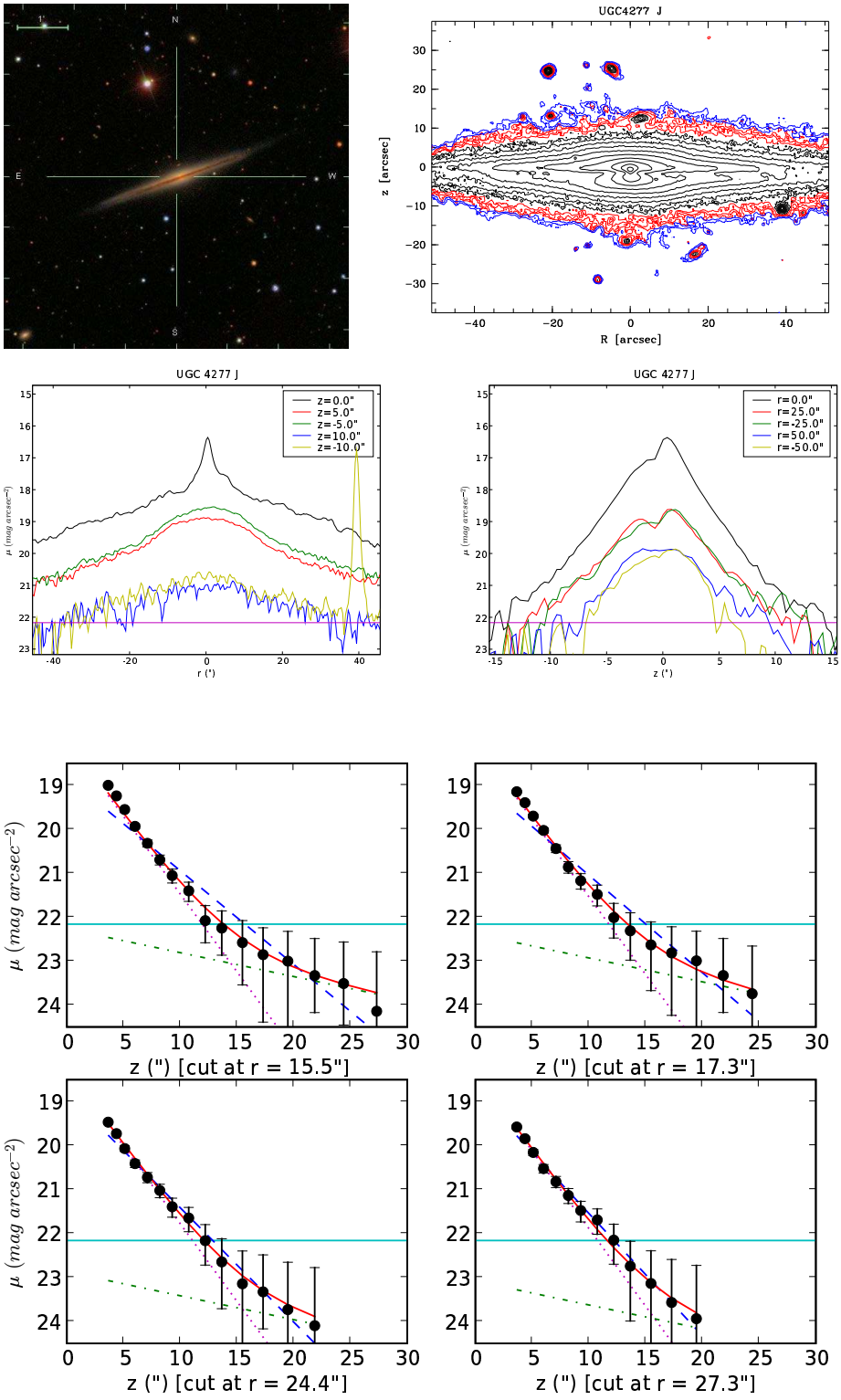

Figure 31: UGC 4277 J

UGC 4277 K

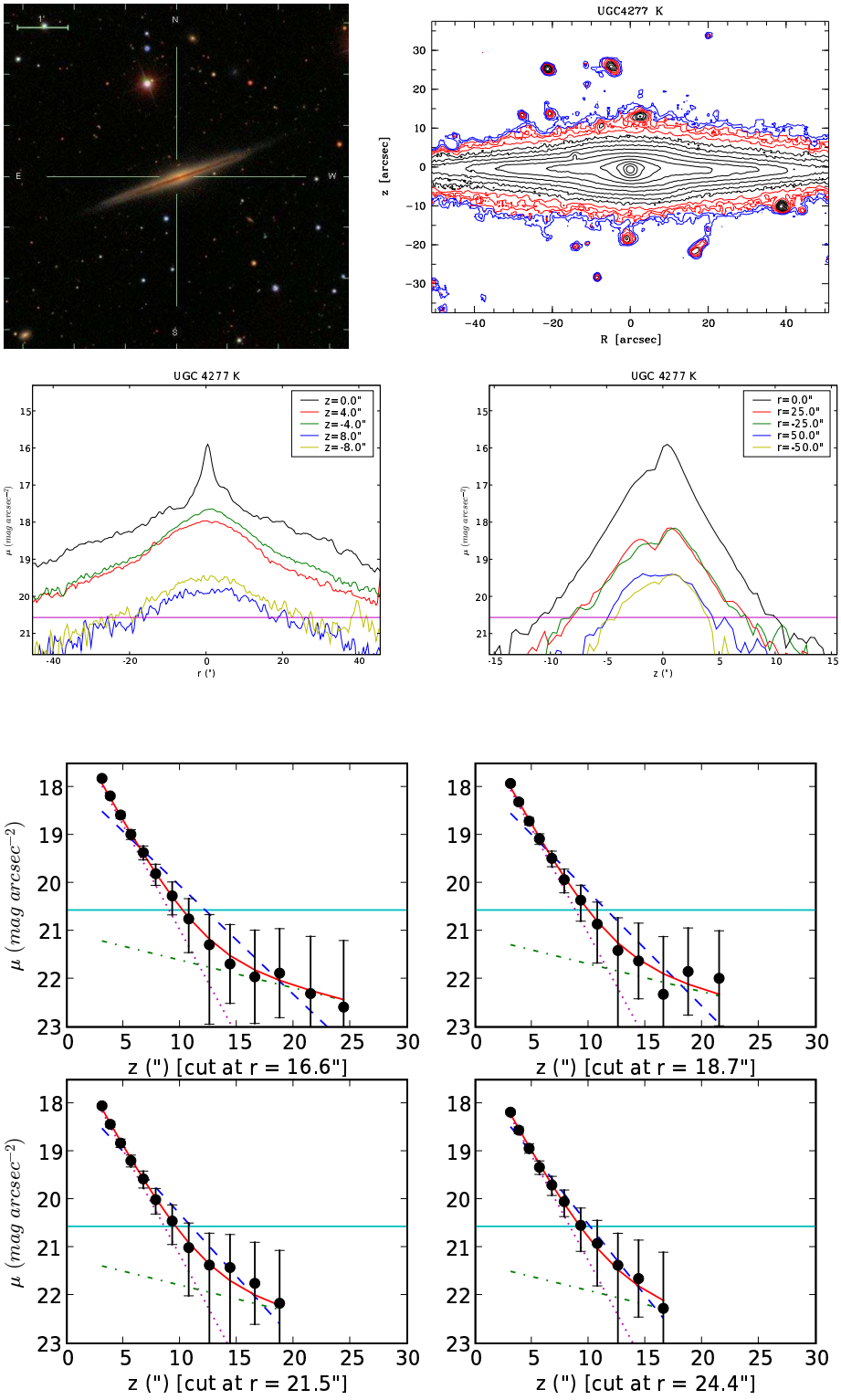

Figure 32: UGC 4277 K

B Single Disk Radial Behaviour of Artificial Galaxies

A one dimensional single disk weighted least-squares fit was done on the complete sample of artifical galaxies that were created, encompassing a μ_{n-k} range of 3–5 (in steps of 1), a f_h range of 0.5–3.0 (in steps of 0.5) and a f_z range of 2-6 (in steps of 2), resulting in 36 artificial galaxies. The overall basic input parameters are $\mu_n = 19.24$ mag arsec^{-2}, $z_n = 10$, $h_n = 50$ with the truncation at $2.5h_n$. Plots were made to show the behaviour of each model of z_0 (fit result) divided by $z_{n,0}$ (input parameter), here expressed at z_n/z_{input}, over the fitted radius range (40–120). $\mu_0 - \mu_{\rm cut}$ was set at 7.4 mag arcsec^{-2}.

The 36 resulting plots are put in three columns. The first column shows the behaviour from small μ_{n-k} to large μ_{n-k} and small f_h to large f_h secondly. The second column shows the behaviour from small f_h to large f_h and from small μ_{n-k} to large μ_{n-k} secondly. The third column shows the behaviour from small f_z to large f_z and from small μ_{n-k} to large μ_{n-k} secondly.

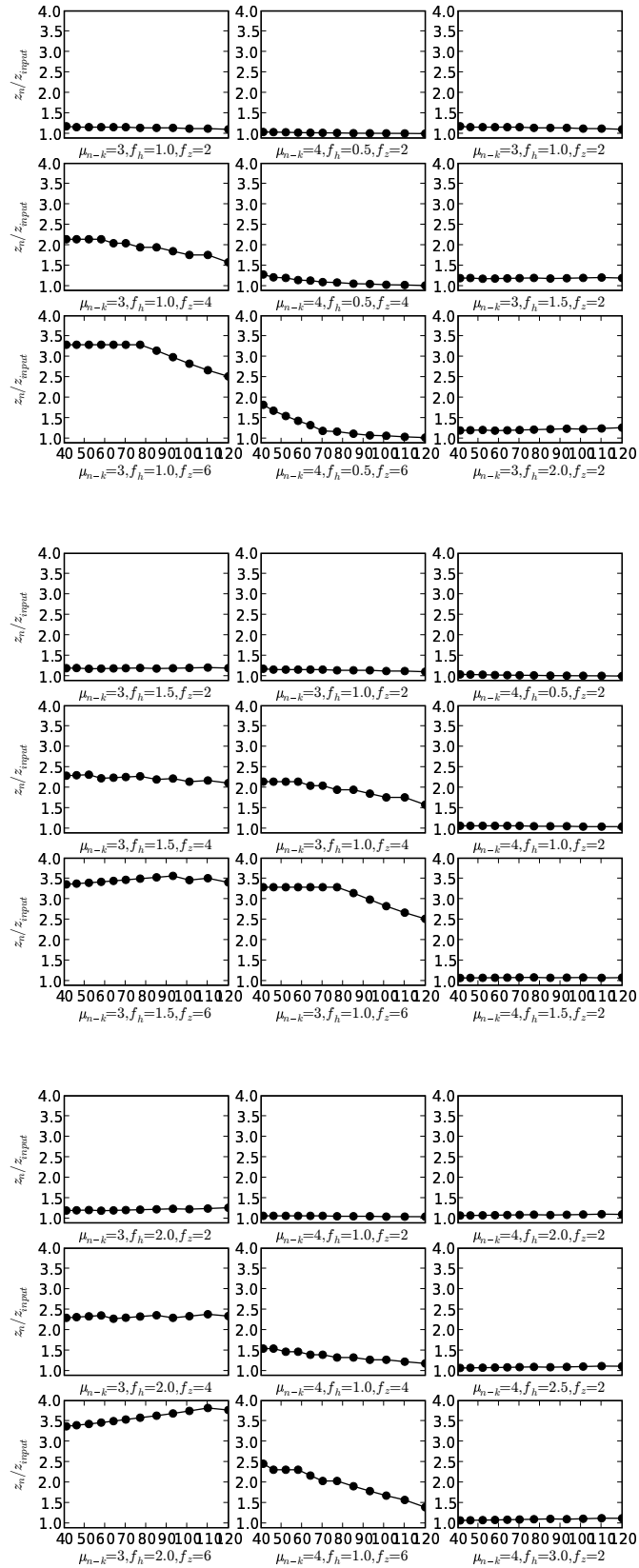

Figure 33: Single Disk Radial Behaviour. Part 1.

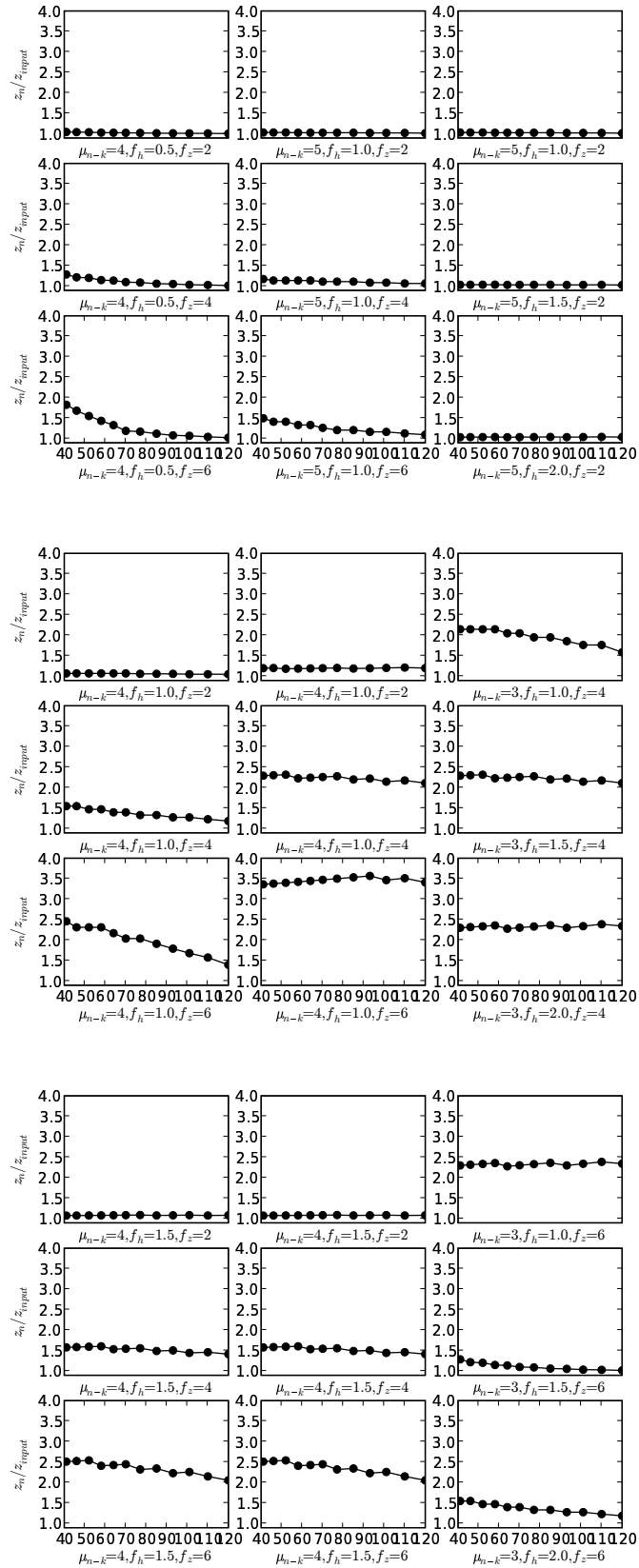

Figure 34: Single Disk Radial Behaviour. Part 2.

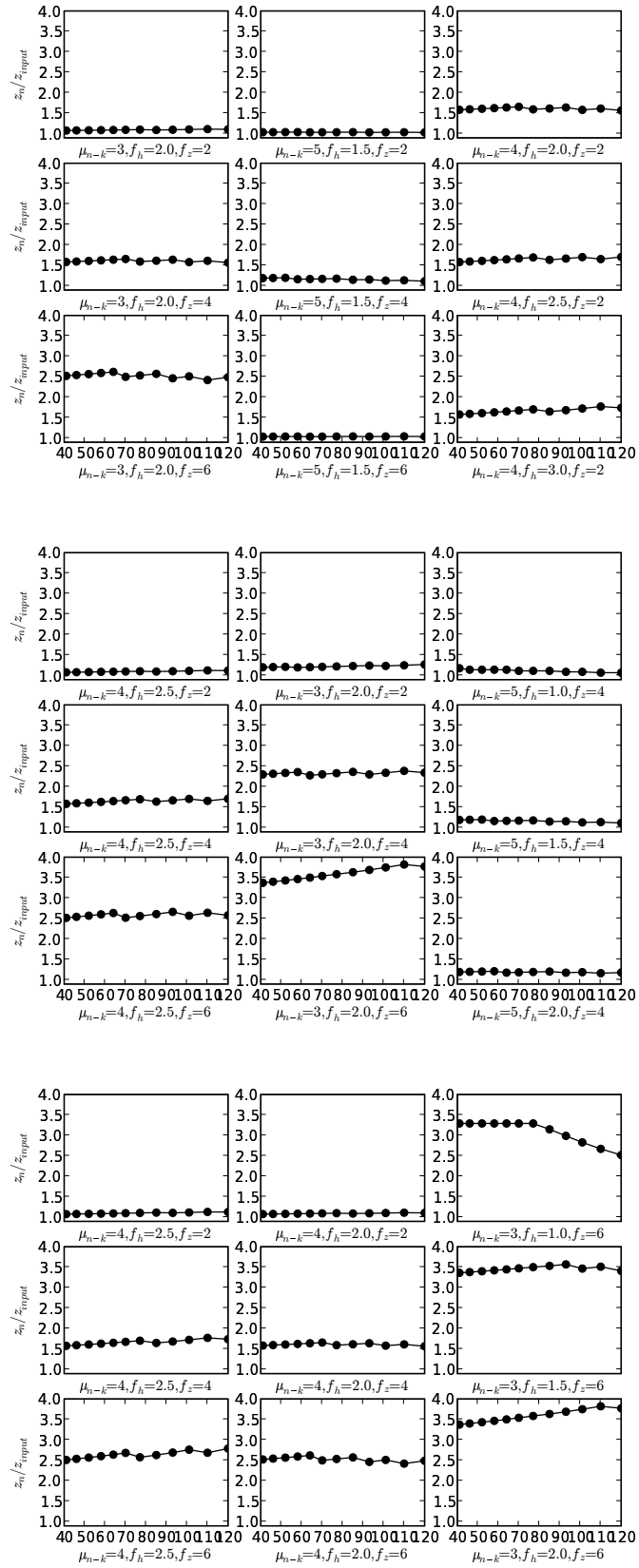

Figure 35: Single Disk Radial Behaviour. Part 3.

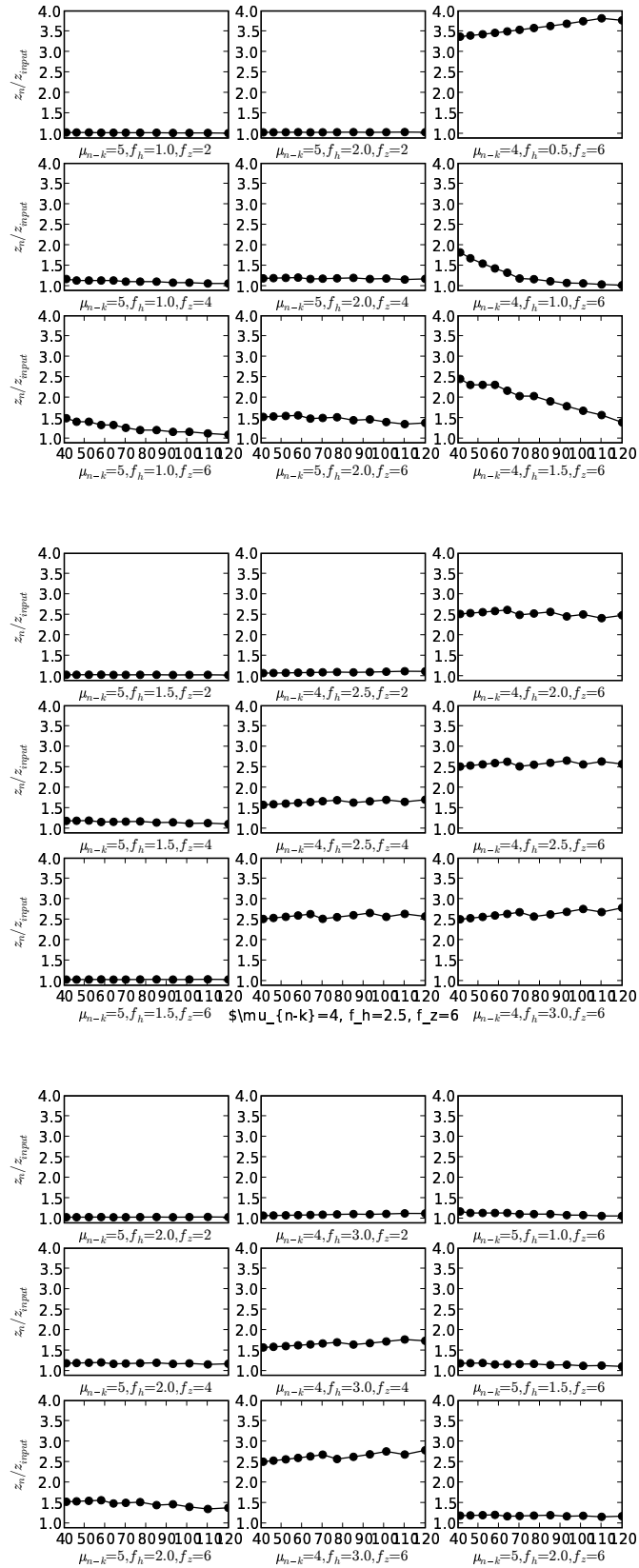

Figure 36: Single Disk Radial Behaviour. Part 4.

C Colour Profiles & Gradients

For each galaxy used to determine the vertical colour gradient a column with four plots is shown. The first plot shows the central vertical colour profile and four equipositioned cuts at the right side of the galaxy. The second plot shows the central vertical colour profile and four equipositioned cuts at the left side of the galaxy, the positions given in negative values. The third plot shows the selected part of the vertical colour profiles used for the fit of the gradient as taken from the first two plots. The fourth plot shows the profile normalized over the scaleheight. The presented profiles are unmatched to the average $z/z_n = 2$ position and uncorrected for the galactic extinction, which will be done while determining the gradient.

In Tables A to F the gradient fit results for each individual cut are shown. The gradient fit results represent the observed values. The central $(J-K)$ values are not matched for their average $2z_n$ $(J-K)$ and are also not corrected for the galactic extinction. These corrections were applied after the determination of all parameter results of the individual cuts.

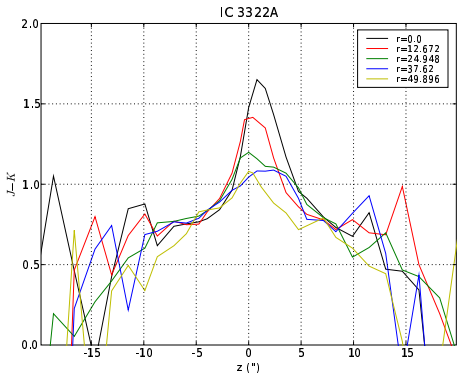

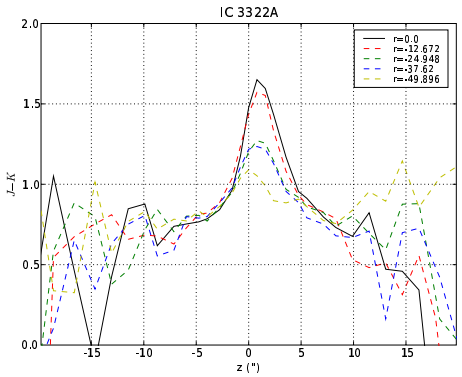

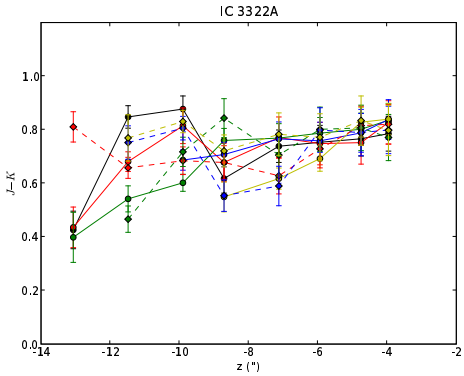

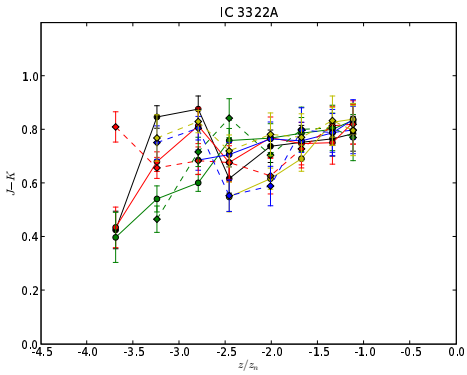

Figure 37: IC 3322A

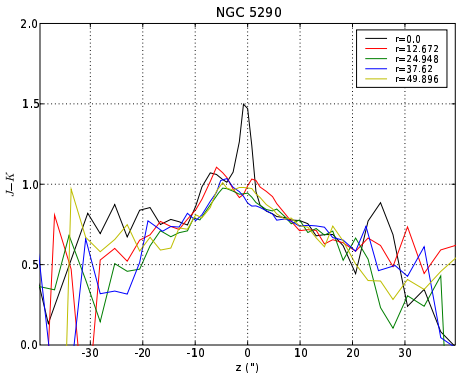

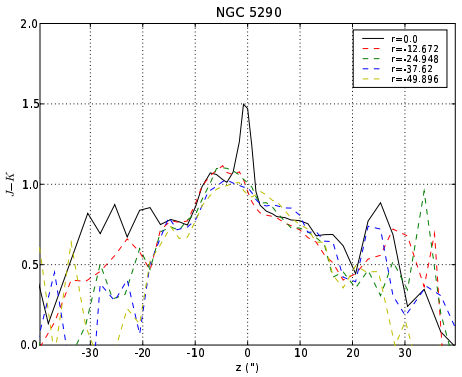

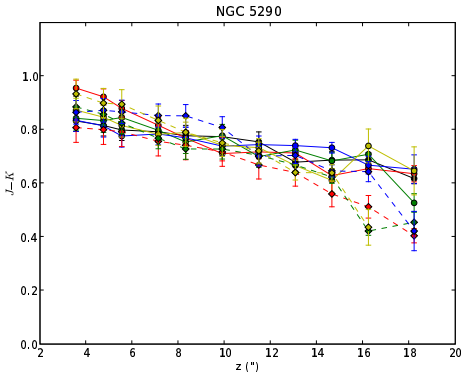

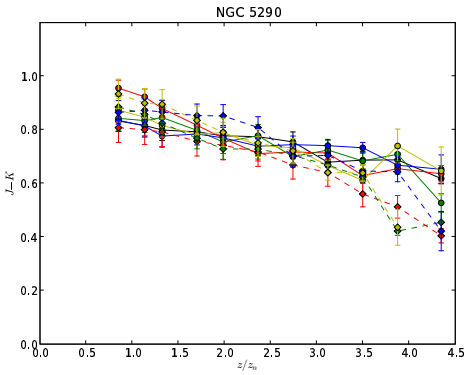

Figure 38: NGC 5290

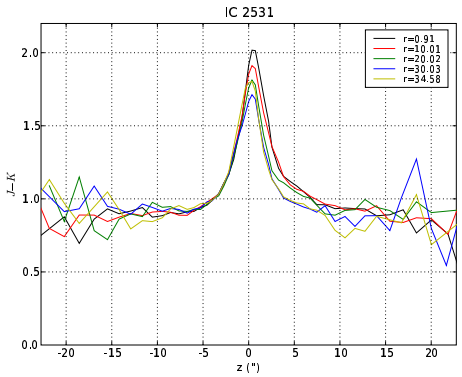

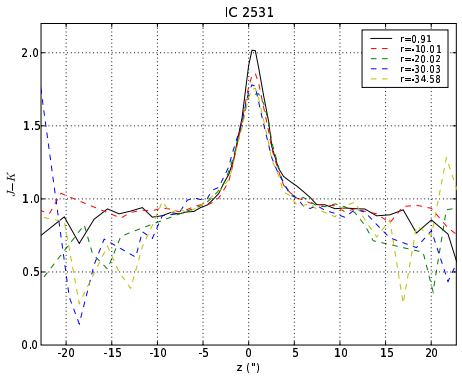

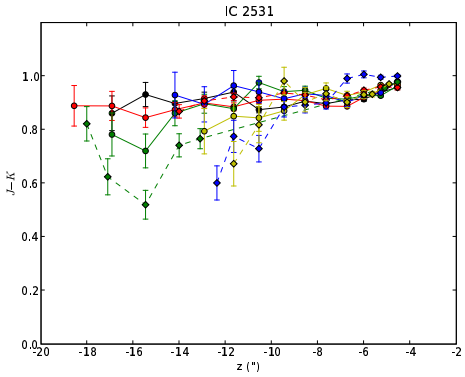

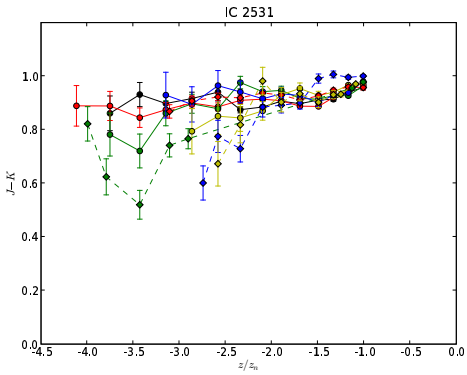

Figure 39: IC 2531

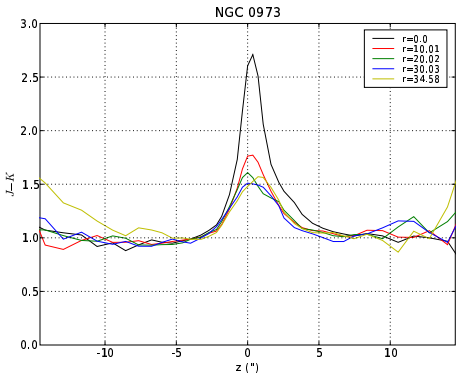

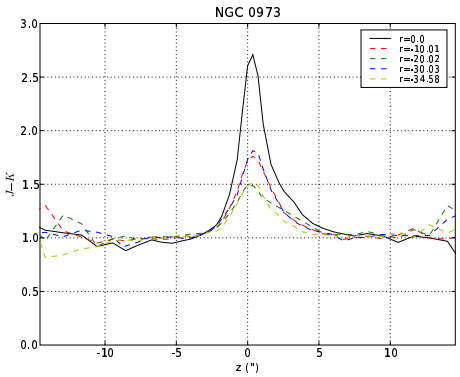

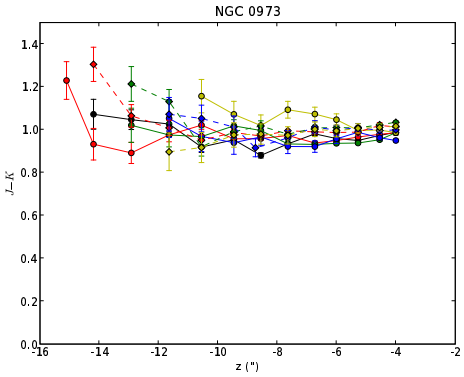

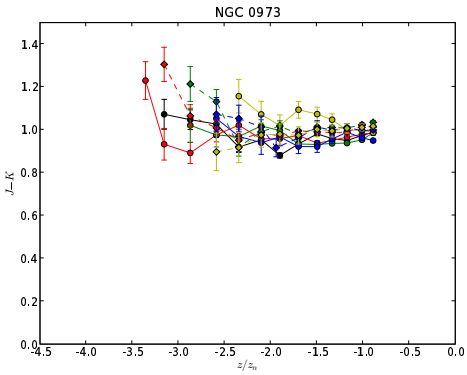

Figure 40: NGC 0973

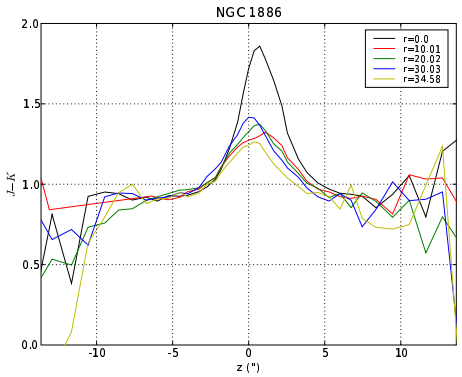

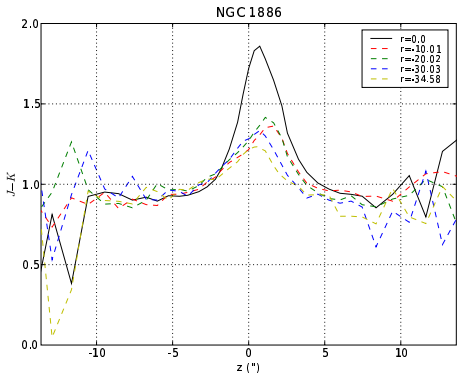

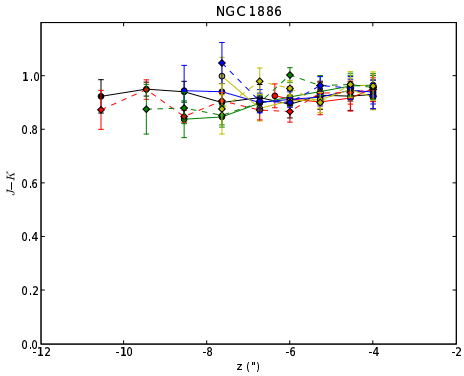

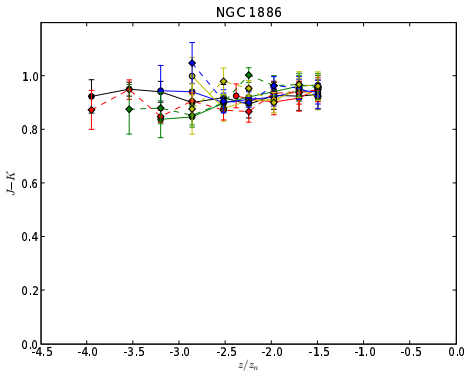

Figure 41: NGC 1886

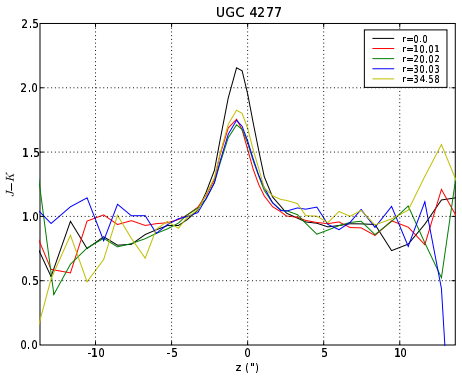

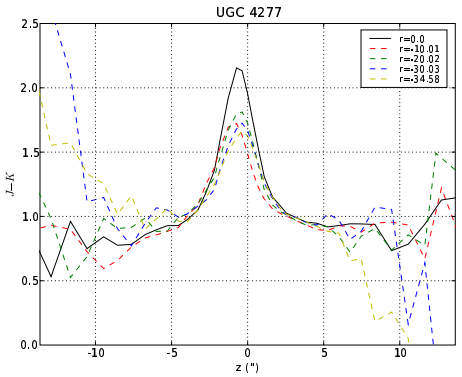

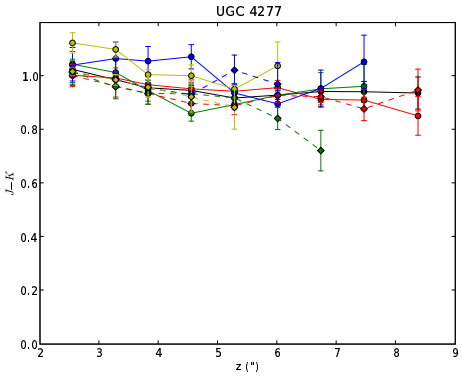

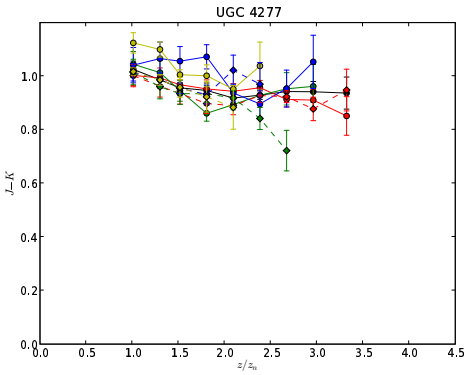

Figure 42: UGC 4277

A: Colour Gradient Fits IC 2531

r [″] (1)	Δ_{J-K} [Mag arcsec^{-1}] (2)	Δ_{J-K} [Mag arcmin^{-1}] (3)	$z_n\Delta_{J-K}$ [Mag] (4)	$J-K$ [Mag] (5)	χ^2 (6)
1.0	-0.007	-0.424	-0.032	0.964	43.9
10.0	-0.010	-0.605	-0.045	0.979	205.3
20.0	-0.009	-0.558	-0.042	0.997	49.6
30.0	-0.014	-0.848	-0.064	1.035	28.8
34.6	-0.016	-0.933	-0.070	1.043	6.7
-10.0	-0.005	-0.300	-0.023	0.971	33.9
-20.0	-0.026	-1.576	-0.118	1.094	22.2
-30.0	-0.030	-1.777	-0.134	1.147	33.4
-34.6	-0.024	-1.412	-0.106	1.082	15.0

B: Colour Gradient Fits IC 3322A

r [″]	Δ_{J-K} [Mag arcsec^{-1}]	Δ_{J-K} [Mag arcmin^{-1}]	$z_n\Delta_{J-K}$ [Mag]	$J-K$ [Mag]	χ^2
0.0	-0.006	-0.357	-0.021	0.804	39.1
12.7	-0.023	-1.389	-0.082	0.918	10.8
24.9	-0.043	-2.569	-0.152	1.044	6.2
37.6	-0.023	-1.368	-0.081	0.911	0.2
49.9	-0.067	-4.043	-0.239	1.112	0.9
-12.7	-0.006	-0.384	-0.023	0.771	10.5
-24.9	-0.040	-2.394	-0.141	1.024	13.6
-37.6	0.000	0.006	0.000	0.726	17.4
-49.9	0.001	0.039	0.002	0.787	2.6

C: Colour Gradient Fits NGC 0973

r [″]	Δ_{J-K} [Mag arcsec^{-1}]	Δ_{J-K} [Mag arcmin^{-1}]	$z_n\Delta_{J-K}$ [Mag]	$J-K$ [Mag]	χ^2
0.0	-0.006	-0.357	-0.027	0.998	89.6
10.0	-0.000	-0.021	-0.002	0.966	46.9
20.0	-0.002	-0.094	-0.007	0.957	37.6
30.0	0.001	0.071	0.005	0.950	9.4
34.6	0.022	1.297	0.097	0.900	4.5
-10.0	-0.004	-0.219	-0.016	1.017	32.3
-20.0	-0.006	-0.335	-0.025	1.046	24.5
-30.0	-0.001	-0.041	-0.003	1.002	7.5
-34.6	-0.011	-0.648	-0.049	1.061	0.7

Notes: (1) Radial position of the profile. (2)(3) $(J-K)$ gradient. (4) $(J-K)$ gradient over units of scaleheight. (5) $(J-K)$ colour. (6) See Section 3.6 for a description.

D: Colour Gradient Fits NGC 1886

r [″]	Δ_{J-K} [Mag arcsec^{-1}]	Δ_{J-K} [Mag arcmin^{-1}]	$z_n\Delta_{J-K}$ [Mag]	$J-K$ [Mag]	χ^2
0.0	0.005	0.287	0.013	0.895	1.3
10.0	-0.009	-0.530	-0.024	0.970	0.5
20.0	-0.032	-1.907	-0.085	1.107	0.4
30.0	-0.007	-0.418	-0.019	0.963	0.9
34.6	-0.003	-0.209	-0.009	0.936	2.8
-10.0	-0.009	-0.548	-0.024	0.962	9.0
-20.0	-0.028	-1.695	-0.075	1.112	8.2
-30.0	-0.007	-0.442	-0.020	0.965	6.3
-34.6	-0.002	-0.124	-0.006	0.958	2.8

E: Colour Gradient Fits NGC 5290

r [″]	Δ_{J-K} [Mag arcsec^{-1}]	Δ_{J-K} [Mag arcmin^{-1}]	$z_n\Delta_{J-K}$ [Mag]	$J-K$ [Mag]	χ^2
0.0	-0.014	-0.859	-0.060	0.893	3.3
12.7	-0.023	-1.368	-0.096	0.993	23.1
24.9	-0.016	-0.974	-0.068	0.918	14.6
37.6	-0.009	-0.567	-0.040	0.854	3.1
49.9	-0.019	-1.114	-0.078	0.929	6.8
-12.7	-0.029	-1.747	-0.122	0.966	5.4
-24.9	-0.034	-2.036	-0.142	1.036	40.5
-37.6	-0.024	-1.429	-0.100	1.002	9.6
-49.9	-0.031	-1.844	-0.129	1.054	5.0

F: Colour Gradient Fits UGC 4277

r [″]	Δ_{J-K} [Mag arcsec^{-1}]	Δ_{J-K} [Mag arcmin^{-1}]	$z_n\Delta_{J-K}$ [Mag]	$J-K$ [Mag]	χ^2
0.0	-0.013	-0.789	-0.033	1.019	5.5
10.0	-0.019	-1.168	-0.049	1.051	1.2
20.0	-0.024	-1.420	-0.060	1.035	13.6
30.0	-0.035	-2.103	-0.088	1.163	8.1
34.6	-0.057	-3.427	-0.144	1.251	6.3
-10.0	-0.012	-0.718	-0.030	0.991	4.8
-20.0	-0.046	-2.763	-0.116	1.132	3.6
-30.0	-0.018	-1.082	-0.045	1.040	3.9
-34.6	-0.047	-2.797	-0.117	1.137	0.02

Notes: See Tables A–C.

List of Tables

1	Observation Sample	9
2	Observation Data	10
3	Mean or Median Counts in Small Boxes	11
4	Photometry Calar Alto Set	13
5	Standard Star Photometry UKIRT Set	14
6	Photometry UKIRT Set	15
7	Residual Background Estimations	16
8	IC 3322A J: 1D Constrained Two Disk Fit Results	29
9	NGC 5981 J: 1D Constrained Two Disk Fit Results	30
10	IC 3322A Alternative Fitting Function Fit Results	31
11	2D Two Disk Fit Results	33
12	2D Two Disk Fit Results in Parsecs	35
13	1D One Disk Fit Results	37
14	1D Weighted Alternative Fitting Function Results	39
15	1D Unweighted Alternative Fitting Function Results	40
16	2D Two Disk Artificial Galaxy Fit Tests Results	41
17	Literature Thick Disk Results	45
18	Metallicities of Bruzual-Charlot SSP Models	49
19	Colour Gradients	50
20	Metallicities for 15 Gyr Stars on $J - K$ Gradients	50

References

Abadi, M. G., F., N. J., Steinmetz, M., and Eke, V. R.: 2003, *ApJ* **591**, 499

Abe, F., Bond, I. A., and Carter, B. e. a.: 1999, *AJ* **118**, 261

Balcells, M., Dominguez-Palmero, L., Graham, A., and Peletier, R. F.: 2001, *ASP Conf. Ser. 249: The Central Kiloparsec of Starbursts and AGN: The La Palma Connection* p. 167

Brook, C. B., Kaiwata, D., Gibson, B. K., and Freeman, K. C.: 2004, *ApJ* **612**, 894

Brook, C. B., Kaiwata, D., Martel, H., Gibson, B. K., and Bailin, J.: 2006, *ApJ* **639**, 126

Bruzual, G. and Charlot, S.: 2003, *MNRAS* **344**, 1000

Burstein, D.: 1979, *ApJ* **234**, 829

Chabrier, G.: 2003, *PASP* **115**, 763

Dalcanton, J. J. and Bernstein, R.: 2002, *AJ* **124**, 1328

De Grijs, R. and Peletier, R. F.: 1997, *A&A* **320**, L21

De Grijs, R. and Peletier, R. F.: 2000, *MNRAS* **313**, 800

De Grijs, R. and Van der Kruit, P. C.: 1996, *A&AS* **117**, 19

De Jong, R. S.: 1996, *A&A* **313**, 337

De Vaucouleurs, G.: 1959, *Handbuch der Physik*, Vol. 53, p. 311

Freeman, K. C.: 1970, *ApJ* **160**, 811

Gilmore, G. and Reid, N.: 1983, *MNRAS* **202**, 1025

Huizinga, J. E.: 1998, *Ph.D. thesis*, Groningen University, Netherlands

James, P. A., Salaris, M., Davies, J. I., and Cassisi, S.: 2006, *MNRAS* **367**, 339

Jensen, E. B. and Thuan, T. X.: 1982, *ApJS* **50**, 421

Knapen, J. H., Beckman, J. E., Shlosman, I., Peletier, R. F., Heller, C. H., and de Jong, R. S.: 1995, *AJ* 443

Kregel, M., Van der Kruit, P. C., and De Grijs, R.: 2002, *MNRAS* **334**, 646

Kuchinski, L. E. and Terndrup, D. M.: 1996, *AJ* **111**, 1073

Larsen, J. A. and Humphreys, R. M.: 2003, *AJ* **125**, 1958

Matthews, L. D.: 2000, *AJ* **120**, 1764

Morrison, H. L., Miller, E. D., Harding, P., Stinebrig, D. R., and Borosan, T. A.: 1997, *AJ* **113**, 2061

Neeser, M. J., Sackett, P. D., De Marchi, G., and Paresce, F.: 2002, *A&A* **383**, 472

Nelder, J. A. and Mead, R.: 1965, *Comp. J* **7**, 308

Ojha, D. K.: 2001, *MNRAS* **322**, 446

Patterson, F. S.: 1940, *Harvard College Observatory Bulletin* **914**, 9

Persson, S. E., Murphy, D. C., Krzeminski, W., Roth, M., and Rieke, M. J.: 1998, *AJ* **116**, 2475

Pohlen, M., Balcells, M., Lütticke, R., and Dettmar, R.-J.: 2004, *A&A* **422**, 465

Pohlen, M., Dettmar, R.-J., Lütticke, R., and Schwarzkopf, U.: 2000, *A&AS* **144**, 405

Pohlen, M. and Trujillo, I.: 2006, *A&A* **454**, 759

Shaw, M. A. and Gilmore, G.: 1989, *MNRAS* **237**, 903

Skrutskie, M. F., Cutri, R. M., Stiening, R., Weinberg, M. D., Schneider, S., and Carpenter, J. M.: 2006, *AJ* **131**, 1163

Tsikoudi, V.: 1979, *ApJ* **234**, 842

Van der Kruit, P. C.: 1979, *A&A Suppl.* **38**, 15

Van der Kruit, P. C.: 1984, *A&A* **140**, 470

Van der Kruit, P. C.: 1988, *A&A* **192**, 117

Van der Kruit, P. C. and Searle, L.: 1981, *A&A* **95**, 105

Van Dokkum, P. G., Peletier, R. F., De Grijs, R., and Balcells, M.: 1994, *A&A* **286**, 415

Vazdekis, A., Casuso, E., Peletier, R. F., and Beckman, J. E.: 1996, *ApJ* **106**, 307

Wadadekar, Y., Robbason, B., and Kembhavi, A.: 1999, *AJ* **177**, 1219

Wu, H., Burstein, D., and Deng, Z.: 2002, *AJ* **123**, 1364

Yoachim, P. and Dalcanton, J. J.: 2006, *AJ* **131**, 226